Carbon Nanotubes: Adsorption, Point Defects and Structural Deformation from Quantum and Classical Simulations

THÈSE N^{O} 6368 (2014)

PRÉSENTÉE LE 19 DÉCEMBRE 2014

À LA FACULTÉ DES SCIENCES DE BASE

CHAIRE DE CHIMIE PHYSIQUE COMPUTATIONNELLE À L'ÉCHELLE NANO

PROGRAMME DOCTORAL EN PHYSIQUE

ÉCOLE POLYTECHNIQUE FÉDÉRALE DE LAUSANNE

POUR L'OBTENTION DU GRADE DE DOCTEUR ÈS SCIENCES

PAR

Jaap KROES

acceptée sur proposition du jury:

Prof. V. Savona, président du jury
Prof. W. Andreoni, directrice de thèse
Dr A. Curioni, rapporteur
Dr O. Gröning, rapporteur
Dr A. V. Krasheninnikov, rapporteur

ÉCOLE POLYTECHNIQUE
FÉDÉRALE DE LAUSANNE

Suisse
2014

Acknowledgements

First of all I thank my supervisor, prof. Wanda Andreoni, for her indefatigable efforts and dedication. Her incisive scientific vision has been of indispensable help to bring this thesis to a successful end. Also, I would thank all other members who are and have been working in our group. Specifically Fabio Pietrucci – who only recently left for a position in Paris – has provided excellent guidance on many different subjects throughout my PhD. Also the many discussions with Gregoire Gallet – with whom I shared an office for several years – has helped to more form my own ideas on both scientific and less scientific problems.
I also sincerely thank my collaborators, at IBM and in the CabTuRes project [1]. The possibility of comparison with experimental results in the CabTuRes project has been extremely motivating. I am especially grateful to Alessandro Curioni for hosting me at IBM Zurich Research Laboratory several times. Moreover his insights to both physics and chemistry, as well as computational expertise, have been very useful.
I also thank my friends, in Switzerland, in the Netherlands and elsewhere. The great times we have had the last four years and for helping me enjoy things outside the thesis work. Specifically I am thankful to Christian, Dafne and Magali, with whom I share a flat in Lausanne since early 2012. Without them I would have not met so many nice and interesting people and my French would have forever remained stuck at the very basics.
Finally I thank my family; my parents and my sister. Without their unconditional support throughout the years, including long before starting the PhD, I would not have arrived at this point.

Lausanne, October 23, 2014 Jaap Kroes

[1] This thesis work was funded by Nano-Tera.ch, a program of the Swiss Confederation, evaluated by the SNSF. Allocations for computer time were provided by the Swiss National Supercomputing Centre (CSCS, projects S245 and S456). Part of the research also benefitted from the allocation in the Blue Gene systems made available by the Center for Advanced Modelling Science (CADMOS). The financial support for CADMOS and for the Blue Gene systems is provided by the Canton of Geneva, the Canton Vaud, the Hans Wilsdorf foundation, the Louis-Jeantet foundation, the University of Geneva, the University of Lausanne, and the Ecole Polytechnique Fédérale de Lausanne.

Abstract

This thesis studies carbon nanotubes using state-of-the-art computational methods. Using large-scale quantum-mechanical calculations, based on density-functional-theory (DFT), we investigate several important aspects of the physics and chemistry of single-walled-nanotubes. The focus is on the effect of defects, namely adparticles and vacancies, on the structural, electronic and dynamical properties of the nanotubes. We also present preliminary results of simulations exploring a possible route for the formation of carbon nanotubes from graphene nanoflakes. Adparticles include atomic hydrogen, oxygen, sulfur at different concentrations as well as nitrogen–oxides. Chemisorption of hydrogen as well as oxygen and isoelectronic species results in the formation of clusters on the sidewall, with characteristic structures corresponding to characteristic signatures in the electronic spectra.

Especially in the case of oxygen, we find that relatively high energy barriers separate different structures: this shows that not only thermodynamically favored configurations are relevant for the understanding of oxygen chemisorption but the presence of traps cannot be neglected. The fingerprint of these traps is confirmed by scanning-tunneling spectroscopy.

Trends with size and chirality of the nanotubes and oxygen coverage are studied in detail and also explained in terms of simple chemical descriptors. The importance of large-scale atomistic models is also emphasized to obtain convergent results and thus reliable predictions, and comparison is made of results we obtain using different gradient-corrected exchange-correlation functionals and in part with hybrid functionals. The study of nitrogen-oxides faces the difficulty to correctly represent physisorption, also with empirically corrected gradient-corrected exchange-correlation and hybrid functionals. Still our calculations of vibrational frequencies of different molecules on the sidewall, once compared with experiment, are able to distinguish the specific species observed in infrared spectra.

Part of our work is centered on the comparison of widely used classical potentials (reactive force fields) with DFT results. Specifically we use them to study hydrogen and oxygen chemisorption, and especially examine the validity of several different force-fields for the description of the structure and energetics of single and double vacancies. In all cases, we find rather limited agreement with DFT results, showing the intrinsic difficulty to represent the subtle and intrinsic quantum effects governing the physico-chemical behavior of carbon nanotubes. Still, the wealth of results we have obtained might be useful for an improvement of these classical schemes for a specific application or other semi-classical models.

Keywords: carbon nanotubes, density functional theory, classical potentials, chemisorption, physisorption, vacancies, nanotube growth

Résumé

Le travail de recherche présenté dans cette thèse porte sur l'étude des nanotubes de carbone à l'aide de méthodes numériques de pointe. Des simulations à grandes échelle basées sur la théorie de la fonctionnelle de la densité (DFT) sont effectuées dans le but d'examiner des aspects importants de la physique et de la chimie des nanotubes. Nous étudions principalement les défauts, tels que les particules adsorbées et les lacunes, ainsi que leurs effets sur la structure géometrique et électronique des nanotubes. Nous présentons également une nouvelle méthode de fabrication des nanotubes à partir de *nanoflakes* de graphène. Les particules adsorbées considérées comprennent les atomes d'hydrogène, d'oxygène et de soufre à diverses concentrations, ainsi que les oxides d'azote. L'hydrogène et l'oxygène s'assemblent sur la surface et forment des structures identifiables dans le spectre électronique.
Dans le cas de l'oxygène, les barrières de diffusion, relativement hautes, piègent les atomes dans leurs positions, montrant ainsi non seulement l'importance des structures thermodynamiquement favorables mais aussi que les "pièges atomiques" ne peuvent être négligés. La signature de ces pièges apparaît en spectroscopie tunnel à balayage.
De plus, les effets de la chiralité du nanotube et de la taille des particules adsorbées sur sa surface sont examinées en détails et expliqués en termes de paramètres géométriques. Les modèles de grandes tailles se révèlent importants pour obtenir des résultats convergés. En outre, une comparaison est effectuée entre des résultats obtenus sous différentes approximations pour la fonctionnelle d'échange et corrélation de la DFT. Les difficultés de la DFT à bien réprésenter la physisorption rendent particulièrement complexes les études des oxides d'azote. Malgré ces complications, nous démontrons qu'il est possible de distinguer les différentes espèces présentes par des calculs de fréquences vibrationnelles moléculaires.
Une partie de ce travail se focalise sur la comparaison entre nos résultats obtenus *ab initio* et les calculs avec des potentiels classiques. En particulier, pour l'hydrogène et l'oxygène et les lacunes atomiques, nous testons différents potentiels classiques disponibles. Dans tous les cas considérés, nous trouvons de forts écarts avec les résultats obtenus en DFT. Ceci montre la difficulté intrinsèque aux nanotubes de carbone où les effets quantiques dominent les intéractions physiques et chimiques. Cependant, la majorité des comparaisons effectuées peuvent servir à de futures améliorations de ces potentiels ou d'autres modèles semi-classiques.

Mots clés : nanotubes de carbone, théorie de la fonctionnelle de la densité, potentiels classiques, chimisorption, physisorption, lacunes, croissance des nanotubes

Contents

List of Figures

List of Tables

1 Motivation

The work presented in this thesis was primarily motivated by the interest in the physico-chemical behavior of single-walled nanotubes (SWNT) as they were explored within the Nanotera project "CabTuRes". More generally, a deep understanding of the fundamental properties of SWNTs is often missing and several issues needed being revisited with accurate *ab initio* simulations and experimental methods. Part of our theoretical work has indeed been in collaboration with experimental groups, the one of Oliver Gröning at EMPA — for the investigation of chemisorption — and with the one directed by Christofer Hierold at ETHZ — for the study of the nitrogen oxides-nanotube interactions. Also, the need for simulations of nanotubes with larger sizes (lengths of the order of the micrometer) was felt allowing for the study of growth and of mechanical properties of realistic systems under different physical conditions. These studies however are not affordable yet with *ab initio* methods and have motivated us to verify whether reliable classical force fields were available through extensive comparison with *ab initio* methods.

2 Introduction to the Physics and Chemistry of Nanotubes

2.1 Description of Carbon Nanotubes

Carbon nanotubes (CNTs) are part of the family of carbon allotropes (see Fig. 2.1). CNTs were discovered by Iijima in 1993 [1] when making detailed tunneling electron microscopy (TEM) micrographs of carbon soot. Since then they have been the topic of both fundamental research as well as provided new opportunities for nanotechnology.

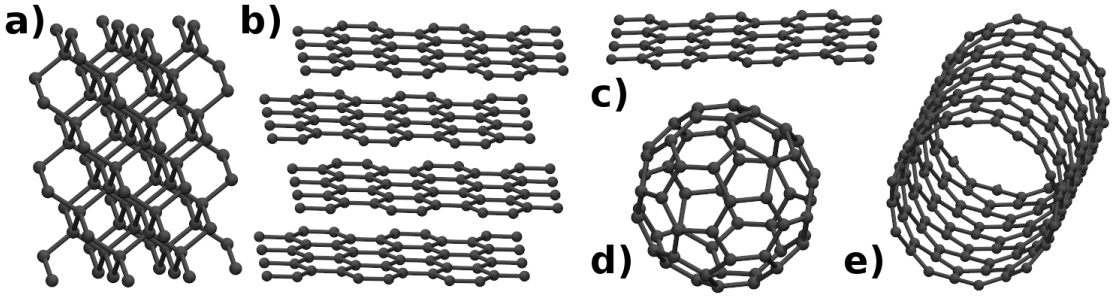

Figure 2.1: Five allotropes of carbon: (a) diamond, (b) graphite, (c) graphene, (d) fullerenes and (e) nanotubes.

The fundamental study of CNTs is primarily complicated because there is not a *unique* CNT structure. CNTs may appear as single-walled CNTs (SWNTs) or multi-walled, they may be isolated or bundled, or may form more complicated structures. Also isolated SWNTs are not unique, but instead represent a family of structures classified according to their chirality $\mathbf{C}_h$. $\mathbf{C}_h$ describes the folding edge to theoretically form a SWNT from a graphene sheet and is defined in terms of the graphene unit vectors as $\mathbf{C}_h = n\mathbf{a}_1 + m\mathbf{a}_2 \equiv (n,m)$ (see Fig. 2.2). The number of atoms in the unit cell (N) of a SWNT is given by [2]

$$N = 4\frac{n^2+m^2+nm}{\mathrm{GCD}(2m+n, m+2n)}.$$

where $\mathrm{GCD}(a,b)$ denotes the greatest common denominator of a and b. The smallest unit cells are those of the *achiral* nanotubes, where $n = m$ (armchair CNTs) or $m = 0$ (zigzag CNTs), containing 2n and 4n atoms respectively. The unit cell of a *chiral* CNT ($n \neq m$ and $n \neq 0$) is

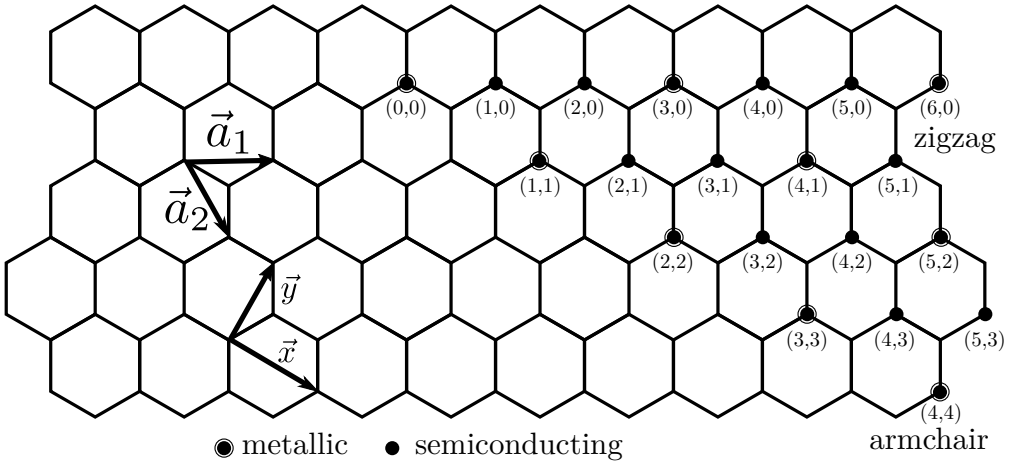

Figure 2.2: Illustration of the chiral indices of a carbon nanotube. The chiral vector $\mathbf{C}_h$ is the folding vector along the tube circumference in terms of the graphene unit vectors $\mathbf{a}_1 = a_{CC}\,(\sqrt{3}/2, 1/2)$ and $\mathbf{a}_2 = a_{CC}\,(\sqrt{3}/2, -1/2)$ with $a_{CC} \approx 1.42$ Å. Encircled dots indicate metallic CNTs where $\mathrm{mod}(n-m,3)=0$. Image based on Fig. 2b in Ref. 3.

easily much larger. For example the unit cell of the (zigzag) (17,0)-CNT contains 68 atoms whereas the chiral (17,1)-CNT contains 1,228 atoms. This complicates the theoretical study of CNTs and forms a simple reason why many studies are based on achiral CNTs.

By applying periodic boundary conditions along $\mathbf{C}_h$ an approximate band structure for CNTs can be constructed from that of graphene, following the *zone-folding* approximation.[2] Discretization of wave vectors along $\mathbf{C}_h$, combined with graphene's zero-gap transition high-symmetry (K) points, then leads to the result that CNTs are metallic if $n-m$ is a multiple of 3 and semiconducting otherwise. Using a tight-binding model Hamiltonian, moreover leads to an exact expression for the band energies from which it can be shown that the bandgap is inversely proportional to the CNT diameter[4–6] ($E_{\mathrm{gap}} = \alpha/D$). The proportionality constant α is experimentally found to be 0.7–0.75 eV·nm.[7,8]

The zone-folding approximation does not account for curvature effects. As such, it breaks down in the case of small diameter CNTs where deviations from ideal sp^2-hybridized C become significant. For example, in the case of the "metallic" (9,0)-CNT a small (0.08 eV) bandgap has been measured[9] using low-temperature atomically resolved scanning tunneling microscopy (STM). Nevertheless, this gap remains significantly smaller than that of typical semiconducting nanotubes,[7,8] which have a gap in the range of 0.5–2 eV. Curvature also breaks the symmetry between the three bonds formed by each C atom, leading to different bond lengths and an increased chemical surface reactivity.[10–13]

Experimentally used CNTs are most commonly grown using chemical vapor deposition (CVD) from hydrocarbon precursor gases on catalytic metal nano-particles (see e.g. Ref. 14). Recent advances in the understanding of CVD growth conditions have enabled selective growth of either semi-conducting or metallic CNTs with a certainty of 99.9%,[15] CNT-lengths of up to half a meter in length,[16] ultra high density (1.6 g cm^{-3}) CNT forest growths,[17] and chirality selective

growth to an accuracy of more than 90%.[18] These advances in controlled and selective growth pave the way for future chirality-specific applications, as well as one-to-one comparison with theoretical predictions.

2.2 Current State of Knowledge

2.2.1 Chemisorption of Hydrogen, Oxygen and Sulfur

Covalent sidewall functionalization[19] is of special relevance for CNTs because of their insolubility in water and most organic solvents. This need for covalent functionalization has driven a widespread effort to understand chemical reactions on the CNT surface. While the bulk of experimental studies have focussed on physisorbed molecular H_2 and O_2, several studies have considered the interactions with atomic hydrogen[20–25] and oxygen[26–29] and the chemisorption that may take place on the nanotube surface.

Thin-film sensor response combined with temperature programmed desorption studies of chemisorbed hydrogen on SWNT thin-films[25] show that hydrogen atoms tend to cluster on the surface and their desorption follows a simple Arrhenius law corresponding to a desorption energy of 1.7 ± 0.04 eV. STM measurements[23] further indicate that chemisorbed hydrogen atoms lead to new states in the electronic bandgap of semiconducting nanotubes. Chemisorbed hydrogen atoms are further identified in infrared spectroscopy by the CH stretching modes which are found[20] at a frequency of 2924 cm^{-1}, or, in the presence of CH_2-groups[22] by two main peaks at 2850 and 2920 cm^{-1}.

For oxygen in particular, the oxygen-based functional groups and the role of oxygen as common attacking agent[30] has driven a number of investigations. Near-edge X-ray adsorption fine-structure (NEXAFS) spectroscopy measurements of oxidized SNWTs[26] show the presence of carbonyl (C=O) and ether (C-O-C) groups, associated with $\pi^\star(CO)$ and $\sigma^\star(CO)$ resonances in the C K-edge spectra respectively. Upon heating to 500–600 K the $\pi^\star(CO)$ spectral features are removed whereas the $\sigma^\star(CO)$ features are found to disappear at an increased temperature (1073 K), suggesting a thermodynamic preference for ethers. This observation is further corroborated by infrared spectroscopy measurements which show the relative intensities of peaks associated with carbonyl groups to disappear first, followed by ether and quinone groups. The tendency for single (ether-like) C-O bonds was further confirmed by XPS experiments,[27] where upon 300 eV O_2^+ irradiation of SWNT bucky paper O(1s)-levels characteristic of a single bond are observed. Also on double-walled nanotubes, XPS measurements[31] show a thermodynamic preference for ether-like configurations.

Thiolation experiments[32] on MWNTs has shown that sulfur chemisorbs on the CNT surface and may be identified through new modes in the Raman spectra near 500 cm^{-1}. Tunneling Electronic Microscopy (TEM) scanning of the resulting CNTs suggests a homogeneous surface coverage of sulfur atoms. Complementary EELS measurements further indicate a sulfur content of $\sim 0.6\%$.

2.2.2 CNT-based Nitrogen-Oxides Sensors

In the seminal paper by Kong et al.[33] strong reversible changes in conductivity were observed as a result of CNT exposure to NO_2 gas. This response was explained by hole doping of the CNT by the adduct. Since then, several experiments have reproduced these results. However, differences in the details of the experimental set-up have lead to large variations in response and recovery timescales and sensitivity. A recent overview of these experimental results can be found in e.g. Ref.34. Two main problems obstruct a clear understanding of the interaction of nitrogen oxides with carbon nanotubes. First, the contribution of the CNT relative to the metal contacts to the device response is unclear. Second, the nature of the chemical generating the response of the device is difficult to ascertain.

The CNTs are coupled to a metal, so that the integrated device is a field-effect transistor where the electronic transport is dominated by the Schottky barrier at the contact.[35] Therefore both the metal and the CNT work functions are relevant as well as the metal-CNT interactions at the interface.[36] The results however appear to depend on the specific experimental setting. For example, it has been shown that replacing Pd or Cr by Al as electrodes in a SWNT-bundle based device, produces a response one order of magnitude faster and qualitatively different.[37] On the other hand, more recent experimental measurements on SWNT based sensors[38] demonstrated that the tubes mainly responsible for the response to NO_2.

X-ray photoemission spectra (XPS)[39] taken on mixed metallic and semiconducting SWNTs exposed to NO_2 in the range of 150–200 K revealed N(1s) core level shifts typical of NO_3. More recently XPS and X-ray Absorption Spectra (XAS) were taken over a range of temperatures, from 100 to 300 K.[40] At 100 K evidence was given for the presence NO_2, N_2O_4 on both metallic and semiconducting nanotubes, whereas data at room temperature were interpreted as due to the presence of defects like metal adparticles. Moreover, NO_2 was found to desorb spontaneously at 140 K. The desorption energy was estimated to be ~ 0.4 eV for metallic SWNTs and 0.2 eV for semiconducting ones,

Infrared spectra measured for a CNT-bundle exposed to NO_2 exhibited an anomalous strong feature that was interpreted as due to NO_2 in interstitial positions within the bundle.[41,42]

2.2.3 Vacancies

Vacancies, interstitials, bond-rotations and non-hexagonal rings are common intrinsic defects of graphitic surfaces in general. Pristine nanotubes are often described as defect-free to a large extent. However, given their reduced dimensionality, a single defect is expected to have stronger effects on their physical and chemical properties than on graphite or also graphene. This explains the great interest in identifying defects on nanotubes also at very low concentration and even in trying to engineering defected SWNTs so as to tailor their electronic properties.[43]

Several techniques are able to detect the presence of defects on the sidewall of nanotubes,[44] but identifying their nature is a more challenging task. For example, Raman spectroscopy is particularly sensitive to structural changes induced by any type of defects through intensity variations of specific phonon bands, shifts and appearance of new features.[45,46] However, also in this case, the source of these "anomalies" is not easy to identify unless combined with calculations (see e.g. Ref. 47). Direct imaging of defects is provided by STM[48] or high-resolution aberration-corrected TEM[49] at atomic resolution. In particular, imaging is combined with high-energy electrons or ions irradiation, which artificially generates different types of defects.[50,51] In particular, artificial generation of vacancies is crucial to allow for systematic studies also for different concentrations. Two main characteristics were identified: the tendency of vacancies to coalesce and a relatively facile of self-healing.[51–53]

2.2.4 Top-down CNT Formation from Graphene Nanoflakes

It is natural to consider graphene as "the basic building block for graphitic materials of all other dimensionalities"[54] and thus to investigate possible routes to fold it into diverse nanostructures. This possibility is of special interest for nanotubes, for which different methods are explored for chirality-selective synthesis. Experimental evidence exists from aberration-corrected HRTEM[55] that graphene nanoribbons (GNR) tend to warp and ripple at the edges. These observations are also supported by a number of simulations .[56–60] Moreover, GNRs were observed to roll up onto nanoscrolls[61] and small flakes to fold into fullerenes .[62] The latter possibility has recently emerged also in *ab initio* dynamical simulations.[63] Suggestions have also come from computations on the formation of GNRs with nanotube-terminated edges.[64,65] More recently, it has been demonstrated[66,67] that seamless wrapping of GNR — in direct analogy with the chiral vector — leads to chirality selective growth of nanotubes. Two different folding approaches have been proposed, of which one based on the twisting of the edges[67] - as suggested by previous simulations[68] - and the other based on graphite ultrasonication in the presence of a templating molecule (ferrocene aldehyde).[66,69] Discussion of related calculations is postponed to Chapter 7. A third method was proposed on the basis from molecular dynamics simulations, based on controlled hydrogenation of the GNR surface to induce curvature.[70,71] However no experimental confirmation has followed.

3 Theoretical & Computational Methods

This chapter provides a brief background to the theoretical and computational methods applied in this thesis. Section 1 recalls the fundamentals of density-functional theory (DFT) and some approximations to the exchange–correlation functional. Section 2 introduces the classical potentials most widely employed to simulate carbon aggregates and that we examine in comparison to DFT-based approaches. Section 3 describes the algorithms we apply to simulate "rare events".

3.1 The Atomistic Model and Basic Equations

We consider a mixed nuclear-electron system in mutual interaction, in which nuclei are treated classically and relativistic effects are not taken into account in the solution of the electronic problem. Moreover, our approach is based on (i) Density-Functional Theory for the description of the electron subsystem; (ii) The Born-Oppenheimer approximation, that allows to separately solve for the electronic and ionic variables; and (iii) The pseudopotential framework in which only valence electrons are explicitly treated and interact with core electrons via an effective potential.

3.1.1 Density Functional Theory and Kohn-Sham formulation

Density Functional Theory (DFT) is a mean-field theory for the ground state of a many-particle system. Let N be the number of particles and define its density as $n(\mathbf{r})$ such that

$$\int d\mathbf{r} n(\mathbf{r}) = N. \tag{3.1}$$

DFT relies on two theorems due to Hohenberg and Kohn,[72] having the density as the key quantity:

1. For any system of interacting electrons in an external potential $v_{\text{ext}}(\mathbf{r})$, this is determined uniquely, except for a constant, by the ground state electron density $n(\mathbf{r})_{GS}$.

2. A *universal functional* for the energy $E[n(\mathbf{r})]$ can be defined for any external potential $v_{\text{ext}}(\mathbf{r})$.

$$E[n(\mathbf{r})] = T[n(\mathbf{r})] + V_{\text{ee}}[n(\mathbf{r})] + \int d\mathbf{r} v_{\text{ext}}(\mathbf{r}) n(\mathbf{r}) \tag{3.2}$$

where $T[n(\mathbf{r})]$ is the kinetic energy of the interacting electrons, $V_{\text{ee}}[n(\mathbf{r})]$ is the electron-electron interaction. For any particular $v_{\text{ext}}(\mathbf{r})$, the exact ground-state energy of the system $E[n(\mathbf{r})]_{GS}$ is the global minimum of this functional and the density that minimizes this functional is the exact ground-state density $n(\mathbf{r})_{GS}$.

By recognizing the unique and key role of the electron density, DFT avoids the determination of the many-electron wavefunction which is also a functional of the density, as any other property of the system. This is a great advantage when trying to solve for the ground-state of a many-body problem but important steps are necessary before a practical application can be realised. The first big step was realised by Kohn and Sham [73] (KS). Kohn-Sham's *ansatz* consists in defining an auxiliary system of non-interacting electrons having the same ground-state density as that of interacting electrons:

$$n(\mathbf{r})_{GS} = n(\mathbf{r})_{GS,KS} = \sum_{i_{occ}} |\phi_i(\mathbf{r})|^2 \tag{3.3}$$

where the ϕ_is are independent one-electron wavefunctions in terms of which the many-electron wavefunctions of the non-interacting system - a Slater determinant - is expressed, and the sum is over the occupied states. In spite of the resemblance with the Hartree-Fock formulation, the ϕ_is have no physical meaning. Kohn–Sham's *ansatz* allows to write the energy functional of the interacting system as

$$E_{\text{KS}}[n(\mathbf{r})] = T_s[n(\mathbf{r})] + E_{\text{ext}}[n(\mathbf{r})] + E_{\text{Hartree}}[n(\mathbf{r})] + E_{\text{xc}}[n(\mathbf{r})] \tag{3.4}$$

$$E_{\text{ext}}[n(\mathbf{r})] = \int d\mathbf{r} v_{\text{ext}}(\mathbf{r}) n(r)(\mathbf{r}) \tag{3.5}$$

$$E_{\text{Hartree}}[n(\mathbf{r})] = \frac{1}{2} \int \frac{n(\mathbf{r}) n(\mathbf{r}')}{|\mathbf{r} - \mathbf{r}'|} d\mathbf{r} d\mathbf{r}' \tag{3.6}$$

where T_s is the kinetic energy of the non-interacting electrons

$$T_s[n(r)] = \sum_{i_{occ}} -\frac{1}{2} \int d\mathbf{r} \phi_i^\star \nabla_i^2 \phi_i(\mathbf{r}) \tag{3.7}$$

and the electron-electron interaction V_{ee} has been partitioned in the Hartree term E_{Hartree}, classical Coulomb e-e repulsion, and the exchange-correlation energy E_{xc} which contains the quantum contribution to the e-e interaction and is only defined by Eq. 3.4 itself. As such, the E_{xc}[n] functional is unknown.

In the KS approach, applying the variational principle to obtain the ground-state density, reduces to minimizing the total energy with respect to the independent one-electron wave-function ϕ_i under the orthonormalization constraints

$$\int d\mathbf{r}\phi_i^\star\phi_i(\mathbf{r}) = \delta_{ij} \tag{3.8}$$

The Kohn–Sham Schrödinger-like equations thus obtained are

$$\mathscr{H}_{\mathrm{KS}}\phi_i \equiv \left(-\frac{1}{2}\nabla^2 + \hat{v}_s\right)\phi_i = \epsilon_i\phi_i \tag{3.9}$$

$$\hat{v}_s = \hat{v}_{ext}(\mathbf{r}) + \hat{v}_H(\mathbf{r}) + \hat{v}_{xc}(\mathbf{r}) \tag{3.10}$$

Both the ϕ_is and the energies ϵ_i have no physical meaning.

The external potential represents in general the interaction of the electron system with the nuclei:

$$\hat{v}_{ext} = \sum_I V_{eI}(\mathbf{r}-\mathbf{R}_I); \qquad \hat{v}_H(\mathbf{r}) = \frac{1}{2}\int d\mathbf{r}'\frac{n(\mathbf{r}')}{|\mathbf{r}-\mathbf{r}'|} \tag{3.11}$$

The total energy of the mixed nuclear-electron system is thus

$$E_{tot} = E_{KS} + E_N \tag{3.12}$$

where

$$E_N = \sum_{I<J} W_{IJ} \tag{3.13}$$

and W_{IJ} represents the Coulomb repulsion of the nuclei.

So far, we have assumed that the many-electrons system has the density of electrons with spin-up $\mathrm{n}_\uparrow$ as with spin-down $\mathrm{n}_\downarrow$. In many cases, however, one needs to account for spin-polarization, and thus a spin-dependent functional $E[\mathrm{n}_\uparrow,\mathrm{n}_\downarrow]$.

3.1.2 Approximations to the Exchange-Correlation Functional

A major theoretical effort has been directed towards finding reliable approximations to the functional $E_{\mathrm{xc}}[n(\mathbf{r})]$. Only the most common approximations are discussed here, that are used in this thesis.

Local Density Approximation In the local density approximation (LDA), the xc-energy is a local functional of the density, namely

$$E_{\rm xc}^{\rm LDA}[n(\mathbf{r})] = \int \left(\epsilon_{\rm x}^{h}(n(\mathbf{r})) + \epsilon_{\rm c}^{h}(n(\mathbf{r})\right) n(\mathbf{r}) d\,\mathbf{r}, \tag{3.14}$$

where at any **r** the energy density is expressed as that of the homogeneous electron gas (HEG). In particular, for the density n_0, the HEG exchange energy density has a simple analytic expression [74]:

$$\epsilon_{\rm x}^{\rm h} = -\frac{3}{4\pi}\left(\frac{9\pi}{4}\right)^{1/3}\frac{1}{r_s}$$

where r_s is the Wigner–Seitz radius

$$r_s = \left(\frac{3}{4\pi n_0}\right)^{1/3}$$

and the correlation energy density has analytical expressions only in limit of high [75] and low densities. [76]

$$\epsilon_{\rm c} = \begin{cases} A\log r_s + B + r_s(C\log r_s + D) & \text{for high densities,} \\ \frac{1}{2}\left(\frac{g_0}{r_s} + \frac{g_1}{r_s^{3/2}} + \frac{g_2}{r_s^2} + \ldots\right) & \text{for low densities,} \end{cases}$$

For intermediate values of the density, $\epsilon_{\rm c}$ is known in numerical form from the results of quantum Monte Carlo calculations . [77] In practice, several parametrizations are used (e.g., Ref.s 78,79).

The spin-density-dependent version of the LDA — called local spin-density approximation (LSDA) — is constructed in a similar way. [80]

The L(S)DA is known to give good results especially for structural properties of metals and semiconductors but also significantly underestimate bond lengths (both is solids and molecules) and strongly overestimate atomization energies. However its success is not limited to systems with slowly varying densities. This has been mainly attributed to the fact that the exchange-correlation hole satisfies the correct sum rule which excludes one electron from the vicinity of of another. [81]

3.1.2.1 Gradient Corrected Exchange-Correlation Functionals

The first natural extension of $E_{\rm xc}$[n(r)] beyond the LDA is a semi-local approximation including the local gradient of the density. Initial attempts known under the Gradient Expansion Approximation (GEA) to 2nd order (GE2) led to worsening of the LDA results and especially to spurious divergences, which forced the introduction of a real-space cutoff to correct the long-range behavior. This was achieved in the scheme referred to as the generalized gradient

approximation (GGA).[82–84] The GGA formulation of the xc-functional also satisfies a number of fundamental constraints of the HEG, including the xc-hole sum rule. In this way, just as the LDA, it does not contain any empirical parameter.

In GGA the exchange functional is written as

$$E_x^{GGA}[n] = \int d\mathbf{r} n(\mathbf{r}) \epsilon_x^{\mathrm{h}}(n(\mathbf{r})) F_x(s)$$

where

$$s = |\nabla n|/2k_F n; \qquad k_F = (3\pi n)^{1/3}$$

and the correlation functional is written as

$$E_c^{GGA}[n] = E_c(LDA) + F_c(r_s, \zeta, t)$$

where

$$\zeta = n_\uparrow - n_\downarrow; \qquad t = \frac{\nabla n(\mathbf{r})}{2k_s \phi n(\mathbf{r})}; \qquad k_s = 2\sqrt{k_F/\pi}; \qquad \phi = \frac{(1+\zeta)^{2/3} + (1-\zeta)^{2/3}}{2}$$

where $n_{\uparrow(\downarrow)}$ is the density of the electrons with spin $\uparrow$ ($\downarrow$).

The simplest and most widely used form of a GGA functional is the so-called Perdew-Bruke-Erzenhof (PBE) approximation,[85] in which

$$F_x(s) = 1 + k - \frac{k}{1 + \mu s^2/k},$$

where k and μ are constants, and

$$F_c(r_s, \zeta, t) = \gamma \phi^3 \log\left\{1 + \frac{\beta}{\gamma} t^2 \frac{1 + At^2}{1 + At^2 + A^2 t^4}\right\}$$

where

$$A = \frac{\beta}{\gamma}\left[\exp\left(\frac{-\epsilon_c^{\mathrm{h}}}{\gamma\phi^3}\right) - 1\right]^{-1},$$

k_s is the inverse Thomas-Fermi screening wavelength and β and γ are constants.

The expression of Becke's gradient-corrected exchange energy functional is

$$E_x(\text{Becke}) = E_x(\text{LSDA}) - \beta \sum_\sigma \int d\mathbf{r} n_\sigma^{4/3} B(n_\sigma)$$

where

$$B(n_\sigma) = x_\sigma^2/(1+6\beta x_\sigma \sinh^{-1} x_\sigma)$$

and

$$x_\sigma = |\nabla n_\sigma|/n_\sigma^{4/3}$$

The so-called BLYP gradient-corrected functional combines Becke's formulation for the exchange functional,[86] that corresponds to a GGA, with the Lee-Yang-Parr (LYP) approximation to the correlation functional.[87] The expression of Becke's gradient-corrected exchange energy functional is

$$E_x(\text{Becke}) = E_x(\text{LSDA}) - \beta \sum_\sigma \int d\mathbf{r} n_\sigma^{4/3} B(n_\sigma)$$

where

$$B(n_\sigma) = x_\sigma^2/(1+6\beta x_\sigma \sinh^{-1} x_\sigma)$$

and

$$x_\sigma = |\nabla n_\sigma|/n_\sigma^{4/3}.$$

Here one parameter β is present, which is fitted to the exact HF exchange energies of selected rare gases. The LYP functional was derived as a simplification and fitting of a more complicated (and rigorous) functional.[88]

Grimme's corrections One of the major failures of LSDA and gradient-corrected functionals is that they are unable to represent dispersion forces, due to the short-ranged character of the approximated correlation energy functional. Therefore systems where the long-range part of the van-der-Waals (vdW) interactions are relevant cannot be treated correctly. In order to overcome this problem, a variety of corrections have been proposed. One simple method to achieve this aim is by adding a long-range interaction tail of the form r^{-6}. A few models have been introduced by Grimme.[89,90] In particular the so-called Grimme-D2 correction is expressed as

$$E_{\text{Grimme}}^{D2} = -s_6 \sum_{I>J} \frac{C_6^{IJ}}{R_{IJ}^6} f_{\text{damp}}(R_{IJ}), \tag{3.15}$$

with C_6^{IJ} a constant and the function f_{damp} damps the interactions at short distances so that the description of chemical bonds remains unchanged. The parameter s_6 is a scaling factor depending on the xc-functional to which the correction is applied.

3.1.2.2 Hybrid Functionals

The common idea of this class of functionals is adding a fraction of the exact Hartree-Fock exchange to the GGA expressions, with

$$E_{\mathrm{x}}^{\mathrm{HF}} = \sum_{ij} \int \int \frac{\phi_i(\mathbf{r})\phi_j(\mathbf{r})\phi_i^{\star}(\mathbf{r}')\phi_j^{\star}(\mathbf{r}')}{|\mathbf{r}-\mathbf{r}'|} d\mathbf{r} d\mathbf{r}'. \tag{3.16}$$

This explicitly includes a dependence of the functional on the KS one-electron wavefunctions.

The hybrid functionals used in this thesis are PBE0[91] and B3LYP[92] functionals. In PBE0 the xc–energy is given by[91]

$$E_{\mathrm{xc}}^{\mathrm{PBE0}} = (1-a_0)E_{\mathrm{xc}}^{\mathrm{PBE}} + a_0 E_{\mathrm{x}}^{\mathrm{HF}}, \tag{3.17}$$

with the coefficient $a_0 = 0.25$. In analogy with PBE, also PBE0 does not contain any empirical parameter. PBE0 is known to lead to remarkable improvement e.g. in the values molecular dissociation energies and the description of charged defects in solids.

The B3LYP functional[92] is defined as

$$E_{\mathrm{xc}}^{\mathrm{B3LYP}} = E^{\mathrm{LDA}} + a_1(E_{\mathrm{x}}^{\mathrm{HF}} - E_{\mathrm{x}}^{\mathrm{LDA}}) + a_2(E_{\mathrm{x}}^{B} - E_{\mathrm{x}}^{LDA}) + a_3(E_{\mathrm{c}}^{\mathrm{LYP}} - E_{\mathrm{c}}^{\mathrm{LDA}}). \tag{3.18}$$

The three coefficients (a_i) depend on the choice of the particular parametrization used for LDA and on the fitting data set. In the original formulation, these were sets of thermochemical data. In general, this is the preferred functional used to study molecular systems and complex bonding situations.

Adding the non-local exchange term makes calculations with hybrid functional computationally much more demanding than LDA or GGA. In many cases, the gain in accuracy is significant. For example, the partial inclusion of exact exchange cancels in part the self-interaction of the Hartree term, thus improving e.g. the calculation of the electron affinity. Also, a byproduct is the opening of the HOMO-LUMO gap or the valence-conduction bandgap in the KS spectrum.

3.1.3 The Pseudopotential Approach

In the pseudopotential scheme one reduces the electronic problem to that of the valence electrons, which interact with the core-electrons via an effective potential. The inherent approximation is the so-called "frozen-core approximation" that ignores any variation of the core-electron distribution under the effect of any physical or chemical stimulus. The effect of core electrons on the valence electrons is a fixed potential that includes the screening of the nuclear charge and mimics the repulsion due to orthogonality constraints. There are numerous techniques for the construction of atomic pseudopotentials. The most commonly procedure is the one leading to "norm-conserving" pseudopotentials,[93] namely such as to ensure that the pseudo-wavefunction very closely corresponds to the all-electron wavefunc-

tion beyond a certain "core" radius (r_c), fixed a priori, within which the norm (integral of the probability density) of the pseudo- and all-electron wavefunctions are the same. Clearly, this choice is crucial in determining the accuracy of the pseudopotential. The general criterion for a "good" atomic pseudopotential is its *transferability*, namely its ability to describe the core effects in different states of the valence electrons. In practice, this can be verified e.g. at different ionized or excited states in the atom, and globally when passing to molecules and condensed matter systems. Adding to accuracy is also the "non-local" representation of pseudopotential, namely the inclusion of an explicit dependence on the angular momentum of the valence electron state in the atom.

In the following pseudopotentials constructed with the algorithms by Martins-Troullier[94] (MT) and Goedecker-Tetter-Hutter (GTH) pseudopotentials[95] will be used. The former have a numerical form; the latter have an analytical form - separable in real- and reciprocal-space - which is particularly convenient for our computations.

3.1.4 Basis Sets

The solution to the KS equations is generally obtained after expanding the wavefunctions is a given basis set. Depending on the atomistic model either localized basis functions (Gaussians, Slater orbitals or numerical) or plane waves are selected.

Apart from some tests we have made to validate or compare our results for simple molecules with all-electron calculations, we have used plane waves as basis functions. A number of requirements make this basis set convenient in general: they constitute an orthonormal and complete basis set. In particular, completeness allows to control the convergence of the results via simple tests by increasing the expansion cutoff. Plane waves are especially suited for our calculations which are performed in the pseudopotential scheme and use periodic boundary conditions. Several matrix elements can also be expressed analytically. Moreover, *ab initio* molecular dynamics benefits from the use of plane waves[96] because they are independent from the atomic coordinates and also the calculation of the forces acting on the atoms can be done on the same footing as the energies. We use the well-established schemes implemented in the CPMD code.[97]

3.1.5 *Ab initio* Molecular Dynamics

With *ab initio* MD, one generally refers to molecular dynamics (MD) in which the forces acting on the nuclear coordinates are explicitly calculated within DFT. The direct procedure obviously consists of a dynamics, in which at each step of the nuclei Kohn-Sham equations are solved and forces are calculated that drive the next step. This is the so-called Born-Oppenheimer MD. It guarantees decoupling of electronic and nuclear variables and high accuracy in the forces. However it is not computationally efficient and for this reason it is only rarely used. An elegant and efficient algorithm unifying DFT and MD was first proposed by Car and Parrinello in their seminal paper.[98] There they introduced a new type of MD (Car-Parrinello MD) based

on the following (CP) Lagrangian

$$\mathscr{L}^{\mathrm{CP}} = \sum_i \mu \langle \dot{\psi}_i | \dot{\psi}_i \rangle + \sum_I \frac{1}{2} M_I \dot{\mathbf{R}}_I - E_{\mathrm{KS}}[n(\mathbf{r})] + \sum_{ij} \Lambda_{ij} \left(\langle \psi_i | \psi_j \rangle - \delta_{ij} \right).$$

The electronic variables are one-electron wavefunctions (ψ_i) and are treated on the same footing as the nuclear variables (R_I): this is accomplished by associating a fictitious mass μ to the ψ_is and thus a kinetic energy term. The functional E^{DFT} plays the role of the potential energy and is expressed as in the Kohn-Sham formulation. Given the orthonormality propriety of the electronic wavefunctions, this has to be explicitly imposed as a constraint, using Lagrange multipliers Λ_{ij}. The equations of motion are derived from the Euler-Lagrange equations

$$\frac{d}{dt} \frac{\partial \mathscr{L}^{\mathrm{CP}}}{\partial p} - \frac{\partial \mathscr{L}^{\mathrm{CP}}}{\partial q} = 0,$$

where q and p represent the nuclear and electronic coordinates ($\mathbf{r}_i$ and $\mathbf{R}_I$) and conjugate momenta. We thus get

$$M_I \ddot{\mathbf{R}}_I = -\nabla_I E_{\mathrm{KS}}, \qquad \mu \ddot{\psi}_i = -\frac{\delta E_{\mathrm{KS}}}{\delta \psi_i^\star} + \sum_j \Lambda_{ij} \psi_j. \tag{3.19}$$

By applying a unitary transformation, so that Λ becomes diagonal, the latter is equivalent to a KS equation, with Λ_{ii} the one-electron energies.

Note that the fictitious mass μ is a "free" parameter and is chosen so as to ensure that the coupling between electronic and nuclear degrees of freedom remains weak during the simulation (see e.g., Ref.99). To integrate the equations of motion, the Verlet algorithm [100] is commonly used with a time step that depends on the specific system. Given the different time scales of the motion of electronic and nuclear variables, time step to be used in Car-Parrinello MD is significantly smaller than for classical and also Born-Oppenheimer MD. A combination of the Car-Parrinello and Born-Oppenheimer MD has also been proposed [101] that enables significant acceleration of the former.

Several extensions of the original CP Lagrangian have been made and successfully applied: for example, the formulation in terms of Mermin finite-temperature functional [102] to treat non-zero gap systems, the addition of Nose'-Hoover constraints [103,104] to allow for simulations at constant temperature (canonical ensemble) or also Parrinello-Rahman constraints [105] to allow for simulations at constant pressure. [106]

In this thesis, Car-Parrinello MD is applied only in Chapter 7 to simulate the folding of a GNR-model to a nanotube at 1000 K. However, we have also made use of it to verify the stability of various structures at low temperatures.

3.2 Classical Potentials

Real nanoscale systems have often a size that cannot allow for an accurate modeling with *ab initio* calculations. In these case, simulations are made using classical potentials which generally have also simple and physically appealing analytical expressions. The force-fields we consider here are called "reactive" because they aim at representing situations with difference bonding pattern and also chemical processes. This requirement is particularly intriguing for carbon, given its high chemical versatility.

3.2.1 The "Reactive Bond-Order" family

The potential called Reactive Bond Order (REBO [107]) is the "parent" of a class of potentials whose key ingredient is indeed the bond-order, which was originally introduced in the context of classical potentials by Tersoff. [108] The value of the bond-order changes with varying environment in the attempt to simulate the change in the electronic structure of the quantum system.

The REBO bond order is defined as

$$b_{ij}^{\mathrm{REBO}} = \frac{1}{2}\left[b_{ij}^{\sigma-\pi} + b_{ji}^{\sigma-\pi}\right] + b_{ij}^{\pi,RC} + b_{ij}^{\pi,DH}.$$

where the separate terms represent different aspects of the chemical environment which may reduce the attraction between the atom pair: $b_{ij}^{\sigma-\pi}$ and $b_{ji}^{\sigma-\pi}$ account for the angular dependence and the coordination numbers; $b_{ij}^{\pi,RC}$ accounts for radical character and bond conjugation; $b_{ij}^{\pi,DH}$ is responsible for the energy change associated with dihedral rotations.

The expression of the REBO potential energy reads

$$E^{\mathrm{REBO}} = \frac{1}{2}\sum_{i\neq j}[V_R(r_{ij}) - b_{ij}\,V_A(r_{ij})], \tag{3.20}$$

where r_{ij} is the distance between atom i and j and V_R and V_A are repulsive and attractive pair potentials respectively:

$$V_R(r) = f^c(r)\sum_{n=1,3} B_n \exp(-\beta_n r), \qquad V_A(r) = f^c(r)(1+Q/r)A\exp(-\alpha r),$$

where $f^c(r)$ is a switching function varying smoothly from one to zero in the cutoff region (between 1.7 and 2.0 Å for carbon). The constants A, Q, α, B_n and β_n are fitted to a database of mixed empirical and computed physical properties like relevant energies (e.g., atomization

energies, heat of formation), bond-lengths and force constants. In the case of carbon,[107] these refer to crystal structures (diamond, graphite, simple-cubic and face-centered-cubic) and hydrocarbons (ethyne, ethene, ethane, cyclohexane, benzene).

The Adaptive Intermolecular Reactive Bond Order (AIREBO[109]) potential adds the Lennard-Jones(LJ) interaction term as well as a torsional contribution to the REBO expression:

$$E^{\text{AIREBO}} = E^{\text{REBO}} + E^{\text{LJ}} + E^{\text{torsion}}.$$

In order to preserve the reactive nature of the REBO potential, the LJ-interaction between two atoms i and j is only added in specific situations, defined on the basis of their distance (r_{ij}), the bond strength (through a modified b_{ij}) and the bond network between them. In the case of carbon and hydrogen only empirical data were used for the fitting of the LJ parameters: the interlayer spacing and the c_{33} elastic constant of graphite for the C-C potential; the structure and vaporization energy of liquid methane and ethane for the H-H potential, and simple combination rules for the C-H interaction.

The torsional energy is given by

$$E^{\text{torsion}} = \frac{1}{2} \sum_{l \neq k \neq j \neq i} f^c(r_{ij}) f^c(r_{jk}) f^c(r_{kl}) V^{\text{torsion}}(\omega_{ijkl}),$$

with

$$V^{\text{torsion}}(\omega_{ijkl}) = \epsilon_{ijkl} \left[\frac{256}{405} \cos^{10}\left(\frac{\omega_{ijkl}}{2} \right) - \frac{1}{10} \right],$$

where ω_{ijkl} is the torsional angle and ϵ is a constant related to the energy barriers for dihedral rotations. For carbon-hydrogen systems, ϵ_{ijkl} is fitted so as to reproduce experimental bond rotation barriers for ethane and propane as well as different conformers identified in liquid butane.

Another potential of the REBO family, especially targeted to carbon aggregates in condensed phases, is the so-called Long-Range Carbon Bond Order Potential of which two versions have been applied over the years: LCBOPI[110] and LCBOPII.[111]

The LCBOPI energy is written as

$$E^{\text{LCBOPI}} = \frac{1}{2} \sum_{i \neq j} [S^{\text{down}}(r_{ij}) V_{ij}^{SR}(r_{ij}) + S_{ij}^{\text{up}}(r_{ij}) V^{LR}(r_{ij})],$$

where S are switching functions (with $S^{\text{up}}(r) = 1 - S^{\text{down}}(r)$) designed to smoothly switch between short- and long-ranged interaction terms V^{SR} and V^{LR}. The contribution from the short-range interaction is similar to the REBO expression for the total energy (Eq. 3.20), namely

for each pair

$$V^{SR}(r_{ij}) = V_R(r_{ij}) - b_{ij}\, V_A(r_{ij}),$$

with

$$V_A(r) = A\exp(-\alpha r), \qquad V_R(r) = \sum_{n=1,2} B_n \exp(-\beta_n r).$$

The bond order in LCBOPI is defined as

$$b_{ij}^{\mathrm{LCBOPI}} = \frac{1}{2}\left[\tilde{b}_{ij} + \tilde{b}_{ji}\right] + F^{\mathrm{conj}},$$

where $\tilde{b}_{ij}$ contains the angular dependence and F^{conj} is a complicated function aimed at describing conjugation effects.

The long-range term $V^{LR}(r)$ is written as

$$V^{LR}(r) = \theta(r_0 - r)V_1^M(r) + \theta(r - r_0)V_2^M(r),$$

where θ is the step function and $V_k^M(r)$ (k=1,2) are Morse potentials.

The parameters entering both short- and long-range potentials were fitted to reproduce the values of several bulk and surface properties of graphite and diamond obtained with DFT-LDA calculations.

The energy expression of the LCBOPII scheme is

$$E^{\mathrm{LCBOPII}} = E^{\mathrm{LCBOPI}} + \frac{1}{2}\sum_{i\neq j} S_{mr,ij}^{\mathrm{up}}\, V_{ij}^{mr}.$$

where the short-range potential of LCBOPI is modified and new medium-ranged interactions are added (covering the range from 1.7 to 4 Å).

Changes in the former are introduced through variations in the definition of the bond-order,

$$b_{ij}^{\mathrm{LCBOPII}} = \frac{1}{2}\left[\tilde{b}'_{ij} + \tilde{b}'_{ji}\right] + \tilde{F}^{\mathrm{conj}} + A_{ij} + T_{ij},$$

where, in particular, $\tilde{F}^{\mathrm{conj}}$ is augmented to describe the occurrence of multiple fractional bonds, and A_{ij} and T_{ij} are added to account for the presence of occupied anti-bonding states and torsional terms.

The inclusion of a middle-range coordination-dependent term is aimed at improving the performance of the force-field in complex coordination situations and to describe bond-breaking and bond-formation events. The reference database include dissociation curves for the triple, double and single bonds in $(CH_3)C{\equiv}C(CH_3)$, $(CH_3)_2C{=}C(CH_3)_2$ and $(CH_3)_3C{-}C(CH_3)_3$ respectively, obtained with the GGA Becke-Perdew xc functional.

3.2.2 ReaxFF

The Reactive Force-Field (ReaxFF) [112] corresponds to a general and comprehensive scheme, originally developed for hydrocarbons, and later extended to systems of diverse types of bonding, from covalent to metallic . [113–116] In particular, a specific parametrization was performed to describe the catalytic formation of carbon nanotubes. [117]

The ReaxFF potential energy is written as

$$E^{\mathrm{ReaxFF}} = E_{\mathrm{bond}} + E_{\mathrm{over}} + E_{\mathrm{under}} + E_{\mathrm{lp}} + E_{\mathrm{val}} + E_{\mathrm{tor}} + E_{\mathrm{vdW}} + E_{\mathrm{Coulomb}}.$$

The different terms represent the bond energy, energy penalties due to over- and under-coordination and the presence of lone-pairs, bond-angle explicit dependence and torsional contribution, as well van-der-Waals and Coulomb interactions.

The concept of bond-order is crucial also in this approach and all interaction terms explicitly depend on its value (b^{ReaxFF}), apart from E_{vdW} and E_{Coulomb}. In particular, the bond energy is written as

$$E_{\mathrm{bond}} = -D b_{ij}^{\mathrm{ReaxFF}} \exp\left(p\left(1-(b_{ij}^{\mathrm{ReaxFF}})^{p}\right)\right),$$

where D and p are constants. However its definition differs from the REBO and related potentials and is given by

$$b_{ij}^{\mathrm{ReaxFF}} = b_{ij}^{B} f_1(\Delta_i', \Delta_j') f_4(\Delta_i', b_{ij}^{B}) f_5(\Delta_j', b_{ij}^{B}),$$

where b_{ij}^{B} is the bare bond order, further decomposed as

$$b_{ij}^{B} = b_{ij}^{\sigma} + b_{ij}^{\pi} + b_{ij}^{\pi\pi},$$

where each of the b_{ij}^{x} has the form of an exponential and the f_is (ranging from 0 to 1) introduce corrections depending on the deviation (Δ_i') of the sum of all bond orders around the ith-atom with respect to its nominal valency.

E_{vdW} is approximated with a sum of Morse potentials and E_{Coulomb} as a sum of modified point-charge Coulomb interaction terms:

$$E_{\mathrm{Coulomb}} = \sum_{i<j} C \frac{q_i q_j}{\left[r_{ij}^{3} + \gamma_{ij}^{-3}\right]^{1/3}},$$

where C, and γ_{ij} are constants and the atomic charges (q_i) are calculated using a charge equilibration method.

For hydrocarbons, [112] parameters were adjusted to reproduce a database including empirical heats of formation, bond lengths and bond angles, complemented by DFT-B3LYP calculations. In the construction specific to simulate the catalytic formation of nanotubes, [117] an additional

term was incorporated in the energy expression so as to help destabilize the carbon dimer and the training set was extended to include results of DFT-B3LYP calculations on the relative stabilities of different nanotubes.

3.3 Simulation of Rare Events

Rare events in chemical physics are processes which involve barriers significantly greater than thermal energy fluctuations. Because the probability to find the system in a state decreases exponentially with the energy of the state, the time needed to wait (in an MD simulation) for a system spontaneously overcome such barriers increases exponentially. To speed up such calculations a number of techniques exist and in this section I will describe the methods applied in this thesis for this purpose.

3.3.1 Nudged Elastic Band

The Nudged Elastic Band (NEB) method is a method to compute the potential energy barrier for activated processes by finding a transition state between an initial and final state. In the NEB method a collection of N images, each with their own set of coordinates R_i, is used to form a path between the initial and final state. An initial guess for such a path may for example be obtained by linear interpolation of coordinates between the reactant and product.

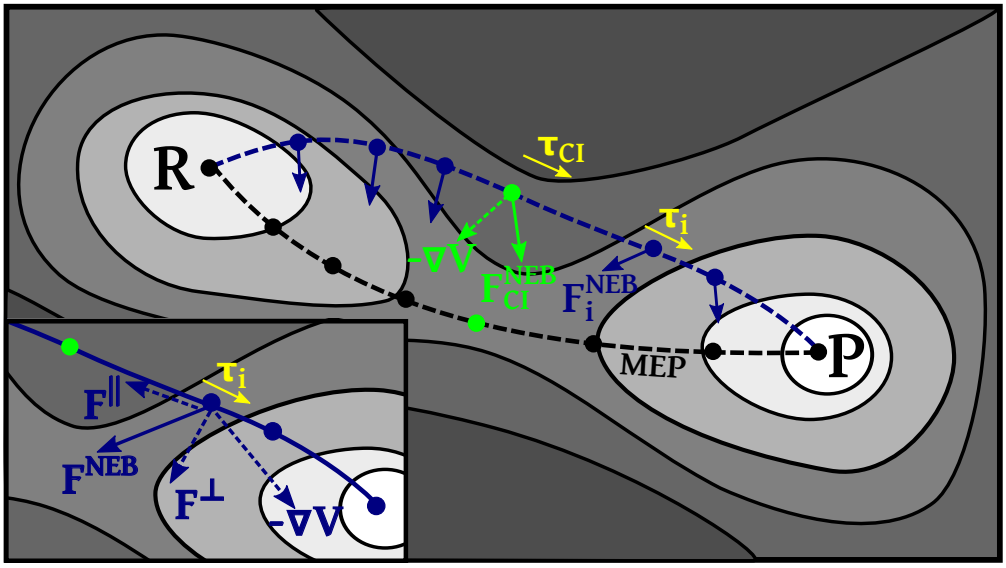

Figure 3.1: Illustration of the Nudged Elastic Band method. Evaluation of the image forces on the potential energy surface (gray background), forces from the potential energy surface use dashed lines and NEB forces with solid lines. Circles represent images with the climbing image in green.

The force on each image then consists of two parts: (i) in the direction parallel to the path ($\hat{\tau}_i^{\parallel}$) a spring force is applied to keep the image separation constant and (ii) in the direction perpendicular ($\hat{\tau}_i^{\perp}$) to the path minus the force from the potential energy surface is applied

so that the path converges to a minimum energy path with the highest point close to the transition state between the two minima. Thus the total force in the NEB scheme on image $i \in \{2,3,\ldots,N-1\}$ may be expressed as

$$\mathbf{F}_i^{\mathrm{NEB}} = \underbrace{-(\nabla V \cdot \hat{\tau}_i^{\perp})\hat{\tau}_i^{\perp}}_{\text{perpendicular}} + \underbrace{-k_i\left(|R_i - R_{i-1}| - |R_{i+1} - R_i|\right)\hat{\tau}_i^{\parallel}}_{\text{parallel}}.$$

The first and last image are generally either kept fixed, or are otherwise subject to the forces from the potential energy surface. It can easily be seen that the forces on all images are zero exactly when (i) the path follows the steepest descent path so that $\nabla V \cdot \hat{\tau}^{\perp} = 0$ and perpendicular forces are zero, and (ii) the images are equally spaced so that the parallel forces are zero. The direction $\hat{\tau}^{\parallel}$, defining the path, can be defined from linear differences or neighbouring image coordinates or more sophisticated approaches such as a spline interpolation between different images. The spring constants k_i may be further adjusted to increase the accuracy in the description of the transition state. The NEB method is a local optimization, and therefore does not necessarily converge to the global minimum energy transition state.

3.3.1.1 Climbing image

Because the replicas are equally spaced, the highest point does not necessary correspond to the exact transition state. In order to overcome this problem, one of the replicas may act as a climbing image (CI).[118] The CI does not experience the spring forces but instead is pushed in the direction of the transition state as illustrated in Fig. 3.1. The forces on the CI are given by

$$\mathbf{F}_{\mathrm{CI}}^{\mathrm{NEB}} = -\nabla V + 2(\nabla V \cdot \hat{\tau})\hat{\tau}.$$

If the starting path is a NEB path without CI, switching on the CI will thus make this image climb to the transition state.

3.3.2 Metadynamics and the Choice of Collective Variables

Energy barriers at finite temperature are more complicated to compute in general. To obtain a well converged *free* energy landscape, an accurate sampling of the phase space is necessary. For this purpose a variety of different sampling methods exist (see e.g. Ref. 119). In this thesis work I have used metadynamics[120] for this purpose, a dynamical non-equilibrium sampling method. During a metadynamics run a bias is slowly added to the potential energy (making this is a non-equilibrium method) which enables the system to overcome barriers. The added bias potential consists of (small) Gaussian hills placed at regular time intervals, so that the total history-dependent biased potential is given by

$$V^{\mathrm{bias}}(\zeta) = V^{\mathrm{pot}}(\zeta) + \sum_{i<n} h \exp\left(-\frac{|\zeta - \zeta_i|^2}{2\sigma^2}\right),$$

where ζ is some collective variable able to distinguish reactants from products. The choice for the h and σ depend on the studied system. Metadynamics can serve two different purposes: (i) to explore possible rare events and predict inexpensive free energy pathways for the system to evolve and (ii) to estimate free energy barriers between different states of the system.

3.3.3 Collective Variables

For metadynamics to work in practice, a set of *collective variables* (CVs) specific to the process must be specified that are able to follow the evolution of the activated process from reactants to products. These CVs must be chosen with care and their construction is a non-trivial procedure in general. Some basic examples of CVs include for example the bond length between two atoms to study a bond-breaking process, or the atom density to simulate a phase transition. To assess the validity of the chosen collective variables and convergence of the free energy barrier several criteria exist. First, several crossings of a barrier must be observed to obtain convergence, where after some time parallel growth of the bias profile must observed. Hysteresis would otherwise indicate a hidden slow degree of freedom not included in the simulation. A more stringent test (commitor analysis) can be performed *a posteriori*, once the relevant state basins (initial, intermediates and final) and transition states are identified as is done in the work of Geissler et al.[121] This consists of generating many short MD-runs starting from each sample in the putative transition state with random initial velocities. If the chosen CVs are a good approximation of the true reaction coordinate, the trajectories from each sample will fall into A or B with probability $1/2$, if this is not the case then the chosen CVs are inadequate for the system.

Path Collective Variables The Path Collective Variables (path-CVs[122]) are a set of coordinates to simulate the transition between two known metastable states (A and B) of the system, similar in spirit to the NEB procedure. First an initial guess for path $\mathbf{R}_{\text{path}}(\tau)$ is constructed, where τ goes from 0 to 1 as $\mathbf{R}_{\text{path}}$ changes contiuously from the product to the react coordinates. Then, given the atom coordinates $\mathbf{R}$, two CVs are defined, one parallel (s) and another perpendicular to the path (z)

$$s(\mathbf{R}) = \frac{\int_0^1 \tau \exp\left[-\lambda(\mathbf{R}_{\text{path}}(\tau)-\mathbf{R})^2\right] d\tau}{\int_0^1 \exp\left[-\lambda(\mathbf{R}_{\text{path}}(\tau)-\mathbf{R})^2\right] d\tau}, \tag{3.21}$$

$$z(\mathbf{R}) = \frac{-1}{\lambda} \log \int_0^1 \exp[-\lambda(\mathbf{R}_{\text{path}}(\tau)-\mathbf{R})^2] d\tau. \tag{3.22}$$

The perpendicular coordinate (z) allows the simulation to sample not merely along the originally constructed path, but also to discover new paths passing through different transition states in the vicinity of the original path, a significant advantage over the local optimization nature of the NEB method. In practice, the parameter λ is chosen such that different states

are numerically well separated, which is achieved if

$$\lambda\langle\mathbf{R}_{\text{path}}(\tau)-\mathbf{R}(t))^2\rangle \approx 1.$$

Moreover the path is normally discretized so that the integrals are to be replaced by sums.

SPRINT The SPRINT (Social Permutation Invariant) coordinates[123] are a set of collective variables. To each atom is assigned a scalar coordinate sensitive to the topology of surrounding network of chemical bonds, which can be used to push topological change and explore different chemical structures. The sprint-coordinates (**S**) are defined as the product of the principal eigenvector $\mathbf{v}_n$ and corresponding eigenvalue λ_n of the $(n \times n)$ contact matrix D which defines the connection of atoms i and j through a switching function going smoothly from 1 to 0, where n is the number of atoms included for the calculation of **S**.

$$\mathbf{S} = \sqrt{N}\,\lambda_n \text{ sorted}(\mathbf{v}_n) \tag{3.23}$$

In order to perform molecular dynamics simulations not only the vector **S**, but also the forces on each atom resulting from the bias potential $V_{\text{bias}}(\mathbf{S})$ are needed. We therefore need to compute the derivatives with respect to atomic coordinates x_i. Using perturbation theory one can show that a small change in the matrix D, δD, leads to a perturbative change in the eigenvalues ($\delta\lambda$) and eigenvectors (δv) given by

$$\delta\lambda_n = \langle\mathbf{v}_n|\delta D|\mathbf{v}_n\rangle, \tag{3.24}$$

$$\delta\mathbf{v}_n = \sum_{\alpha\neq n}\left\langle\mathbf{v}_\alpha\left|\frac{\delta D}{\lambda_n-\lambda_\alpha}\right|\mathbf{v}_n\right\rangle\mathbf{v}_\alpha. \tag{3.25}$$

The bias force on atom $i = 1,\ldots,N$ can then be computed using

$$F_i = -\frac{d}{d\mathbf{x}_i}V_{\text{bias}} = -\sum_{\alpha,\beta,\gamma}\frac{\partial V_{\text{bias}}}{\partial s_\alpha}\frac{\partial s_\alpha}{\partial D_{\beta\gamma}}\frac{\partial D_{\beta\gamma}}{\partial\mathbf{x}_i} \tag{3.26}$$

The computational complexity of the forces from SPRINT coordinates ($\mathcal{O}(n^4)$) can noticeably slow down MD simulations with more than ~ 100 atoms. To reduce the complexity of this calculation we have parallelized this code. Details on this implementation are given in Appendix A.

4 Chemisorption

In this chapter we study the chemisorption of different adducts on CNT sidewalls using DFT. The adducts we consider include hydrogen and oxygen as well as species isoelectronic to oxygen: NH, CH_2, SiH_2 and sulphur. Using large-scale DFT calculations we estimate the thermodynamic stability of different chemisorption configurations and correlate different configurations to (electronic and vibrational) spectral fingerprints. Our DFT results are further compared to classical force-field predictions — AIREBO is used for hydrogen chemisorption and ReaxFF for oxygen.

4.1 Hydrogen

4.1.1 Status of Simulations and Models

Several calculations have been published on the chemisorption of hydrogen on CNT surfaces. Table 4.1 summarized the methods used in referenced work. The predicted binding energies and structural characteristics are summarized in Table 4.2. Atomic hydrogen chemisorbs on top of a carbon atom, creating an sp^3-like hybridized carbon.[11,124] B3LYP calculations[11] on armchair CNTs have shown exohedral chemisorption to be favoured over endohedral by ~ 1 eV for a 1-nm diameter CNT. Endohedral chemisorption moreover becomes increasingly disfavoured at smaller diameters until it finally becomes unstable for CNTs with a diameter smaller than ~ 0.5 nm. Chemisorbed hydrogen atoms are thermodynamically expected to favour clustering: going from one isolated chemisorbed H to 100 % coverage, binding energies are predicted to increase slightly. GGA and hybrid functionals were found to predict comparable chemisorption structures and energetics in this case.[124] However intermediate coverages have received little attention so far. Other DFT calculations[48,125,126] considered the chemisorption of two hydrogen atoms from the dissociation of molecular hydrogen. Specifically, calculations using the PW91 (GGA) functional[125] found binding energies in between 1.8 and 2.0 eV, with the most favourable structure having two H atoms on neighbouring sites of a double bond along the (10,0)-CNT axis. GGA calculations in Ref. 48 found hydrogen chemisorption to lead to a nodal structure in the differential electronic density where the cusps correspond to energetically favourable chemisorption sites. The occurrence of double peaks in the local DOS as a result of chemisorbed hydrogen pairs was further proposed as explanation for the double-peak structures observed in STS measurements. However this

Reference	Functional	Algorithm	CNT [N]
[124]^a	LSDA	AE	(10,0) [40]
[124]^b	PBE[85]	AE	(10,0) [40]
[124]^c	HSE03[128]	AE	(10,0) [40]
[129]	PW91[130]	UPP[131]	(10,0) [40]
[125]	PW91	AE-DND	(10,0) [80]

Table 4.1: Methods and models used in various referenced papers. CNT models are H-terminated with the exception of Ref.124 which uses PBCs. Note: DND=double-numerical-depolarised basis functions; UPP=ultrasoft pseudopotentials.

Ref.	n	C_h	E_B (eV)	d(C–H) (Å)	d(C–C) (Å)
[124]^a	1	(10,0)	1.9	1.119	1.511, 1.484
[124]^b	1	(10,0)	1.5	1.116	1.534, 1.502
[124]^c	1	(10,0)	1.5	1.085	1.522, 1.493
[125]	2	(10,0)	2.0	1.10	1.56, 1.52
[129]	1	(10,0)	2.7	1.087	1.556, 1.572

Table 4.2: Literature results: number of chemisorbed H atoms (n), tube chirality (C_h), binding energy (E_B), and typical distances (d). For n=2 only the most stable configurations are reported here.

analysis did not refer to the most stable configuration.

Hydrogenation of SWNTs was also studied with molecular dynamics and Monte-Carlo simulations using the AIREBO force-field[127] over a range of concentrations up to full coverage. The authors concluded that hydrogen atoms and also non–hydrogenated sites tend to cluster leading to a rippled surface morphology. However no clear evidence was brought up and the binding energy found to monotonically decrease up to full coverage in parallel with the behaviour for a random distribution.

4.1.2 Clustering on the (10,0)–CNT: Structures, Energetics and Mechanisms

We have studied hydrogen chemisorption on the (10,0)–CNT sidewall[132] using a CNT model containing 240 C atoms of which the outermost are H_2 saturation. We verified selected calculations using 360 C atoms in a periodic orthorhombic cell of length (38.40 Å) and a perpendicular box length of 21 Å. Our main DFT results refer to the PBE xc functional. We investigate the effect of this approximation by performing several calculations with another GGA (BLYP) and hybrid functional (PBE0). We compare our *ab initio* results to predictions from the AIREBO forcefield.[109] Details of the methods are given in Appendix C.

Fig. 4.1 shows the system configurations that we considered. Binding energies and geometric characteristics for the lowest energy configurations (series (a)) are given in Table 4.3. In good agreement with previous work, chemisorption of a single H atom induces a strong rehybridization of the carbon orbitals leading an sp^3–like hybridized structure. Geometrically

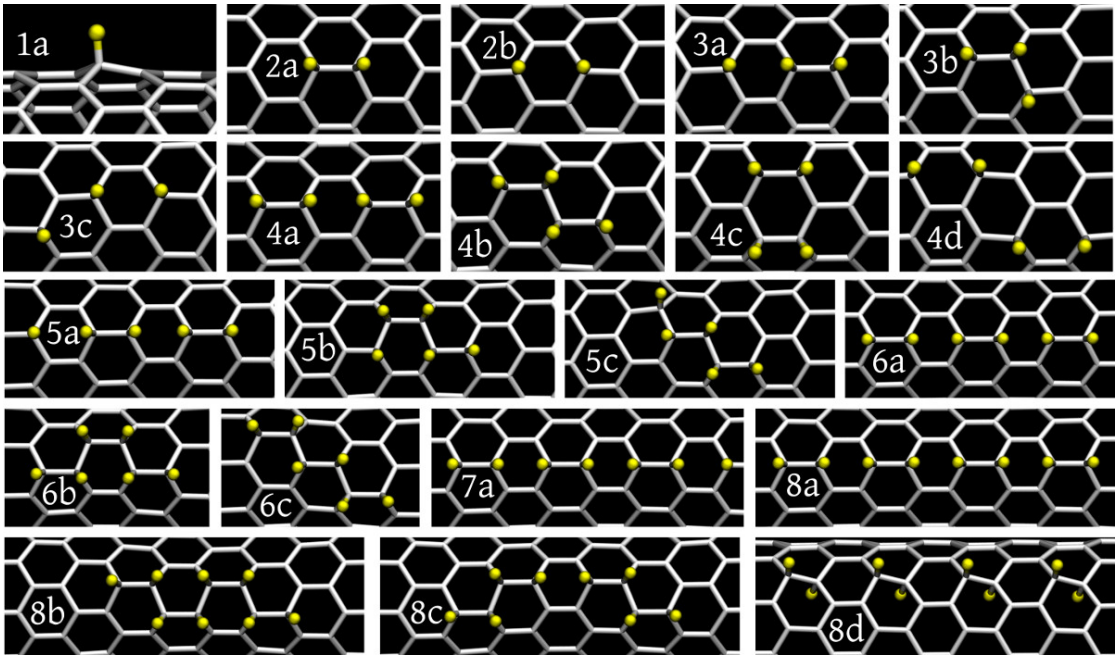

Figure 4.1: CNT:nH, all configurations considered here for the systems with n=1 (side view) and n=2–8 (top view). Note that in 8(d), both exohedrally and endohedrally chemisorbed hydrogens are present.

this is characterised by an increase in the C pyramidalization angle[133] from 5° to 17°. The binding energy, defined as $E_B(n) = (E(\text{CNT}) - E(\text{CNT}+n\text{H}))/n + E(\text{H})$, shows a monotonic increase with n and an energy gain for $n = 8$ of more than 0.7 eV, indicating a strong tendency for the H atoms to cluster on the CNT surface rather than remaining sparse. In Tables 4.4 and 4.5 the binding energies, deformation energy (E_D, defined as the energy difference between the pristine CNT and the carbon lattice in the CNT:nH configuration) and the confinement energy gain ($E_C = E_B(n) - E_B(1)$) are given for the various configurations considered and compared to calculations with the AIREBO potential. Two general observations can be made on the basis of these results. First, results from other xc functionals (specifically BLYP) leave our conclusion on clustering unmodified. Calculations with the PBC model show slightly lower binding energies (differences are less than 0.1 eV). These differences can be understood from the artificial strain due to periodicity. Second, the classical potential (AIREBO) fails to reproduce both binding and deformation energies accurately. Most importantly, AIREBO does not predict H atoms to cluster on the surface ($E_C < 0$).

To understand why these specific pattern are favoured it is instructive to look at changes in charge density as shown by the differential Mulliken population (ΔMP, between the pristine and hydrogenated CNT) in Fig. 4.2. The covalent adsorption of one H atom (top panel) by the formation of a C–H σ–bond leads to a negative differential charge (-0.175) on the C attached to H. This perturbs the π–system and leads to a charge wave around the defect. An excess charge density (ΔMP=0.03) accumulates on the C atom in the ortho–position (leading to 2(a)) while the para–position (2(b)) is deprived of charge (ΔMP=-0.02). This explains why the 2(a) configuration is favoured for subsequent attack by H chemisorption. Moreover the

n(conf)	E_B	d(C–H)	d(C–$C^\star_x$)	d(C–$C^\star$)	α(C*CH)	β(C*CC*)	θ
1	1.64	1.120	1.501	1.522	108; 106	109; 114	17.0
2(a)	2.13	1.109	1.558	1.526	106	106; 116	16.0
3(a)	2.13	1.113	1.556; 1.500	1.525	106.5	106; 115	16.5
4(a)	2.28	1.109	1.560	1.526	107	106; 116	16.6
5(a)	2.23_5	1.112	1.550; 1.493	1.526	107	105; 116	16.7
5(b)	2.22	1.110	1.559; 1.498	1.516; 1.583	104; 106	113; 114	14.8
6(a)	2.34	1.109	1.556	1.527	107	104; 116	16.7
7(a)	2.27	1.111	1.557; 1.498	1.527	107	104; 116	16.8
8(a)	2.38_5	1.109	1.555	1.527	107	103; 116	16.8

Table 4.3: Binding energies (E_B in eV/H), bond lengths (d in Å), angles (α, β in deg.) and pyramidalization angles (θ in deg.) for the lowest energy configurations in Fig. 4.1. For $n > 2$ averages are given when values are close. C indicate the carbon atoms bound to H and C* only to carbon.

	n (conf)									
	1	2(a)	2(b)	3(a)	(3b)	3(c)	4(a)	4(b)	4(c)	4(d)
E_B (QM)	1.64	2.13	1.85	2.13	2.05	1.73	2.28	2.23	1.88	1.85
[PBC]	1.56	1.97	1.90	1.99	1.97		2.11	2.07		
[BLYP]	1.65	2.16	1.87	2.14	2.09		2.29	2.26		
E_D (QM)	-0.76	-0.52	-0.76	-0.84	-0.842	-0.83	-0.86	-0.72	-0.86	-0.73
E_C (QM)		0.48_5	0.21	0.48_5	0.41	0.09	0.64	0.59	0.24	0.21
[PBC]		0.41	0.34	0.43	0.41		0.55	0.51		
[BLYP]		0.51	0.23	0.49	0.44		0.64	0.62		
E_B (A)	3.13	2.82	3.12	2.92	2.82	2.91	2.82	2.79	2.40	3.13
E_D (A)	-1.23	-1.08	-1.25	-1.13	-1.06	-1.22	-1.06	-1.05	-1.12	-1.26
E_C (A)		-0.31	-0.01	-0.21	-0.31	-0.22	-0.31	-0.33	-0.73	0.00

Table 4.4: Chemisorption configurations for n=1–4 : binding energies (E_B) per H atom and corresponding loss due to deformation (E_D) and "confinement" gain (E_C) for DFT–PBE (QM) and AIREBO (A). DFT–PBE results are further compared to our PBC model and the BLYP functional.

mechanical deformation energy (E_D) is 0.24 eV smaller in the 2(a) configuration than for 2(b) which further favours the 2(a) site. The PBE energy difference of 0.3 eV between 2(a) and 2(b) remains unchanged when considering the PBE0 and M06 functionals. This result agrees with previous GGA calculations[23,125,126] but the mechanism and sizeable difference were not explained before.

4.1.3 Electronic and Vibrational Signatures

In Refs.23 doublets were found in the experimental DOS which were associated with hydrogen dimers by calculations on several high–energy isomers of CNT-2H. The ground state structure 2(a) was not considered and 2(b) was not found to induce any perturbations in the gap.

Our calculations with PBCs show an interesting scenario. The gap of the pristine CNT with PBE is 0.78 eV. When a single hydrogen is chemisorbed, it creates an impurity state 0.2 eV above the highest occupied molecular orbital level (HOMO) of the pristine CNT . If hydrogen

	n (conf)											
	5(a)	5(b)	5(c)	6(a)	6(b)	6(c)	7(a)	7(b)	8(a)	8(b)	8(c)	8(d)
E_B (QM)	2.22	2.23_5	2.22	2.34	2.31	2.26	2.27	2.29	2.38_5	2.35	2.33	1.92
[BLYP]	2.22	2.24		2.35	2.33		2.28	2.31	2.39	2.37		
E_D (QM)	-0.93	-0.65	-0.68	-1.18	-0.57	-0.59	-1.08	-0.97	-0.63	-0.89	-0.89	-1.68
E_C (QM)	0.58	0.59	0.58	0.70	0.67	0.62	0.63	0.65	0.74	0.71	0.69	0.28
[BLYP]	0.57	0.59		0.71	0.68		0.63	0.66	0.74	0.72		
E_B (A)	2.88	2.78	2.82	2.82	2.77	2.81	2.86	2.77	2.82	2.76	2.80	2.60
E_D (A)	-1.09	-1.03	-1.04	-1.05	-1.01	-1.03	-1.08	-1.01	-1.04	-0.99	-1.04	-1.41
E_C (A)	-0.25	0.35	-0.31	-0.31	-0.36	-0.32	-0.27	-0.35	-0.31	-0.37	-0.33	-0.33

Table 4.5: Chemisorption configurations for n=5–8 : notation as in Table 4.4.

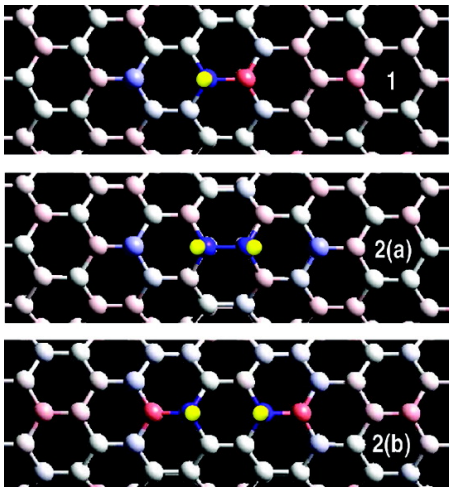

Figure 4.2: ΔMP for 1, 2(a) and 2(b). Red (blue) indicates positive (negative) charge.

atoms were sparsely chemisorbed on the CNT surface, we would thus expect a dispersionless band at this energy. In 2(a) a doublet is found in the DOS which reduces the band gap by 0.3 eV. On the contrary, in 2(b) the gap remains that of the pristine tube (within 0.02 eV). The corresponding states are shown in Fig. 4.3. For (2a) the HOMO is simply that of the bare tube, whereas the lowest unoccupied molecular orbital (LUMO) corresponds to the impurity state and is more localized around the chemisorption region. In 2(b) occupied impurity levels are found 0.6 and 0.2 eV below the HOMO and in the unoccupied states at 1.1 eV above the HOMO. This 1.3 eV splitting corresponds well with the 1.4 eV calculated in Ref.23.

The gap is further reduced for configurations with four hydrogen atoms to 0.3 eV for both the 4(a) and 4(b) configuration. The HOMO (Fig. 4.4A for 4(a)) is delocalized and the LUMO (Fig. 4.4B and C for 4(a) and 4(b) respectively) has a larger amplitude near the chemisorption region. At 0.6 eV below the HOMO, impurity levels are again found in both configurations. An example of these impurity levels is shown for 4(b) in Fig. 4.4D. Upon increasing the number of chemisorbed hydrogen atoms further to 6H and 8H, the gap is reduced to 0.2 and 0.02 eV respectively, with similar characteristic levels as for the 4(a) isomer.

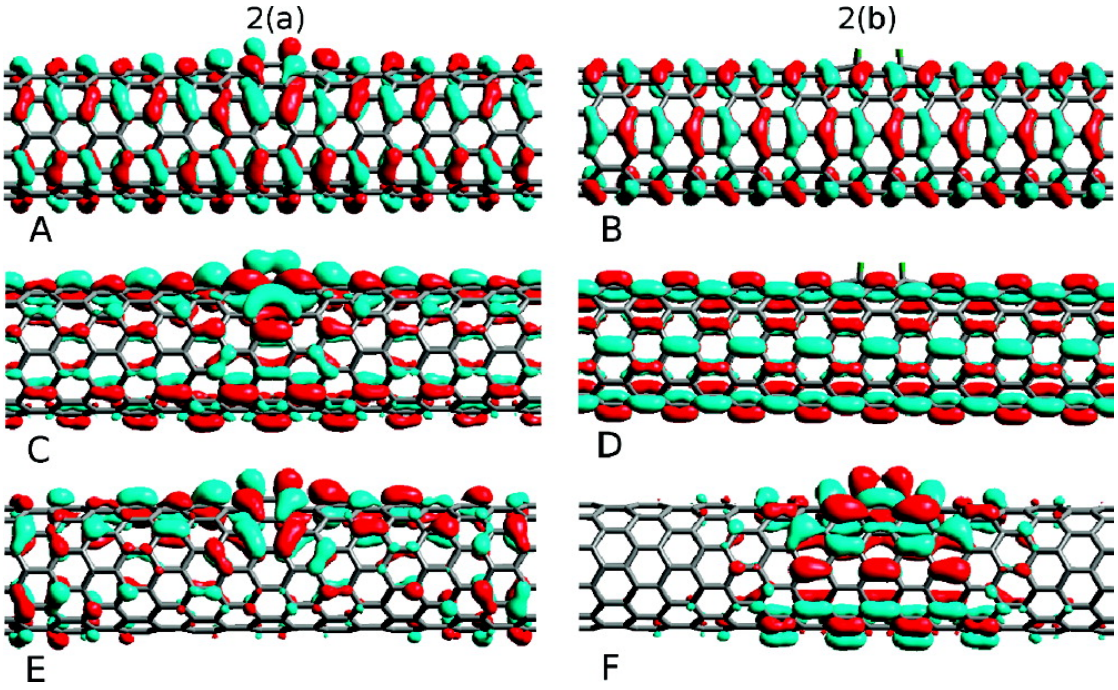

Figure 4.3: Wavefunction isosurface of the HOMO (A, B), LUMO (C, D) and occupied impurity state (E, F) in 2(a) (left) and 2(b) (right).

Despite that DFT–PBE calculations are known to systematically underestimate the size of the band gap, we can conclude that the gap tends to decrease with increasing number of chemisorbed hydrogen atoms by simultaneously destabilizing the HOMO levels and stabilizing the LUMOs. This will eventually lead to closing of the gap at some critical number/concentration $n_c(>8)$.

Finally we computed the infrared active spectrum in the harmonic approximation. We used the CH_2 terminated CNT model to enable comparison with experimental spectra on CNT systems[20,22] that contain not only CH units but also hydrogen atoms bonded to undercoordinated carbons at defect sites and at the ends of suspended CNTs. The infrared spectrum of 4(a) is shown in Fig. 4.5. To understand the effect of the CH_2–groups at the end we projected out their contributions.

The CH stretching modes are easily detectable as they separated by a gap of about 1200 cm^{-1} from the C–only modes which end near 1600 cm^{-1} in agreement with typical IR CNT spectra.[134] This part of the spectrum, shown in detail in the inset of Fig. 4.5, is bimodal. The first peak, at 2780 cm^{-1}, corresponds to symmetric stretching of the CH_2 groups. The second peak, at 2890 cm^{-1}, comprises both the asymmetric CH_2 stretching modes as well as the four CH stretching modes. We find the oscillator strengths corresponding to symmetric (f_s) and asymmetric (f_a) CH_2 stretching and CH stretching (f_1) in the ratio $f_s : f_a : f_1 = 12 : 4 : 1$. Our observations agree with the experimental findings of Ref. 22 for both the assignment and relative intensities of these two peaks. PBE however predicts too soft modes as usual: in Ref.22 the CH band extends from 2750 to 3000 cm^{-1} with peaks centred at 2850 and 2920 cm^{-1}. Also in

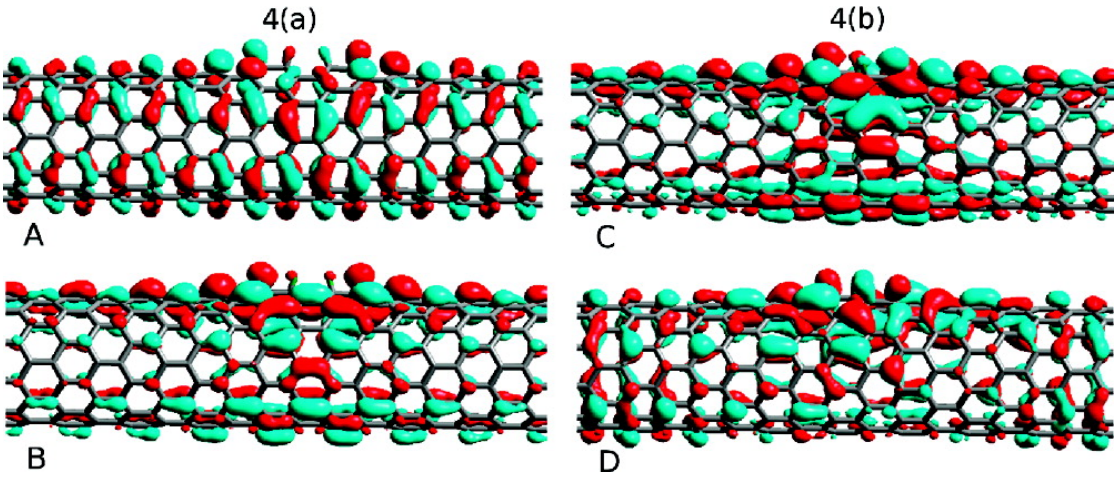

Figure 4.4: Wavefunction isosurface of the HOMO (A) and LUMO (B) for 4(a), and LUMO (C) and HOMO-2 (D) for 4(b).

other measurements[20] the CH stretching modes were assigned to a peak at 2924 cm^{-1}. As long as CH_2 moieties are dominantly present, the overlap of the CH_2 and CH peaks complicates the use of IR spectra for the characterization of hydrogenated CNTs. However, a careful analysis of the fine structure of these two peaks under controlled hydrogenation may allow to distinguish the two groups.

The AIREBO potential is known [1] too predict a more extended CNT vibrational spectrum. In our model, calculated CC stretching frequencies extend to above 1900 cm^{-1}. The AIREBO potential also predict a double peak associated with symmetric and asymmetric stretching of the CH_2 moieties, at 2870 and 2935 cm^{-1} respectively. However the CH stretching overlaps the (softer) symmetric stretching mode, contrary to our DFT results. As a result AIREBO would predict a relative change of intensities inverted with respect our DFT–PBE findings upon hydrogenation.

[1] See e.g. Refs. 127,135. Despite the claimed agreement with DFT calculations, the reported findings are fully in agreement with

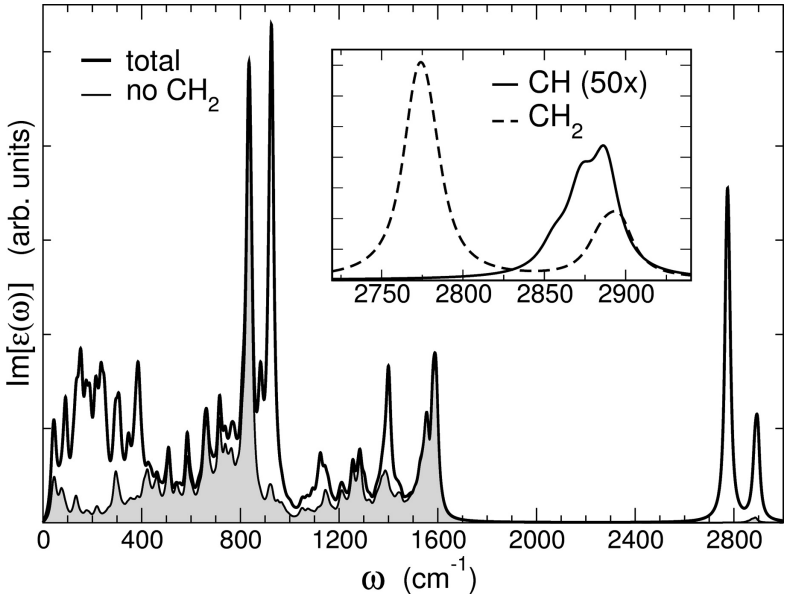

Figure 4.5: Infrared spectrum for 4(a).

4.1.4 Conclusions

Our DFT–PBE results clarify the tendency for hydrogen atoms to cluster on the CNT sidewall. Preferential configurations are moreover identified which can be rationalized by examining the charge redistribution and mechanical strain resulting from chemisorption. These trends are different from those predicted for graphene where only low concentrations are predicted stable.[136] The AIREBO potential fails to capture these differences due to curvature and instead predicts sparsely chemisorbed hydrogen.

We have shown that the electronic states near the gap are strongly modified upon hydrogenation and tends to close gap for the considered coverages. At full coverage however the system is nevertheless expected to be semiconducting[137] due the sp^3–like nature of this system. This can be expected to lead to non–trivial transient response behaviour in CNT based hydrogen sensors. Our DFT–PBE calculation of the CNT:4H infrared spectrum give further clear indications which may aid in the characterization of hydrogenated CNTs and the differentiate CH and CH_2 groups.

4.2 Oxygen and Other [2+1] Cycloadditions

This section summarizes our published work[28,138] on the chemisorption of oxygen and isoelectronic species on SWNT surfaces. After a brief summary of previous calculations we start by considering the case of a single O on the (10,0)-CNT. We then extend our results to (i) determine chemisorption patterns and dynamics on CNTs of different chiralities, (ii) identify fingerprints of adducts in electronic spectra, (iii) and to assess the validity of geometrical descriptors to predict chemisorption products. Our study is further extended to isoelectronic species, specifically sulphur. Finally, we repeat the CNT:O calculations with ReaxFF[117] to compare predictions of this force-field to our DFT results.

4.2.1 Status of Simulations and Models

Carbon chemistry suggests two most probable configurations for an oxygen on a graphitic surface, namely either forming an ether (ET) or an epoxide (EP). In the ET configuration the C-C bond on breaks, whereas in the EP it stays as shown in Fig. 4.6. It is however not *a priori* obvious which one is favored on the sidewall of a given nanotube. Several works have estimated the energy difference between the two adsorbant configurations and aimed to determine criteria for the formation of one or the other. The methods and results of these referenced works are reported in Tables 4.6 and 4.7. However, given the small size of the atomistic models adopted to represent the nanotube, none of these calculations are adequate to assess the energetics of the low-coverage situations.

Reference	Functional	Algorithm	CNT [N]
[139]	PW91	UPP[140]	(3,3) [24], (4,2) [56], (5,0) [20]
[141][a]	PBE	AE	(10,0) [40], (8,4) [112]
[141][b]	HSE03	AE	(10,0) [40], (8,4) [112]
[142]	B3LYP	AE	(4,4) [56]
[143]	B3LYP	AE	(5,0) [40]
[144]	PW91	UPP[131]	(8,0) [32]

Table 4.6: Methods and models used in various referenced papers. Calculations use periodic boundary conditions (PBCs) with the exception of H-terminated models in Ref.s 142 and 143. CNT=pristine nanotube chirality; N=the number of carbon atoms, AE=all-electron, UPP=ultrasoft pseudopotentials.

The effect of curvature on the CNT surface reactivity has been investigated[145–148] for the chemisorption of O and isoelectronic species NH and CH_2. DFT-B3LYP calculations predicted an inverse proportionality of the binding energy to the CNT diameter for armchair CNTs[145] for these adducts. A limiting CNT diameter (of 1.5 nm[146] – 2.4 nm[147]) was moreover identified above which no bond cleavage takes place and thus oxygen can form only EPs. These results have been generalized to CNTs of different chiralities using the concept of local curvature.[148,149] The existence of a limiting curvature dependence for bond cleavage has also led to the proposal of switchable CNT-devices.[150]

Ref.	CNT	ref. O	E_B^{ET}	E_B^{EP}	ΔE
[139]	(3,3)	in O_2	1.97	0.10	1.87
[139]	(4,2)	in O_2	1.77	0.38	1.39
[139]	(5,0)	in O_2	1.06	0.94	0.12
[141]^a	(8,4)	singlet O	6.54	5.69/5.64	0.85/0.90
[141]^b	(8,4)	singlet O	6.04	5.10/5.05	0.96/1.01
[141]^a	(10,0)	singlet O	6.25	6.22	0.03
[141]^b	(10,0)	singlet O	5.73	5.74	-0.01
[142]	(4,4)	triplet O	4.19	2.72	1.47
[143]	(5,0)	triplet O	2.95	2.82	0.13
[144]	(8,0)	triplet O	3.18	3.16	0.02

Table 4.7: Binding energies for SWNT:O. The oxygen reference system (E(O)) is used for the binding energy E_B=E(CNT:O)-E(CNT)-E(O); ΔE=E_B(ET)-E_B(EP). Energies are in eV. In our (PBE) calculations singlet atomic O is 2.23 eV higher in energy than triplet O, and the binding energy of O in (triplet) O_2 with respect to triplet atomic O is 2.81 eV.

For sulfur only a limited number of calculations can be found in literature thus far,[151,152] despite its recognized role in the growth of CNTs.[153] Specifically, DFT-PBE calculations[152] found S to chemisorb with a binding energy of 1.4 eV on the (10,0)-CNT. The binding energy was further found to increase by 0.4 eV if S atoms are chemisorbed in a line along the CNT-axis.

4.2.2 ET versus EP: 1O on the (10,0)-CNT

We first consider the chemisorption of a single O atom on the (10,0)-CNT. Two types of bonds present on the (10,0)-CNT, an armchair- (A) and a zigzag-bond (Z) (see the insets of Fig. 4.6). When O atoms chemisorbs on the A bond it preserves it, whereas chemisorption on the Z bond breaks the underlying bond. The difference in bonding is clearly demonstrated by the electron localization function (ELF), which shows the absence of a bond between the carbon neighbours of oxygen for the ET.

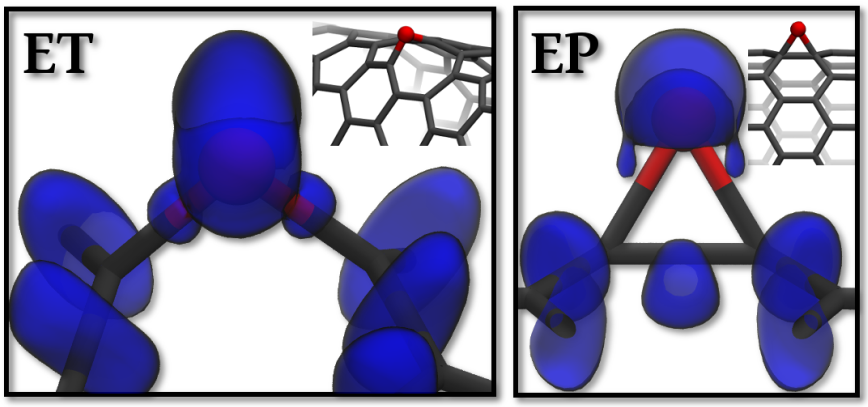

Figure 4.6: ELF (at isovalue 0.8) showing the broken bond in the ET and the bond that remains in the EP. Insets show the (10,0)-CNT carbon network with the bonds on which chemisorption takes place.

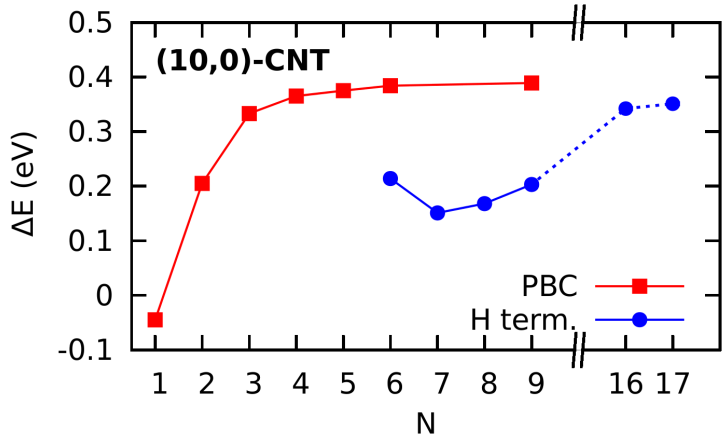

Figure 4.7: Convergence of the energy difference ($\Delta E = E^{\mathrm{EP}} - E^{\mathrm{ET}}$) as function of the number of unit cells (40 C atoms each) for periodic (PBC) and H-terminated models.

Our DFT-PBE calculations predict that the ET is thermodynamically favoured over the EP on the (10,0)-CNT by ΔE=0.4 eV. Fig. 4.7 shows that in order to obtain a converged value for ΔE a cell size containing at least 200 atoms ($N = 5$) is needed. The smallest supercell, containing 40 C atoms ($N = 1$), was used in Ref. 141 where a negligible energy difference of $\Delta E = 0.02$ eV was found. Indeed, our calculations give a similar value[2] for $N = 1$. However it is important to realize that this calculation represents a high density linear row of oxygen atoms, rather than sparsely chemisorption. The same can be concluded for other calculations such as in Ref. 142, where DFT-PW[130] calculations of a 64 C atom model of the (8,0)-CNT lead to a negligible ΔE of 0.02 eV.

We examined both periodic and hydrogen saturated boundary conditions. As expected both models converge to the same energy difference ($\Delta E = 0.4$ eV), however the model sizes needed in the H-terminated model are significantly larger. The slow convergence of H-terminated model can be understood from the perturbation caused by the oxygen chemisorption on the *electronic* rather than the geometric structure. Indeed the binding energy of the EP converges slower than that of the ET, despite that the ET induces a much longer ranged strain field on the CNT structure as shown in Fig. 4.8.

The influence of the exchange-correlation (xc) functional in the prediction of the relative stability of ET versus EP is found small, BLYP and PBE0 calculations give ΔE =0.5 and 0.4 eV respectively. Moreover, the PBE0 geometry optimizations lead to only minor changes from the PBE results: the CNT diameter is reduced by less than 1 % and binding energies are increased by $\sim$ 2%. This agrees with the negligible differences noted between PBE and the hybrid HSE03 functional in Ref. 141.

[2] We find $\Delta E = -0.04$ eV for $N = 1$. These small differences (< 0.1 eV) can easily be ascribed to differences in computational set-up. Most importantly in Ref. 141 a localized all-electron basis set is used, whereas our calculations use a plane wave basis set with pseudopotentials.

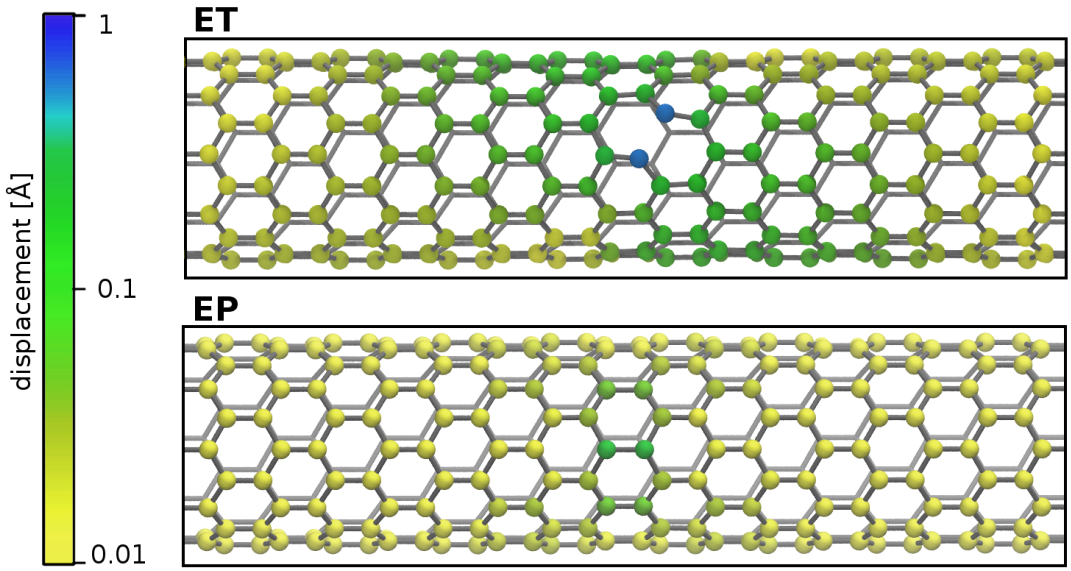

Figure 4.8: (10,0)-CNT:O. Displacement of the C atoms after O chemisorption.

4.2.3 CNT:1O Kohn-Sham Spectra and STS

The Kohn-Sham (KS) density of states (DOS) shown in Fig. 4.9(a) unambiguously reflect the difference between one oxygen as ET or EP adsorbent. The pristine (10,0)-CNT has a PBE bandgap of 0.76 eV. The ET does not significantly alter the π-system and therefore results only in minor changes near the band edges. On the contrary, the EP strongly affects the π-bonding network and induces a new localized impurity state in the gap. This (unoccupied) impurity state, shown in Fig. 4.9(b), is a combination of the oxygen lone pair with the CNT orbitals. In combination with the modifications near the occupied band edge this leads to a $\sim$ 0.3 eV reduction of the gap. Our PBE0 calculations confirm this picture. As usual PBE0 predicts a significantly larger gap for the pristine CNT (1.4 eV), but otherwise the result remains unchanged: a similar impurity state is found near the pristine LUMO resulting in a gap reduction of 0.3 eV when oxygen is chemisorbed as EP.

In Ref.141 both the ET and EP were predicted to lead to a strong gap reduction of 0.35 and 0.20 eV respectively. Our calculations for the small (N=1) cell indeed predict similar gap reductions of 0.4 and 0.25 respectively. The discrepancy with our results presented above can be ascribed to inadequacies of the N=1 CNT model and can be compared neither to our N=9 CNT model, nor to the experimental data presented together with our calculations in Ref.[28] Indeed the gap converges slowly with N as shown in Table 4.8.

In the scanning tunneling microscopy (STM) and scanning tunneling spectroscopy (STS) measurements presented together with our computational results in Ref.28 a large number of defect sites induced by atomic oxygen on semiconducting and metallic SWNTs were considered by the exposure of purified HiPco SWNTs with a defect density below 1 defect per 200 nm to atomic oxygen from a catalytic gas cracker. The oxygen defects are characterised

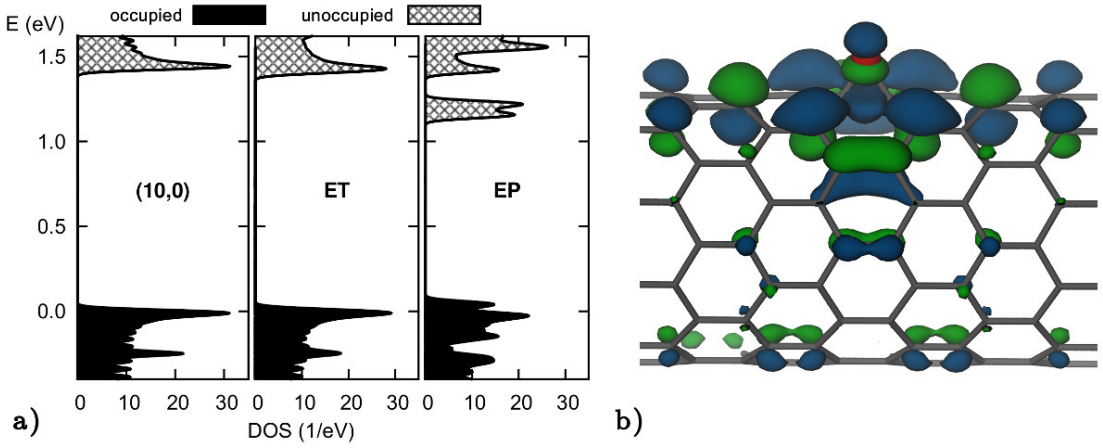

Figure 4.9: (10,0)-CNT:O KS density of states (a) near the band edges. The impurity state (b) is at ∼0.2 eV from the pristine LUMO in the EP.

N	E_g(CNT)	E_g(O-ET)	E_g(O-EP)
1 (Ref. 141)	0.76	0.41	0.56
1	0.78	0.37	0.53
6	0.77	0.73	0.46
9	0.75	0.73	0.43

Table 4.8: (10,0)-CNT:O bandgap (E_g in eV) convergence as function of N (N=1 contains 40 C atoms). In each case k-point convergence is ensured and the transition is a direct gap at Γ.

by hillock type features in the STM topography with typical heights ranging from 0.5 to 2 Å. The STS measured electronic signatures in an energy window of ± 1 eV around the midgap (Fermi) level exhibit significant variations. Clear defect states are frequently observed in the gap of semiconducting tubes above the midgap position. Fig. 4.10 shows an example of such a defect for a sample after exposure to atomic oxygen for four minutes, at a chamber pressure of $1.2{\cdot}10^{-7}$ mbar and 40 W heating power of the gas cracker. STM (Fig. 4.10(a)) reveals the atomically resolved structure of a SWNT close to an oxygen induced defect whose image has a spatial extent of 1.3 nm fwhm (full-width at half maximum) in the topography and a height of 0.85 Å. The corresponding STS map is shown in Fig. 4.10(b), away from the defect. The typical density of states (DOS) of a semiconducting SWNT can be recognised, with an E_{11} gap of 1.1 ± 0.1 eV and the valence band edge of the E_{22} gap at -0.4 eV. The chirality of this nanotube, estimated from E_{11} and a chiral angle $\theta = 19 \pm 2°$, is either (8,3) or (7,3). At the defect position a state is identified at 0.3 eV below the conduction band edge of the pristine nanotube and is strongly localized in energy (80 meV fwhm). These characteristics correspond well to the impurity levels that our calculations identified as fingerprints of the EP sites.

Our theoretical findings clearly show that ETs are thermodynamically favoured but that STS cannot distinguish them from the pristine CNT regions. To understand why EPs are detected in STS experiments, we computed the energy barrier that an oxygen should overcome to go from EP on the armchair bond to ET on the zigzag bond. Our NEB calculation gives a PBE

barrier of 0.8 eV for this process, which shows that an oxygen atom could indeed be kinetically trapped in this metastable state at low temperatures. The functional dependence on this result is small: BLYP gives a barrier of 0.6 and PBE0 (at PBE geometries) a barrier of 0.7 eV.

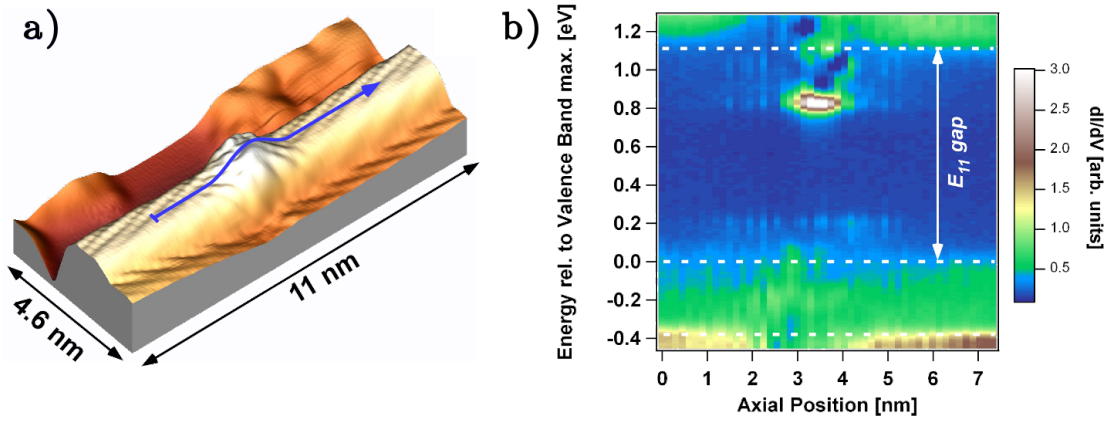

Figure 4.10: STS-map of a semiconducting CNT showing an impurity state assigned to atomic O. The image is composed of 50 individual dI/dV spectra with a 1.5 Å spacing.

Finally, we remark that midgap levels in the STS could also be associated with the presence of vacancies. DFT calculations[43] have predicted that vacancies, both single and double, would generate characteristic states near the Fermi level. These results were used to interpret STS data on SWNTs subjected to Ar^+ ions bombardment. Our calculations of single and double vacancies on the (N=9) (10,0)-CNT confirm these findings. However, vacancies give rise to strong electron scattering,[154] which was not observed in the experiments discussed here. The low concentration as well as low kinetic energy of the impinging oxygen atoms ($\sim$ 0.1 eV) further support our conviction that the probability of finding generated vacancies was negligible.

4.2.4 Dependence on Concentration and Chirality

To establish the dependence of our results on the CNT diameter we considered a range of zigzag nanotubes with diameters (D) from 0.6 to 1.5 nm, i.e. $(n,0)$-CNTs with n from 8 to 19. We also considered the (8,4)-, (6,5)- and (12,10)-CNT (chiral angles of 19° and 27°) as representative of other chiralities. All chiralities considered correspond to semiconducting tubes. Our CNT models contain ~300 to ~700 atoms in an orthorhombic cell (a,b,b) with a between 34 and 41 Å and b between 21 and 30 Å. For zigzag CNTs this corresponds to the N=9 model for the (10,0)-CNT of the preceding section. The diameters of SWNTs obtained from high pressure CO disproportionation (HiPco) range from 0.8 to 1.2 nm.[155] Our considered range of CNT diameters exceed this 1.2 nm (extending to ~1.5 nm) to attempt comparison with graphene.

To investigate the dependence on concentration, we consider adsorbate configurations consisting of n=1 to 4 oxygen atoms on the (10,0)-CNT. We find that with increasing CNT length, from 240 to 360 to 480 C atoms, the binding energy of four oxygen atoms increasing from

2.99 to 3.10 to 3.11 eV. Therefore our calculations on the (10,0)-CNT use a 360-atom unit cell. Binding energies E_B are given per adduct and relative to the atomic (triplet) ground state of oxygen. Deformation energies E_D are total energy differences of the deformed carbon structure with respect the pristine CNT. We use the aggregation (or confinement) energy E_C, defined as the difference in E_B with respect to the ET configuration, to quantify the tendency to cluster.

On all $(n,0)$ tubes of diameter D<1.2 nm ($n < 16$) we find that an ET forms on the zigzag-bond (Z) and that this is thermodynamically favoured over the EP on the armchair bond (A) as shown in Fig. 4.11(a). Also on the (8,4) and (6,5)-CNT bond cleavage takes place on one bond only. With increasing diameter the surface flattens, up to the point where the zigzag-bond can no longer sustain the cleavage for $D > 1.2$ nm. Indeed, in the limiting case of graphene only the EP is stable.[148,156,157] Fig. 4.11(b) shows the variation of the two C-C bond lengths relative to the pristine tube. As long as significant difference exists between the two bonds, the most stable site remains the Z-bond, despite that it generates a more sizeable (localized) strain on the sidewall (Fig. B.1). In the (17,0) the corresponding deformation energy E_D is 0.15 eV higher than with oxygen on the A-bond, and the binding energy E_B is 0.2 eV higher. These values should be compared to an E_D difference of 2.4 eV in the (10,0)-CNT where the Z-bond is broken and the ET is more strongly bound than the EP by 0.4 eV.

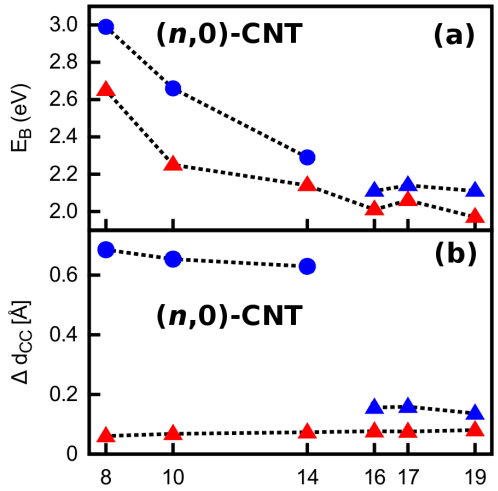

Figure 4.11: $(n,0)$-CNTs. Variation of (a) the oxygen binding energy and (b) C-C bond-length on Z (blue) and A (red) bonds as a function of n. Circles and triangles refer to ETs and EPs respectively.

Fig. 4.12 illustrates the low-energy oxygen configurations on a (10,0)-CNT with between one and four oxygen atoms. Other configurations at higher energy are shown in Fig. B.2. In each of the configurations shown in Fig. 4.12 for n=2, 3 and 4, the binding energy (E_B) per oxygen is higher than for sparsely chemisorbed ETs (n=1). Oxygen atoms thus show a clear tendency to cluster in these configuration, especially when aligned as in 4a. If we consider aggregates consisting of only EPs (Fig. B.2), also EPs tend to cluster, however the resulting binding energies remain below that of sparse ETs. On the (8,4)-CNT, we considered n=1 and 2 (Fig. 4.13), and again we find two aligned ETs to correspond to the lowest-energy structure 2a while two EPs

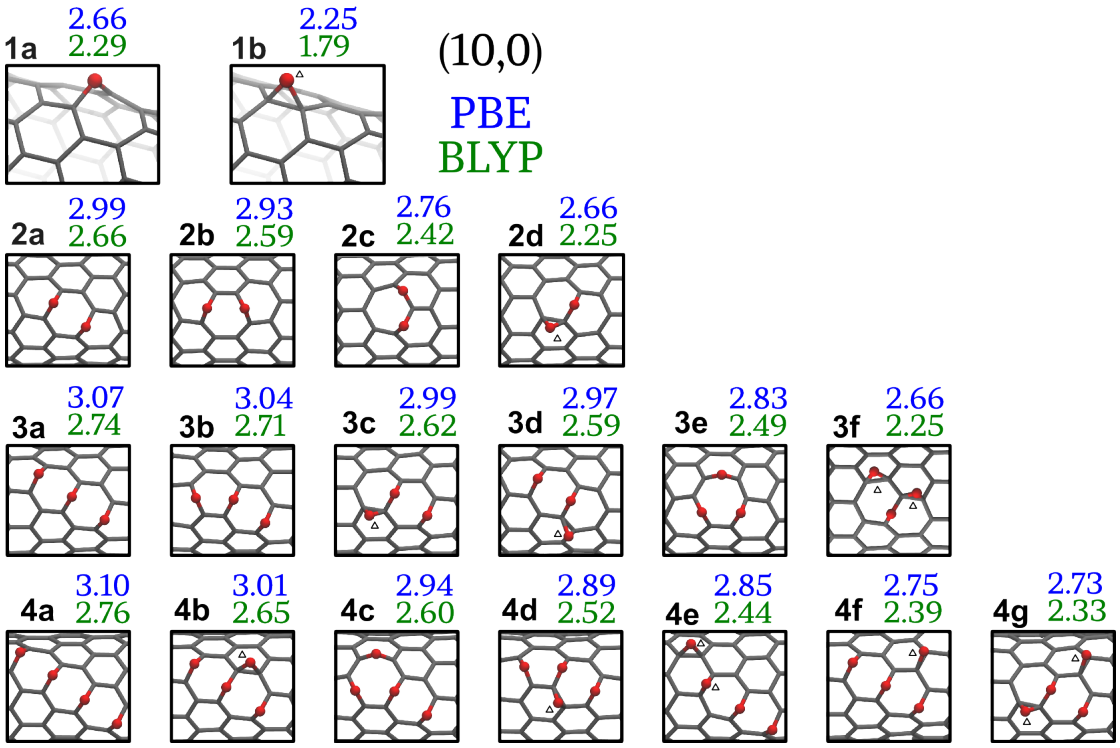

Figure 4.12: (10,0)-CNT:nO (n=1–4). Structures of chemisorbed oxygen for n=1 and for all cases with aggregation energy E_c >0. Binding energies (in eV) refer to triplet O. A small triangle indicates an EP.

(see e.g. 2f in Fig. B.3) are highly disfavoured.

BLYP binding energies (in Fig.s 4.12, 4.13, 4.14, 4.15, B.2 and B.3) are lower than the PBE values by ∼15%. However, the two GGA functionals are in close agreement for the prediction of the clustering energy and energetic ranking of configurations. Small differences are found in the predicted geometric characteristics (see Tables B.2, B.3 and B.4). PBE0 calculations on the PBE geometries resulted in a decrease of the binding energies of 0.4–0.5 eV.

On tubes of diameter larger than that of the (10,0) and (8,4) (D=0.8nm) ETs remain dominant. Considering only one oxygen, we would predict that for $D > 1.2$ nm no bond opening is allowed and only EPs are found. However, with increasing concentration the EPs are destabilized with respect to ETs and clustering may lead to bond cleavage. In Fig. 4.15 stable configurations on the (17,0) are shown. The lowest energy configuration is again a linear chain of ETs. The associated aggregation energy is moreover to be higher than in the case of the (10,0). Fig. 4.16 shows the pattern of atom displacements in the adsorbate with four aligned ETs 4a and in one with two aligned ETs and two EPs 4e. The presence of EPs in 4e decreases the energy loss E_D due to structural deformation by 1.4 eV relative to 4a. In spite of it, in analogy with the n=1 case on CNTs of higher curvature, the electronic contribution dominates the binding energy and here favours 4a by 0.2 eV. For structural characteristics see Table B.5.

It should be emphasized that our findings regarding the thermodynamic preference for ETs is in agreement with NEXAFS and infrared spectroscopy measurements[26] on oxidized SWNTs

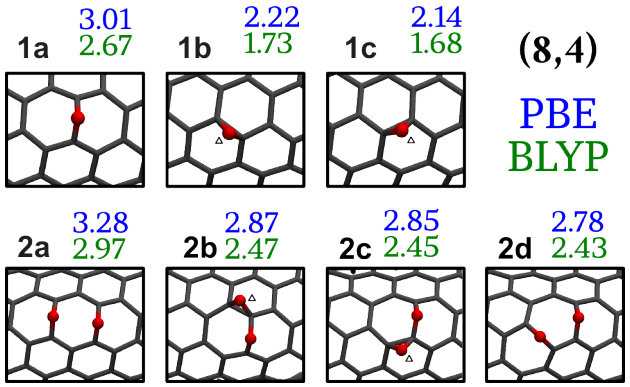

Figure 4.13: (8,4)-CNT:nO. Structures of chemisorbed oxygen for n=1 and for all cases with aggregation energy E_c >0. Notation as in Fig. 4.12.

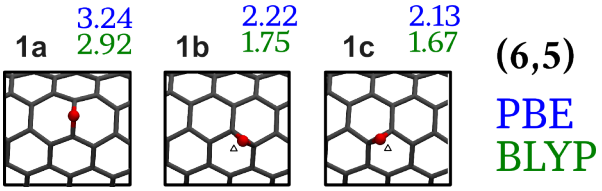

Figure 4.14: (6,5)-CNT:nO. Structures of chemisorbed oxygen for n=1. Notation as in Fig. 4.12.

that revealed a higher relative stability for ETs.

The nanotubes with diameters exceeding 1.2 nm should be relevant to a discussion of limiting case of a flat graphitic surface (graphene). Similar to our calculations on the (17,0)-CNT, the most stable structures for n=2 and n=3 on graphene also consist of ETs,[157] but having a remarkably different energetic ranking of configurations. Such predictions on graphene are however strongly dependent on the employed graphene model.[148,156,157] For example, calculations on a $C_{54}H_{12}$ as "a piece of graphene"[148] predict that two aligned ETs (2a in Fig. 4.12) are the preferred configuration and that in particular this is 0.05 eV lower than the two EPs as in 2e in Fig. B.2. On the contrary, calculations using a periodically extended surface[157] predict two NNN EPs and three ETs on the same hexagonal ring (2e and 3e of Fig. B.2 and 4.12 respectively) to be the thermodynamically favoured with an energy gain of 0.2 eV and 0.6 eV compared to the aligned ET pair. As mentioned above, in the case of a (17,0)-CNT, we again find the aligned ETs as ground state configuration for n=2, 3 and 4. Moreover, the EP pair in 2e is even higher in energy than two isolated oxygen atoms and the 3e is slightly higher than the ground state (by less than 0.1 eV). Given that Ref. 157 uses the same PBE functional and a computational scheme very similar to ours, we could conclude that there is still a qualitative difference in the reactivity to oxygen of graphene and nanotubes of diameter 1.3nm. Experiments on SiC-supported graphene[158] seem to suggest a uniform oxygen distribution and "relatively long-range perturbation of the surface electronic structure around the chemisorbed oxygen" which, as we have shown for O on the (10,0)-CNT and will show in more generality below, is characteristic of EPs only.

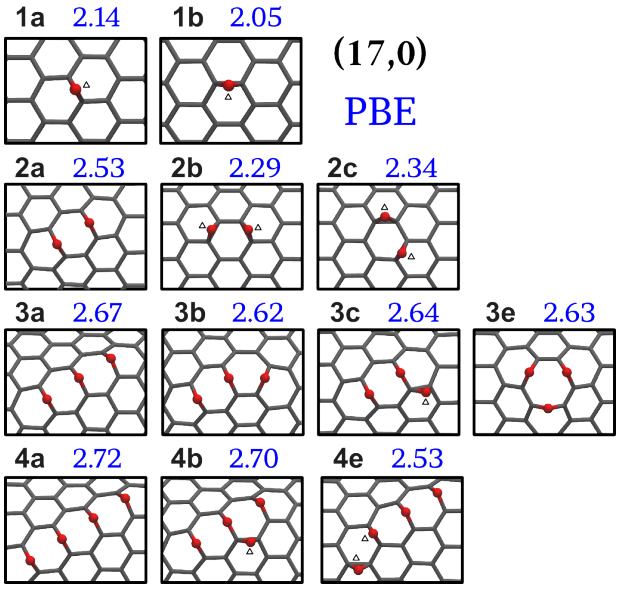

Figure 4.15: (17,0)-CNT:nO (n=1–4). Structures of chemisorbed oxygen for n=1 and for selected configurations with aggregation energy E_c >0. Notation as in Fig. 4.12.

4.2.5 Kinetic Barriers: Trapping and Hopping

In the case of a single oxygen (n=1 on the (10,0)-CNT) we have remarked that the adsorbent could be easily trapped in the (metastable) EP configuration because of the high energetic barrier to diffuse to the nearest-neighbour (NN) zigzag site. On the (10,0) tube, the (PBE) energy barrier is as high as 0.8 eV. On passing to the (14,0)-CNT, despite a significant decrease in ΔE (the EP-ET energy difference) from 0.4 to 0.2 eV, we find that the barrier increases by 0.1 eV. The transition state (TS) for the hopping barriers corresponds in both cases to a configuration where the oxygen is on top of a carbon atom, with both Z and A bond-lengths of ∼1.5 Å.

Next we considered how the oxygen hopping barrier is modified in the presence of other oxygen atoms. In particular, we considered the transitions: 2d to 2b and 4e to 4a that both involve one and two EPs respectively, adjacent to an ET. The paths of these transformations confirm the role of the on-top positions as transition states. In particular, Fig. 4.17 reveals a two-step mechanism, namely the oxygen detachment from one of the carbon atoms is preceded by the EP to ET transformation on the zigzag bond. In both 2d to 2b and 4e to 4a transitions, the barriers are still of the order of 1 eV (Table 4.9). We can then conclude that also in the presence of other oxygens in an ET or in aligned ETs, an additional oxygen can still be easily trapped in an EP configuration. Other types of transformations, involving oxygen hopping between one ET to another ET on a different bond may imply even larger barriers. As an example, Fig. 4.18 illustrates the transition from 2b to 2a, that goes through an intermediate (2f in Fig. B.2) involving an EP.

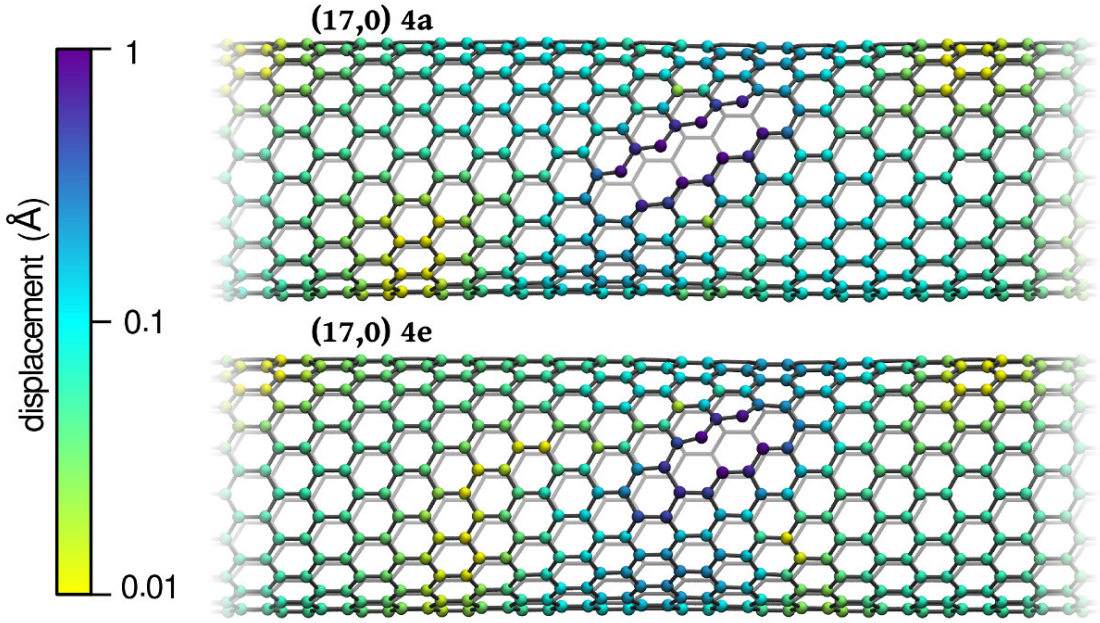

Figure 4.16: (17,0)-CNT:4O. Displacements (in Å) of the C atoms induced by oxygen chemisorption.

I [conf]	F [conf]	$\Delta E^{\star}$
1b [EP]	1a [ET]	0.8
2b [ET]	2a [ET]	1.8†
2d [EP]	2b [ET]	1.2
4e [EP]	4a [ET]	0.7

Table 4.9: (10,0)-CNT. Energy barriers $\Delta E^{\star}$ (in eV) for the hopping of one oxygen from an EP or ET in structure (I) to an ET in a lower-energy isomer (F).
† This value refers to the higher barrier of the two-step mechanism shown in Fig. 4.18.

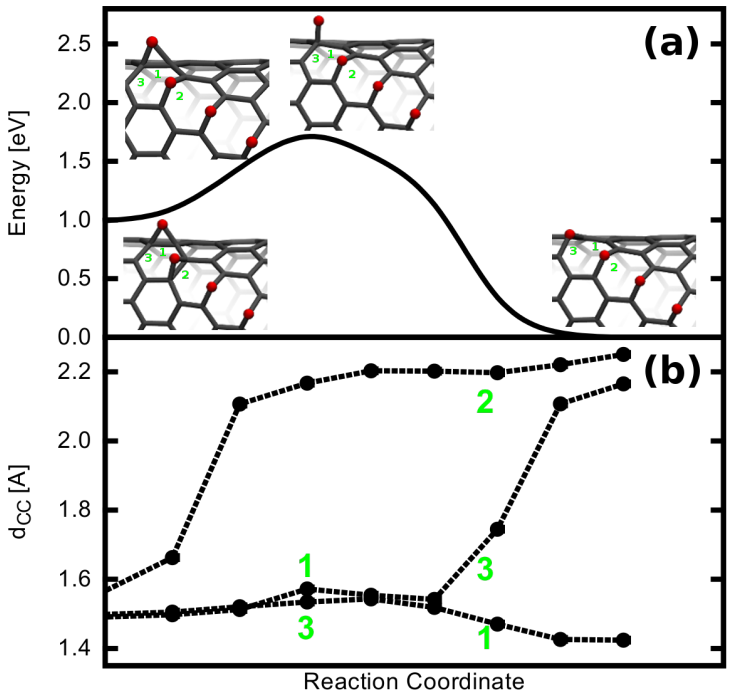

Figure 4.17: (10,0)-CNT:4O - Transformation from 4e to 4a (see Fig. 4.12). (a) Energy profile and sketch of the relevant structures; (b) Variation of the relevant distances.

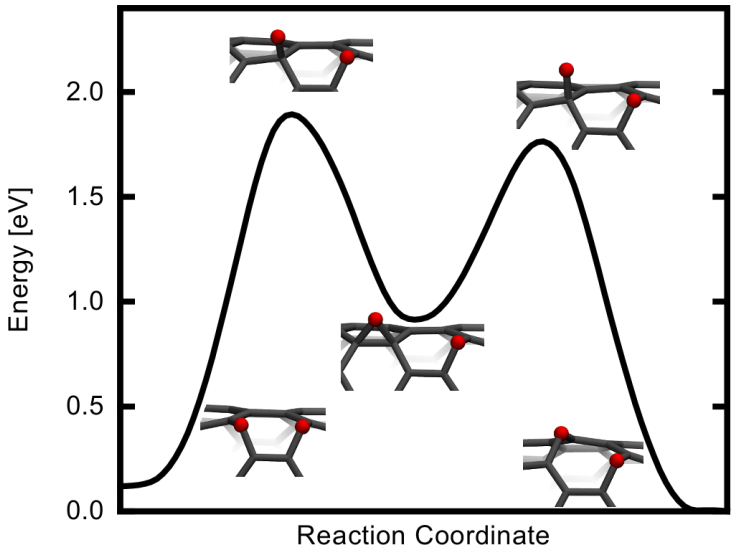

Figure 4.18: (10,0)-CNT:2O - Transformation from 2b to 2a (see Fig. 4.12). Energy profile and sketch of the relevant structures.

Kohn-Sham Electron States. For the (10,0)-CNT we showed that an ET leaves the KS-DOS essentially unperturbed at the band edges, whereas an EP generates a peculiar impurity level in the gap of the pristine tube. A more complex scenario appears to emerge from our results for the (17,0)-CNT. Here, as we have seen above, both the A and Z lead to an EP (Fig. 4.15) but in neither case is a level seen in the gap of the pristine nanotube (Fig. B.4). On the other hand, the (16,0)-CNT exhibits the same behaviour as the (10,0)-CNT. The (8,4)- and (6,5) nanotubes — which both have three inequivalent bonds, two of which lead to an EP (Fig.s 4.13 and 4.14) — show a midgap impurity level only for one specific bond (see e.g. Fig. 4.19 for the (6,5)-CNT).

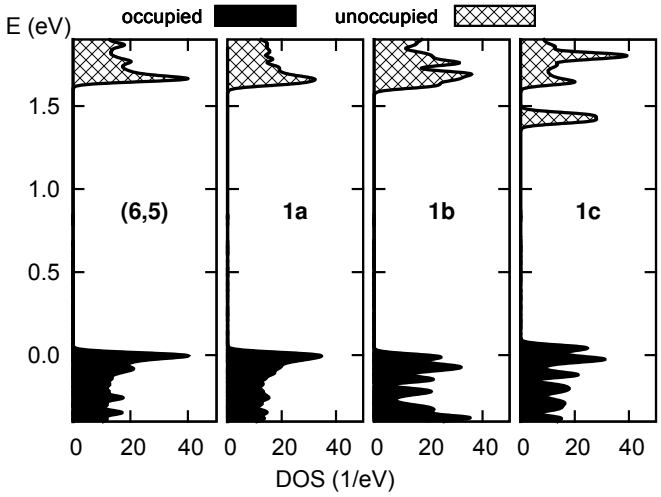

Figure 4.19: (6,5)-CNT:O KS density of states (left) near the band edges.

This situation is only apparently complicated because it has a simple explanation. The appearance of an unoccupied level below the conduction band of the nanotube depends both on the spatial localization of the low-lying unoccupied levels of the nanotube and on the coupling strength with the chemisorbed atom. In the zigzag pristine nanotubes, the π-states can be classified as "delocalized over" one type of bond or the other. This is not always the case in the chiral ones, in which they can be "delocalized over" two out of three types of bond. Still the sequence depends on the characteristics of the tube. In the zigzag class this is governed by mod(n,3) and is thus the same for (10,0) and (16,0)-CNTs, where it is located on the Z-bonds, but different for the (17,0)-CNT, where it is on the A-bonds. Some examples are shown in Fig. 4.20. This clarifies, for example, why the formation of an EP involving the A-bond as in 1(b) hybridizes with the LUMO and thus tends to localize and lower the corresponding energy level. The coupling strength diminishes with the tube diameter. On passing from the (10,0) (D=0.79nm) to the (16,0)-CNT (D=1.26nm), the LUMO-shift diminishes from 0.3 to 0.1 eV. On the contrary, in the (14,0) and (17,0)-CNTs, the HOMO is on the A bonds whereas the LUMO is on the Z-bonds. Also, in both (6,5) and (8,4) nanotubes the LUMO is on one specific bond (the one of lowest curvature again) and is shifted by 0.25 eV when an oxygen is chemisorbed there (corresponding to the 1c in Fig.s 4.13 and 4.14).

With increasing concentration, clustered-ET configurations continue to elude spectroscopies in the range of the gap of the CNT, as well as EPs on bonds of relatively high curvature (Z-sites

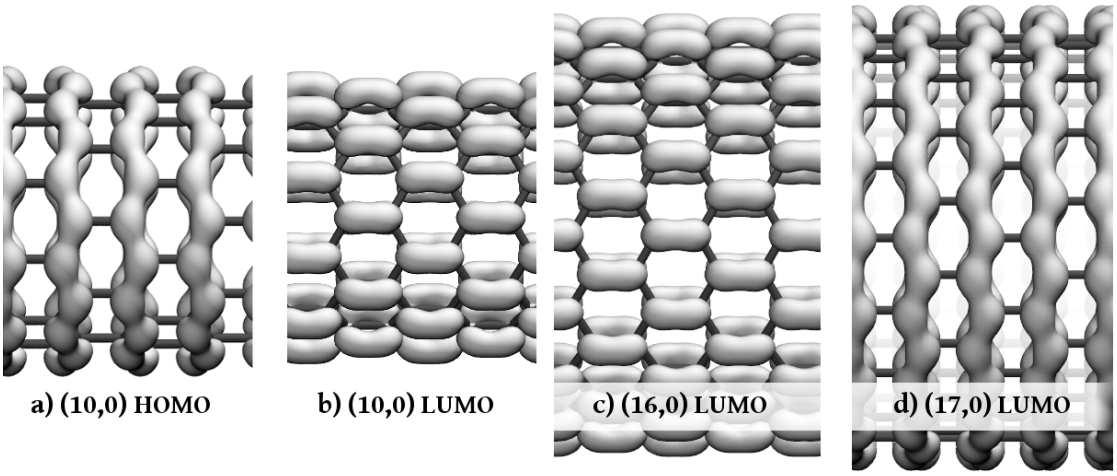

Figure 4.20: Electronic density of the (10,0) HOMO (a) and (n,0) LUMOs (b-d). Isovalue=0.0003 (au)$^{-3}$.

in the (n,0)-CNTs), whereas fingerprints of EPs on bonds of relatively low curvature can still be recognised. In analogy with the case of the (10,0)-CNT,[28] we find that in the (16,0)-CNT:4O EPs on the A-sites continue to generate dispersionless bands in the gap (see Fig. 4.21 (a) and (b)), whereas in the (17,0)-CNT:4O (see Fig. 4.21(c)), due to weaker coupling, the EPs-related states are at the conduction band-edge (see, for example, Fig. 4.21(d) for the 4e structure).

The effects of clustering on inequivalent positions is manifest in the distribution of the 2s-oxygen levels, located about 3 eV below the rest of the valence bands. In the case of one oxygen, we find a clear separation — from 0.3 to 0.7 eV — between different configurations, depending on the specific nanotube. These values would thus correspond to isolated dispersed ET/EP groups. On the other hand, in adsorbates with 4O on the (n,0)-CNTs the four dispersionless bands cover an interval ranging from 0.8 eV for relatively distant groups (e.g., the four aligned ETs in the 4a structure) to 1.8–1.9 eV for mixed arrangements with two groups on adjacent bonds (bonding-antibonding splitting).

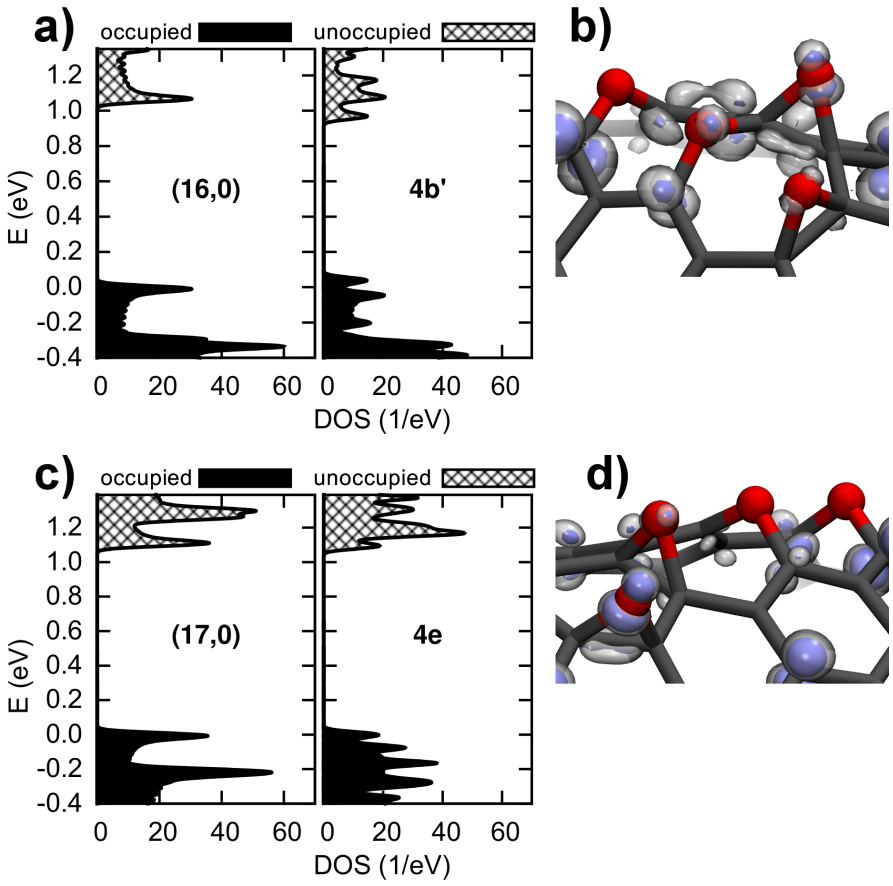

Figure 4.21: DOS (a and c) and probability density (b and d) corresponding to the LUMO in two adsorbate structures with mixed ET and EP populations. Isosurfaces=0.0012, 0.002 $(au)^{-3}$.

4.2.6 Chemical Descriptors

The chemical anisotropy of carbon nanotubes has attracted great interest and has resulted in the proposal of several descriptors for an *a priori* understanding of their chemical behavior. In particular, the "directional curvature" (K_D) introduced in Ref.148, has provided a valuable tool for prediction of ET versus EP formation of sparse [2+1] adducts such as oxygen or methylene (CH_2), as well as trends in reactivity and binding energies for ETs. K_D refers to a pristine SWNT and is defined as in Fig. 4.22, where α is the angle between the bond direction and the CNT-axis. Thus, for any bond type on a SWNT of a fixed chiral angle, the value of K_D depends only on the tube diameter. Here we identify an angle Θ_B, as in Fig. 4.22, that is also related to the "curvature" of a given bond and can be more easily updated for any deformation of the SWNT structure. We verified that in pristine tubes Θ_B and K_D are proportional (see Fig. 4.22) and thus there is no difference between their predictions for a single [2+1] adduct (see Table B.4). Since any chemisorption event induces a local deformation, we can use Θ_B — referred to the bare bond (without O attached) — to answer the question: “Given an adsorbate with a certain concentration, will a certain C-C bond open or not if an additional oxygen binds to it?”. First we considered an oxygen chemisorbed on a coronene molecule and bent it so that

SWNT	bond	d^i_{cc}	Θ_B	B.O.	d^f_{cc} [conf.]	pred.
(8,0)	Z	1.43	57	1.21	2.12 [ET]	ET
	A	1.42	0	1.31	1.48 [EP]	EP
(10,0)	Z	1.43	46	1.23	2.08 [ET]	ET
	A	1.42	0	1.29	1.49 [EP]	EP
(14,0)	Z	1.43	33	1.24	2.06 [ET]	ET
	A	1.42	0	1.29	1.49 [EP]	EP
(16,0)	Z	1.43	29	1.25	1.58 [EP]	EP
	A	1.42	0	1.28	1.50 [EP]	EP
(17,0)	Z	1.43	27	1.25	1.58 [EP]	EP
	A	1.42	0	1.29	1.50 [EP]	EP
(19,0)	Z	1.42	24	1.25	1.56 [EP]	EP
	A	1.42	0	1.28	1.50 [EP]	EP

Table 4.10: One oxygen on semiconducting (n,0) nanotubes. Z=zigzag; A=axial; d^i_{cc} and d^f_{cc} are the bond-lengths prior to chemisorption (pristine tube) and in the adsorbate configuration (ET or EP) respectively. Values (in Å) are from PBE calculations. pred = prediction based on limits defined for oxygen on coronene. Both Θ_B (in degrees) and B.O. refer to the pristine tube. Both give the same prediction for the final configuration.

Θ_B would vary in the range 0–80 °. The transition from EP to ET is sharp and takes place at $\Theta_B = 32°$. Our calculated limits are in the range 29°–33° for Θ_B (see Table 4.10) — in perfect agreement with the case of coronene — and 1.13–1.37 nm^{-1} for K_D. This is in good agreement with the limit value of 1.5 obtained in Ref. 148, where different models, DFT functional and basis set were used.

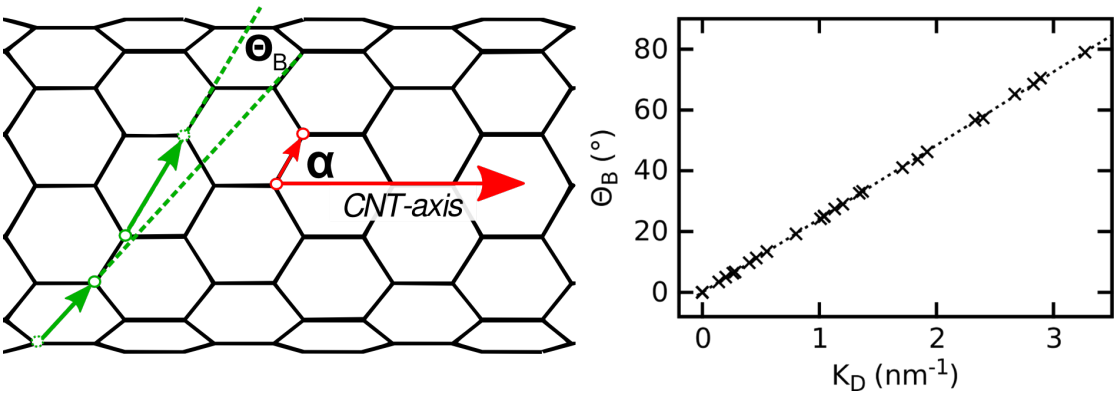

Figure 4.22: Curvature : definition of the "directional curvature" K_D and of the "bond curvature" Θ_B. K_D is defined as $\frac{\sin\alpha}{D}$, with D = the tube diameter.

Any structural parameter, be it a local curvature or bond-length, contains a complex information, with both geometrical and electronic ingredients. The notion of bond-order (B.O.), instead, is directly related to the local electronic configuration. One may as such expect a lower B.O. to be symptomatic of ET formation. Therefore we also examined to what extent the

from	bond	d^i_{cc}	Θ_B [pred]	B.O. [pred]	to	d^f_{cc} [conf]
1a	Z	1.45	53 [ET]	1.25 [ET]	2a	2.20 [ET]
1a	Z	1.45	53 [ET]	1.19 [ET]	2b	2.18 [ET]
1a	Z	1.42	58 [ET]	1.32 [EP]	2c	2.17 [ET]
1a	A	1.45	12 [EP]	1.28 [EP]	2d	1.47 [EP]
1b	Z	1.49	53 [ET]	0.98 [ET]	2d	2.27 [ET]
1b	Z	1.41	46 [**ET**]	1.37 [EP]	2e	1.55 [EP]
1b	A	1.41	0 [EP]	1.35 [EP]	2i	1.48 [EP]
1b	A	1.41	5 [EP]	1.35 [EP]	2j	1.48 [EP]
1b	Z	1.43	46 [ET]	1.23 [ET]	2k	2.07 [ET]
2a	Z	1.44	63 [ET]	1.28 [**EP**]	3a	2.18 [ET]
2a	Z	1.46	54 [ET]	1.15 [ET]	3b	2.20 [ET]
2a	A	1.39	14 [EP]	1.36 [EP]	3c	1.46 [EP]
2a	Z	1.41	55 [**ET**]	1.37 [EP]	3d	1.54 [EP]
2b	Z	1.45	53 [ET]	1.25 [ET]	3b	2.19 [ET]
2c	Z	1.43	53 [ET]	1.32 [EP]	3d	2.21 [ET]
2d	Z	1.47	55 [ET]	1.19 [ET]	3c	2.23 [ET]
2d	A	1.44	8 [EP]	1.31 [EP]	3f	1.52 [EP]
2i	Z	1.49	56 [ET]	0.99[ET]	3f	2.28 [ET]
3a	Z	1.44	53 [ET]	1.29 [**EP**]	4a	2.17 [ET]
3c	Z	1.43	53 [ET]	1.36 [**EP**]	4b	2.18 [ET]

Table 4.11: (10,0)-CNT. Example of the building up of the map in Fig. 4.23(a). Notation as in Table 4.10. Here the initial (from) and final (to) contain n and n+1 O atoms respectively. Bold-faced items highlight deviations where the prediction deviates from the obtained configuration.

B.O. — calculated according to Mayer's prescription [159] — can be used to predict the response of a given bond to a [2+1] adduct. The above-mentioned calculation on coronene showed that EPs become unstable on a bond with Mayer B.O. lower than 1.25. Table 4.10 shows that, when using this limit, the predictions from the bare-bond order are correct for all the (n,0) nanotubes we have considered.

Tables 4.11 and 4.12 extend the above concepts to cases of multiple chemisorbed oxygens. With reference to Fig. 4.12, we consider one bare-bond in a CNT:nO adsorbate and verify whether its Θ_B and B.O. values can be used to predict the chemisorption product (ET or EP) in the CNT:(n+1)O structure. The correlation between the final value of the C-C distance and the bare-bond curvature in Fig. 4.23 confirms the predictive value of the latter. We have emphasized with empty symbols special circumstances for which the prediction fails because under the addition of an extra oxygen the local structure changes so that other bonds — near the one targeted — open or close, or, in other words, the final configuration is the result of concerted or multi-step bond reconstructions. Only a few failures are visible: the transformations from 1b to 2e and from 2a to 3d. These cases correspond to "extreme" values of the B.O. (1.37) and show the predominance of the electronic factor in determining whether cleavage takes place.

from	bond	d^i_{cc}	Θ_B	BO	to	d^f_{cc} [conf.]
1a	Z	1.45	33 [ET]	1.16 [ET]	2a	2.19 [ET]
1a	Z	1.41	31 [EP]	1.28[EP]	2b	1.56 [EP]
1a	A	1.41	4 [EP]	1.35 [EP]	2c	1.50 [EP]
1b	Z	1.41	30 [EP]	1.38 [EP]	2c	1.54 [EP]
2a	Z	1.45	37 [ET]	1.29 [**EP**]	3a	2.18 [ET]
2a	Z	1.46	35 [ET]	1.16 [ET]	3b	2.21 [ET]
2a	A	1.39	14 [EP]	1.35 [EP]	3c	1.47 [EP]
2b	Z	1.44	33 [ET]	1.17 [ET]	3b	2.19 [ET]
2b	A	1.40	8 [**EP**]	1.45 [**EP**]	3e	2.21 [ET]
2c	Z	1.40	33 [ET]	1.46 [**EP**]	3e	2.24 [ET]
3a	Z	1.44	38 [ET]	1.30 [**EP**]	4a	2.17 [ET]
3a	A	1.41	18 [EP]	1.33[EP]	4b	1.50 [EP]

Table 4.12: (17,0)-CNT. Notation as in Table 4.11.

from	bond	d^i_{cc}	Θ_B [pred]	BO [pred]	to	d^f_{cc} [conf.]
(8,4)						
n=0	1	1.43	57 [ET]	1.28 [**EP**]	1a	2.08 [ET]
	2	1.43	25 [EP]	1.22 [**ET**]	1b	1.54 [EP]
	3	1.43	6 [EP]	1.26 [**ET**]	1c	1.50 [EP]
1a	1	1.44	65 [ET]	1.31 [**EP**]	2a	2.17 [ET]
1b	1	1.43	55 [ET]	1.27 [**EP**]	2b	2.23 [ET]
1b	1	1.40	59 [ET]	1.40 [**EP**]	2d	2.18 [ET]
1c	1	1.49	65 [ET]	1.01 [ET]	2c	2.25 [ET]
(6,5)						
n=0	1	1.43	65 [ET]	1.29 [**EP**]	1a	2.09 [ET]
	2	1.42	19 [EP]	1.23 [**ET**]	1b	1.52 [EP]
	3	1.42	13 [EP]	1.24 [**ET**]	1c	1.51 [EP]
(12,10)						
n=0	1	1.42	33 [ET]	1.27 [**EP**]	1a	2.07 [ET]
	2	1.42	10 [EP]	1.25 [EP]	1b	1.52 [EP]
	3	1.42	7 [EP]	1.26 [EP]	1c	1.51 [EP]

Table 4.13: Examples on chiral CNTs. Notation as in Table 4.11.

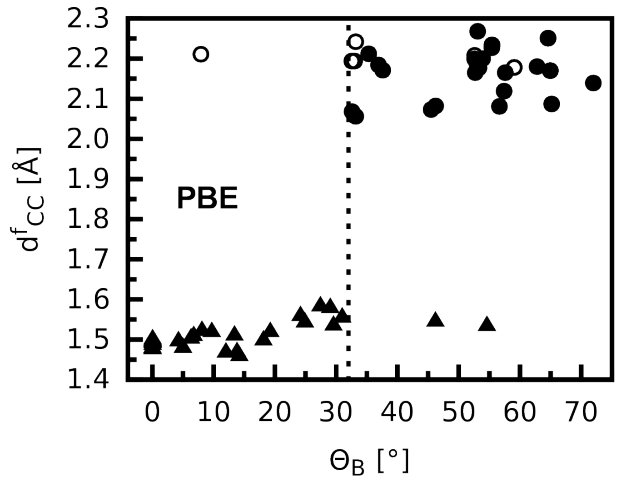

Figure 4.23: C-C distance in the ET or EP groups as a function of the angle Θ_B which refers to the bond before chemisorption. Triangles and open circles represent EPs and ETs respectively. These symbols represent the configurations calculated for oxygen adsorbates on (*n*,0), (8,4), (6,5), (12,10) nanotubes discussed in the text and also the (6,6) bond of fullerene (highest value of Θ_B.).

On the contrary, the B.O., which is highly sensitive to variations in the distribution of the π states, appears to fail more frequently than Θ_B as concentrations increase. However these "failures" can be rationalized. For example, in 2a and 3a the B.O. of the Z-bond aligned with the ETs increases beyond the coronene limit, so that one would not predict an easy cleavage as it happens in 3a and 4a. This increase is more dramatic in 3c, where the Z-bond is near an EP (and two ETs). The threshold could be easily modified from coronene to the CNT domain. On the other hand, failures in correspondence to "extreme" values of the bond curvature can be expected: the structural constraint is then prevailing in the ET vs. EP competition. This is the case of the (6,5)-CNT in which an ET forms on a high-B.O. bond (Table 4.13) where also the variation of B.O.s with bond-lengths is anomalous. Indeed, on passing from zigzag to chiral nanotubes, it is important to note that structural constraints are more severe and in particular do not allow the higher-B.O. bonds to relax. This explains also the case of the (8,4)-CNT (Table 4.13). For large-enough sizes, the Θ_B-B.O. consistency is expected to recover. However, this is not yet the case for the (12,10)-CNT (D=1.50nm) as shown in Table 4.13.

4.2.7 Comparison with ReaxFF

When applied to determine the stable structures of chemisorbed oxygen, ReaxFF presents a serious problem: an arrangement of isolated oxygens on on-top positions is the ground state (I in Fig. 4.24). On the contrary, these structures are unstable in our — and previous[144] — *ab initio* calculations. We notice that in ReaxFF clustering of on-top oxygens is disfavoured; for example pairing on ortho positions as in (IIa) corresponds to a loss of 0.2 eV per atom.

However, if we only compare the geometrical characteristics and the relative stability of

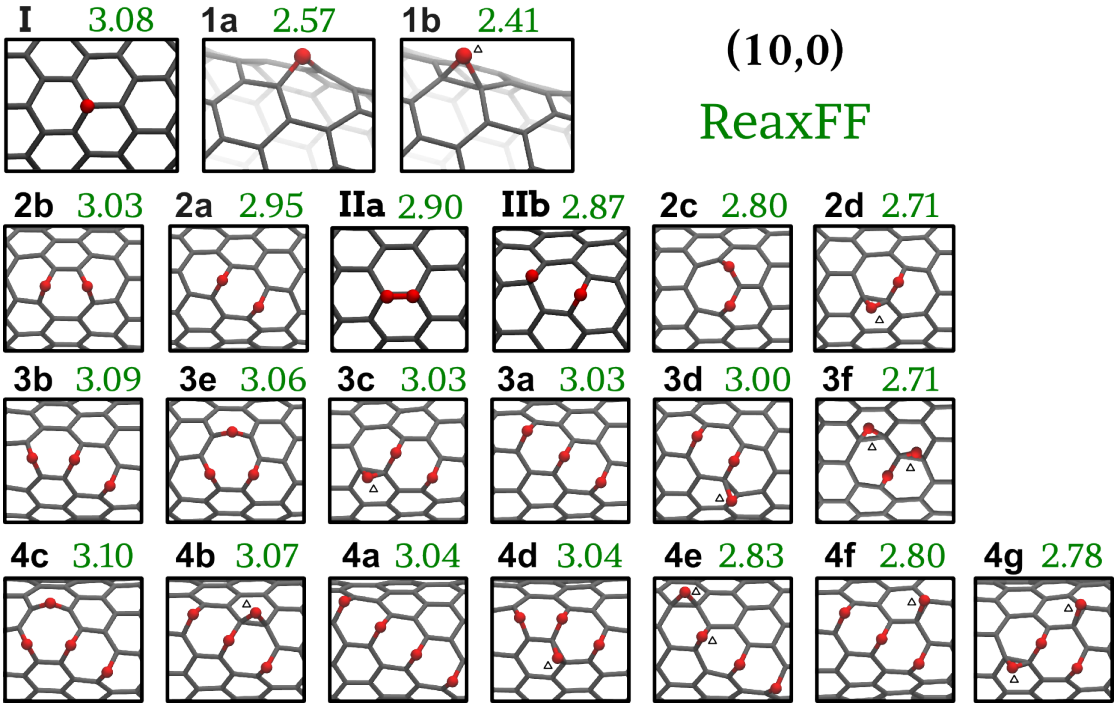

Figure 4.24: (10,0)-CNT:nO structures from ReaxFF. Notation as in Fig. 4.12 apart from Roman numerals that refer to cases with oxygen on on-top positions. Note: d(O-O)=1.25Åin (IIa). Note that E(O)=0 in this scheme.

configurations found stable with DFT-PBE, the agreement with the *ab initio* description is rather good. This can be argued from the plot of binding energies in Fig. B.5a and through comparison of Fig. 4.24 and Fig. 4.12. More precisely, ETs are predicted to be more stable than EPs and the relative ranking is similar although EPs are less disfavoured. Extensive details are given in Tables B.6, B.7, B.8 and B.9. We remark "spurious" values for the C-C distances (from 1.6 to 1.8 Å), which lie between those of an sp^2 C-C bond (like in the EP) and of an ET.

We also analysed the validity of the Θ_B and B.O. ReaxFF values (Tables B.11, B.12 and B.13) as chemical descriptors, and in particular whether the bare-bond curvature correlates well with the result of chemisorption (Fig.4.25(b)). We note that the B.O. values intrinsic to this scheme scale well with the Mayer B.O.s, as can be seen in Fig. B.5b. This correspondence allows one to classify final configurations with "spurious" distances as ETs. Moreover, calculations on coronene suggest not too different ranges for the EP-ET transition: 32.5° for Θ_B and between 1.270 and 1.265 for the B.O. However, a number of discrepancies can be recognised, and especially the lower performance of the bare-bond curvature and the frequent lack of consistency between the two descriptors also for the (n,0)-CNTs. Comparing hopping paths and barriers is meaningless because the TS configurations in DFT are minima of the potential energy surface of the ReaxFF potential. These can then act either as sink or intermediates also for transitions from EP.

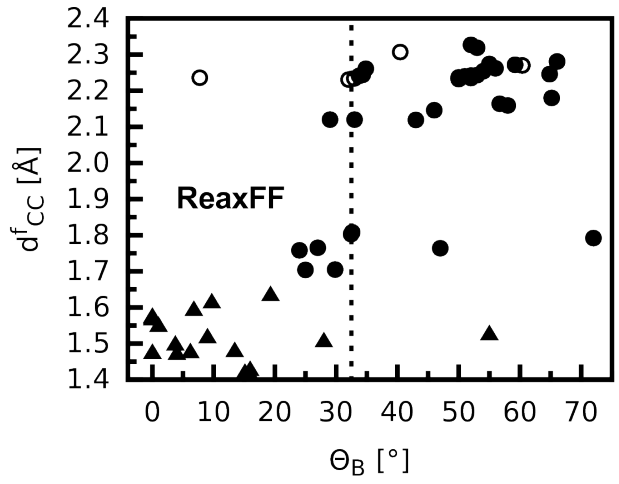

Figure 4.25: Same as Fig. 4.23 for ReaxFF.

4.2.8 CH_2, NH, SiH_2 and Sulphur Compared with Oxygen

Our results for O are compared to other species in Table 4.14. To avoid confusion with oxygen chemisorption we refer to the ETs and EPs as the open and 3-member rings in this section.

	B.L.(Z)	$E_B(Z)$	B.L.(A)	E_B(A)	Z-A	ΔE^*
O	2.082	2.66	1.489	2.25	0.41 [1.11]	0.8
NH	2.124	2.09	1.512	1.57	0.40/0.50[1] [1.28]	1.4
CH_2	2.113	2.93	1.539	2.44	0.49 [1.33]	1.9
SiH_2	1.666	0.62	1.557	0.52	0.10 [0.89]	0.4
S	1.561	1.22	1.498	1.32	-0.10 [-]	0.5

Table 4.14: (10,0)-CNT. Bond-length (B.L.) (in Å) of Z and A bonds after chemisorption and corresponding binding energy E_B (in eV), and energy barrier ΔE^* (in eV) for the hopping of a [2+1] adduct from the metastable to the ground state. Note that in all cases, but sulphur, Z corresponds to the ground state and A to the metastable state. Also the Z-A energy difference is reported explicitly to allow for comparison with previous calculations — in brackets — performed for the (8,0)-CNT (Ref. 160).
[1] The two values correspond to the two adjacent Z bonds that in this case are inequivalent

Chemisorption of one CH_2 or NH group on nanotubes has often been considered at the same time as oxygen (see Ref.s 160 and 145). We have considered both functional groups on the (10,0)-CNT and found that, as expected, the ET on the zigzag bond is strongly favoured over the EP on the axial bond as in the case of oxygen and also by a comparable amount (Δ(ET-EP) $\simeq$ 0.5 eV). Also the electronic structure close to the band-edges closely resembles the case of oxygen chemisorption. In particular, the EP introduces a midgap level a few tenths of an eV below the bottom of the conduction band of the pristine tube (at about 0.2 and 0.1 eV for CH_2 and NH respectively).

A more sizeable difference is found for the values of the binding energies and of the energy barriers for the hopping from the metastable EP to the ET state (Table 4.14). Previous calculations for the (8,0)-CNT, using relatively small hydrogen-terminated models, (see Ref. 160) predict values 2-3 times larger for Δ(ET-EP) for O, CH_2 and NH. Our value for the (8,0)-CNT is 0.4 eV as for the(10,0)-CNT (see Fig. 4.11(a)). Again we attribute this discrepancy to the slow convergence of the binding energy as a function of the model size.[28] However the trend is the same.

SiH_2 does not behave in a similar way as its counterpart methylene (Table 4.14): It still tends to preferentially sit on the zigzag bond and to stretch it but not as strongly as to break it, as can be argued from the ELF in Fig. 4.26. The more delocalized nature of the electron wavefunctions of the adduct strongly decreases the binding energy and makes it less sensitive to the C-C bond specificity (Δ(ET-EP) is only 0.1 eV to be compared to 0.9 eV in Ref. 160). This tendency is clearer in the case of sulphur (Table 4.14), which is bound to the nanotube in the form of an EP on both C-C bonds (Fig. 4.26). We also notice that sulphur has a larger binding energy on the axial bond. An increase of concentration confirms the fact that the thermodynamically favoured structures are EPs only (Fig. 4.27). Clear preference for clustering also emerges from Fig. 4.27, with alternating patterns on the A sites. Z-bonds are disfavoured for n>1 and can either be preserved or cleaved upon chemisorption, depending on concentration (see Fig. B.6). PBE0 calculations on the PBE geometries resulted in a decrease of the binding energies of $\sim$ 0.2 eV.

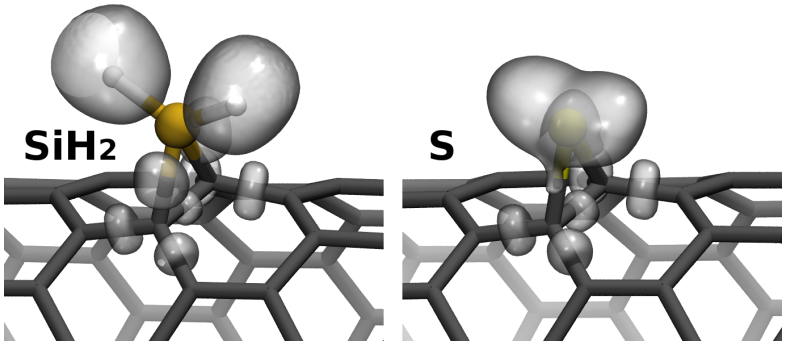

Figure 4.26: (10,0)-CNT:SiH_2/S. ELF (at isovalue 0.8) at the EP on the Z-bond.

Comparison with oxygen EPs shows that the bond-angle reduces from about 60° (61°-66°) by at least 10° (45°-49°)in the sulphur 3-member rings - an obvious size effect - whereas the pyramidalization angles of the carbon atoms are still about 10° and the deformation energy E_D is less than 1 eV (e.g., 0.8 eV in both S-1a and S-1b (Fig. 4.27) to be compared to 0.7 eV in 1b (Fig. 4.12). However, the binding energy is much weaker as found in previous model calculations[151,152] and in agreement with indications from experiment.[32] Details of these structures are reported in Table B.10.

From the above, it is clear that the idea that an adsorbate structure is determined only by the pristine CNT is no longer valid. This works as long as only first-row elements were involved in the bonding with carbon. If we want to use K_D or Θ_B or B.O. as predictors for S chemisorption

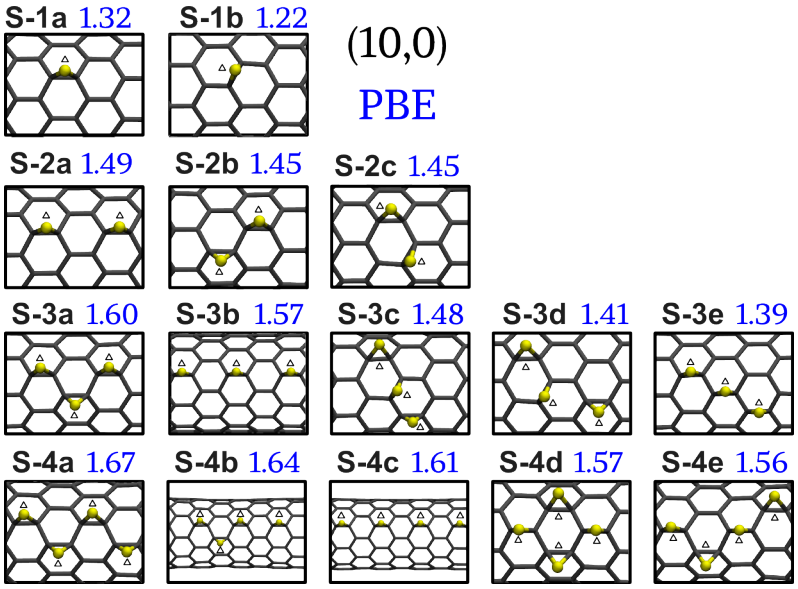

Figure 4.27: (10,0)-CNT:nS (n=1–4). Structures and binding energies E_B (in eV) referred to triplet sulphur. A small triangle indicates an EP.

products, their limiting values must be adjusted to the characteristics (e.g., size) of the head-atom. Calculations of S adsorbed on coronene would predict a less sharp correlation between Θ_B and the "final" C-C distance than the one observed for oxygen: 3-member rings are stable up to ∼60° whereas the open-ring configuration is stable from ∼69°. The critical B.O. range is instead limited between 1.13 and 1.15. Clearly, a much higher curvature (what we called "extreme" for the case of oxygen) and sizeably lower B.O. is necessary for bond cleavage to occur. The cases presented here for sulphur on nanotubes indicate that thioethers could form on bonds of high but somewhat smaller curvature ($\Theta_B \sim 55°$) than in coronene (see Table B.14).

Both SiH_2 and sulphur must overcome lower barriers than their counterparts to hop from one bond to the other (Table 4.14). The case of SiH_2 is more interesting because the molecule undergoes two transformations as illustrated in Fig. 4.28.

Both 3s- and 3p-levels of the sulphur atom resonate with the valence band of the nanotube and induce changes delocalized over several eV. In particular, a non-negligible mixing and a shift of the highest-occupied molecular orbitals of the nanotube is observed. The characteristic mid-gap level associated with the EP at the A-site appears also in this case (see Fig. 4.29). The increase in concentration adds other such levels and may tend to rapidly close the gap (see Fig. 4.30). We remark that these results were calculated with the PBE0 functional and that in PBE the gap would close already for the (10,0):4S CNT.

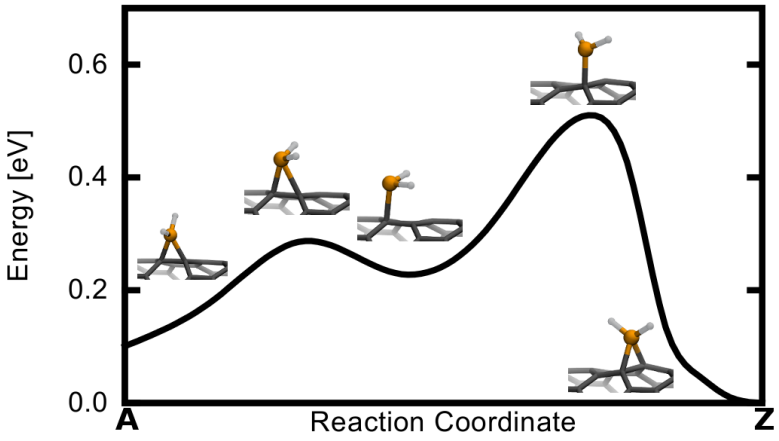

Figure 4.28: CNT:SiH_2. Energy profile and sketch of the relevant structure in the transformation between chemisorption on the A and Z bond.

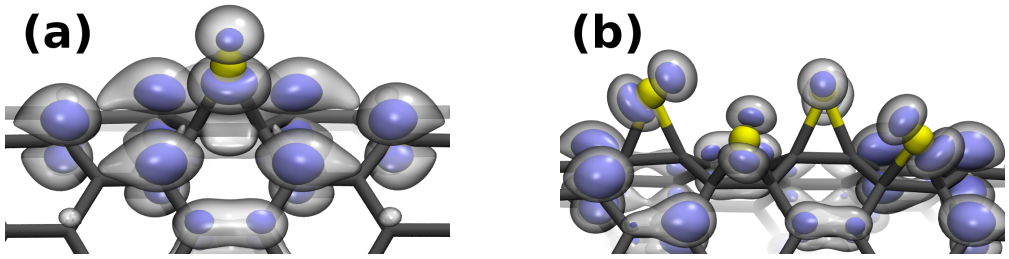

Figure 4.29: 10,0)-CNT:nS. Probability density corresponding to the LUMO in the (a) S-1a and (b) S-4a structures (see Fig. 4.27). Isosurfaces = 0.008, 0.002 $(au)^{-3}$.

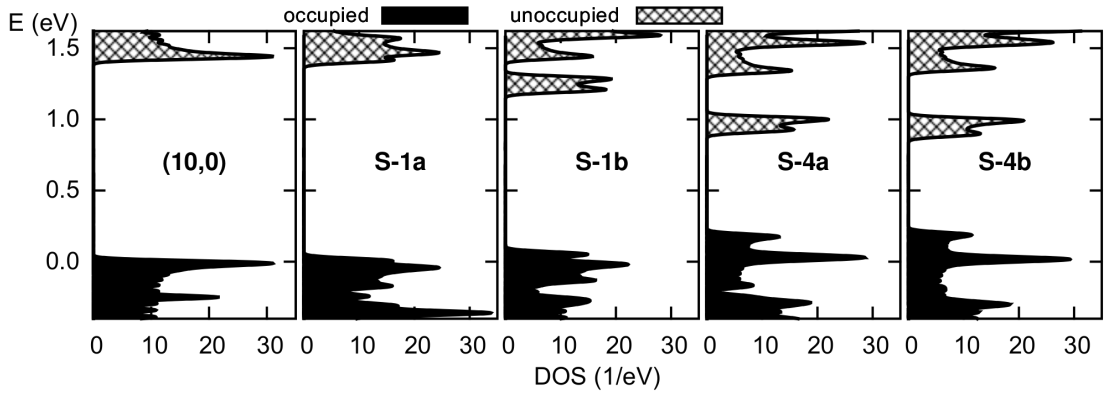

Figure 4.30: (10,0)-CNT:nS. Kohn-Sham DOS for n=1 and n=4.

4.2.9 Conclusions

We have shown that, with increasing concentration, oxygen atoms (Os) tend to cluster more and more, with ETs energetically preferred and thus an increasing structural deformation of the nanotube. Metastable EP configurations act as kinetic traps. They tend to avoid this deformation of the sidewall but generate ring strain (local loss of conjugation). Progressive changes of the neighbouring bonds induced by the presence of other chemisorbed oxygens do not allow to predict whether an additional oxygen will be chemisorbed in an ET or an EP on the basis of the characteristics of the pristine nanotube alone. An update of the bare-bond curvature, which accounts for the modifications induced by nearby chemisorption, still provides good predictions on possible bond cleavage, at least in the coverage-range considered here, unless other local modifications of the bond pattern take place.

Other moieties isoelectronic to O behave similarly if the head-atom belongs to the first row of the periodic table. On passing from oxygen to sulphur and from CH_2 to SiH_2, instead, the opening of the C-C bonds becomes improbable apart from cases of high curvature attained in chiral nanotubes of diameter less than 0.8nm. Given the preference for EPs, sulphur preserves the closed carbon rings but may induce sizeable changes in the electronic properties of the nanotube. In particular, by introducing the EP-characteristic levels in the gap, sulphur will tend to close it for lower concentrations than oxygen.

Comparison of the outcome of the reactive force-field ReaxFF and DFT-GGA shows similar results for the ET-EP competition but reveals that the most probable arrangement predicted by ReaxFF at low temperature consists of oxygen atoms in on-top sites and dispersed on the sidewall. On the contrary, on-top positions are unstable sites in the DFT-GGA and in the hybrid PBE0 functional frameworks. Therefore ReaxFF and DFT descriptions of the reaction dynamics are bound to be very different. The database resulting from our detailed comparison could be useful for an improvement of the classical potential.

Comparison with similar but partial calculations of a few oxygens on graphene models, still shows important differences between graphene and nanotubes of 1.3nm diameter. In particular, oxygen chemisorption does not seem to provide a way to unzip the sidewall of these SWNTs: EPs are effective traps for oxygen (hopping from an EP corresponds to high energy barriers) and ETs — especially clustered — are stable.

As a concluding remark, we note that, provided specific catalysts are devised, hopping of a divalent chemisorbed atom or functional group between an EP and an ET configuration could provide a mechanism for the control and tuning of bond-cleavage on the sidewall of a nanotube, in alternative to the on-site bond-switch induced by adduct rotation suggested in Ref.147,150,161 for adducts like dichlorocarbene.

5 Physisorption: The Case of Nitrogen-Oxides

In this chapter we apply different DFT functional schemes for the description of the adsorption of NO_x species, and also examine results obtained previously. Two main problems are approached: the difficulty of describing and quantitatively assessing the NO_x-CNT interaction and the identification of the species mainly responsible for the change of resistance (sensing response) measured on various nanotube settings.

5.1 Status of *Ab Initio* Calculations

A number of calculations have been published on the adsorption of NO_2 and NO_3 molecules on the sidewall of nanotubes. Table 5.1 reports the methods and the models used and Table 5.2 gives the results for the binding energy and the (minimum) distance from the tube. The tendency of LDA to bind NO_2 strongly is not surprising, and also the strong decrease in binding energy (0.03-0.04 eV) and larger distances (>3 Å) obtained within spin-polarised PBE. The only comparison possible of NO_2 and NO_3 is from Ref. 162 on the (8,0)-CNT, showing higher binding energy for the latter (by one order of magnitude) in spite of a large distance (>3 Å). This relatively large distance for the stable configuration of NO_3 is confirmed in Ref. 163 on the (13,0)-CNT. However no information is given for the binding energy. This is defined as the "physisorbed state". Indeed, in this same reference, another energy minimum is found — the "chemisorbed state" — which is 0.64 eV higher and corresponds to a shorter distance of 1.6 Å. In Ref. 162 also the co-adsorption NO and NO_3 was considered on the (8,0)-CNT. The pair was found to be stable at close distances ($\sim$ 1.5 Å) and have higher binding energies (up to 1.5 eV). These configurations were interpreted as chemisorbed states.

For comparison, in Table 5.2 we give the experimental values of the activation energies for desorption measured in different experiments. No calculations were made for desorption barriers.

Reference	Functional	Algorithm	CNT [N]
[164]	LDA	MT-PP[94]	(10,0) [40]
[165]	LDA[166]	AE-DND	(10,0) [80]
[41]	LDA[166]	MT-PP[94]-pw or AE-DND	(5,5) & (10,0) [40]; (17,0) [68]
[167][a]	LDA	AE-numerical basis	(10,0) [80]
[167][b]	LSDA	AE-numerical basis	(10,0) [80]
[167][c]	PBE[85]	AE-numerical basis	(10,0) [80]
[167][d]	SP-PBE[85]	AE-numerical basis	(10,0) [80]
[168][a]	LDA	MT-PP[94]	(10,0) [80]
[168][b]	LSDA	MT-PP[94]	(10,0) [80]
[162]	SP-PBE[85]	UPP[131]	(8,0) [64]
[163]	SP-PBE[85]	UPP[131]	(13,0) [103]

Table 5.1: Methods and models used in various referenced papers. All these calculations use PBC but with different unit cells. The number of atoms in the unit cell is give in parenthesis. Note: SP=spin-polarised; DND=double-numerical-depolarised basis functions; pw=plane-waves.

Ref.	C_h	E_B (eV)	c.t. (e^-)	d (Å)
		NO_2		
[162]	(8,0)	0.03	—	3.5
[41]	(5,5)	0.4	0.07	2.2
[41]	(17,0)	0.7	0.09	2.1
[41]	(10,0)	0.8	0.06	1.9
[164]	(10,0)	0.4	0.1	2.5
[165]	(10,0)	0.42	0.11	2.3
[168][a]	(10,0)	0.64	0.1	2.7
[168][b]	(10,0)	0.50	0.1	2.7
[167][a]	(10,0)	0.27	0.10	2.9
[167][b]	(10,0)	0.15	0.02	3.3
[167][c]	(10,0)	0.11	0.12	3.3
[167][d]	(10,0)	0.04	0.01	3.3
		NO_3		
[162]	(8,0)	0.5	—	3.3
[163]	(13,0)	—	0.4	3.1
[168][a]	(10,0)	1.37	—	2.87
[168][b]	(10,0)	1.17	0.14	2.87
experiment	material			E_{des} (eV)
[169]	graphite			0.4
[40]	s.c. SWNTs			0.4
[40]	metal SWNTs			0.2
[42]	CNT bundles			1.2
[38]	SWNT (D=1.5–2.5 nm)			1-1.1

Table 5.2: Binding energies (E_B), charge transfer (c.t.) and minimal distance from the tube (d). the tube chirality (C_h). For experimental results the desorption energy (E_{des}).

5.2 Our results

5.2.1 (10,0)-CNT : Description of the binding

We consider three molecules: NO_2, NO_3 and N_2O_4. Indeed the dimer — not treated earlier — is of interest because in the gas phase the monomer and the dimer are in equilibrium at room temperature.

We start by remarking that the description of the (isolated) dimer itself is non-trivial.[170] The thermodynamic ground state (at 0 K) of molecular NO_2 is in the form of a dimer with a relatively weak N-N covalent bond. Its formation is barrierless in all our calculations. However, the values of the binding energy are strongly dependent on the DFT-functional, as shown in Table 5.3. This table also shows a possible dependence on the atomic pseudopotential (which is BLYP, see Appendix C) for our B3LYP value and/or a basis-set effect. The CCSD(T) value of 0.73 eV[170] could be considered as reference. However the value reported in experimental papers for the dissociation energy of the dimer is 0.57 eV.[171]

PBE	PBE-D2	PBE0	BLYP	BLYP-D2	B3LYP	B3LYP[170]	CCSD(T)[170]
0.88	0.92	0.64	0.61	0.61	0.45	0.59	0.73

Table 5.3: Dimerization energy ($2E(NO_2) - E(N_2O_4)$ in eV) for the different functionals considered. Our results are further compared to calculations from Ref. 170.

We are particularly interested in testing the effect of Grimme's corrections to the gradient corrected functionals (PBE-D2 and BLYP-D2) and also of the inclusion of a fraction of exact exchange as in PBE0. As we have discussed earlier, previous calculations used LDA or PBE, namely xc-functionals that do not represent the long-range van der Waals like interactions and thus are unable to give physically reasonable results for "physisorbed states". Our results are summarized in Tables 5.4 and 5.5.

No appreciable structural change is found in either the molecule or the nanotube. Only PBE0 predicts a slightly different ground state structure for the isolated molecule NO_3 (Table 5.4.

The cases of NO_2 and N_2O_4 are similar and also the effect of the changes in the xc-functionals. The results are consistent with physisorption. This is confirmed by the absence of a chemical bond, as shown by the electron-localization-function (ELF) in Figure 5.1(a-b) and also the plot of the differential densities Figs. 5.1(d,e,g,h). Regarding the charge transfer, our estimate through the Mulliken population analysis, gives values even less than 0.1e. This localized weak charge transferred from the nanotube to the molecule is seen in the differential density (Figure 5.1 (d,e,g,h)). Grimme's empirical corrections strengthen the interactions — as expected — leading to an increase of the binding energy and a decrease the molecule-nanotube distance. The hybrid functionals have a different effect and a weak effect on the binding. This is also not surprising because the correlation part remains the same as in PBE/BLYP, in spite of the improvement of the long-range potential. BLYP does not bind N_2O_4.

	NO_2 (gas)			(10,0)-CNT:NO_2			
	d_{NO} (gas)	θ_{ONO} (gas)		d_{NO}	θ_{ONO}	d_{CN}	
PBE	1.21	134		1.21	131	3.05	
PBE-D2	1.21	134		1.21	132	2.87	
PBE0	1.19	135		1.19	135	3.22	
BLYP	1.22	134		1.23	129	3.40	
BLYP-D2	1.22	134		1.23	129	2.86	
	NO_3 (gas)			(10,0)-CNT:NO_3			
	d_{NO} (gas)	θ_{ONO} (gas)		d_{NO}	θ_{ONO}	d_{CN}	
PBE	1.25	120		1.26	120	3.28	
PBE-D2	1.25	120		1.26	120	3.08	
PBE0	1.20, 1.25	111, 125		1.24	120	3.12	
BLYP	1.26	120		1.27	120	3.45	
BLYP-D2	1.26	120		1.27	120	3.06	
	N_2O_4 (gas)			(10,0)-CNT:N_2O_4			
	d_{NO} (gas)	θ_{ONO} (gas)	d_{NN} (gas)	d_{NO}	θ_{ONO}	d_{CN}	d_{NN}
PBE	1.20	134	1.86	1.20	135	3.52	1.86
PBE-D2	1.20	135	1.87	1.20	135	3.14	1.86
PBE0	1.18	135	1.75	1.18	135	3.27	1.74
BLYP	1.21	134	1.92				
BLYP-D2	1.21	134	1.91	1.21	134	3.12	1.92

Table 5.4: NO_x structural characteristics in gas phase and on the (10,0)-CNT surface: bond lengths (in Å) and bond angles (in degrees) in the molecule and minimum distance (in Å) from the tube.

	PBE	PBE-D2	PBE0	BLYP	BLYP-D2
NO_2	0.05	0.17	0.04	0.06	0.19
N_2O_4	0.08	0.28	0.05	—	0.32
NO_3	0.63	0.80	0.44	0.69	0.94

Table 5.5: (10,0)-CNT: binding energies of different molecules obtained with different xc-functionals.

Measurements on graphite in Ref.169 reported an N_2O_4 structure perpendicular to the surface (O-down). We find that it is unstable and spontaneously transforming to the flat configuration.

In the case of NO_3 the estimated charge transfer is ∼0.4e (see Figure 5.1(f,i)). The calculated binding energies are clearly higher, which could erroneously be interpreted as a sign of chemisorption. Indeed the equilibrium minimum distance is still about 3 Åand the electron localization function (ELF) shows also in this case that no chemical bond forms (Fig. 5.1(c)) between the molecules and the CNT. This is again consistent with physisorption. The increase of the binding energy relative to the dioxide can be understood as due to the interaction of the localized charge with the delocalized, highly polarizable density of the π states on the tube surface. This is similar to what is found in the case of DNA on the CNT surface.[172]

Finally, for additional comparison with Ref.162 we considered the co-adsorption of the NO–

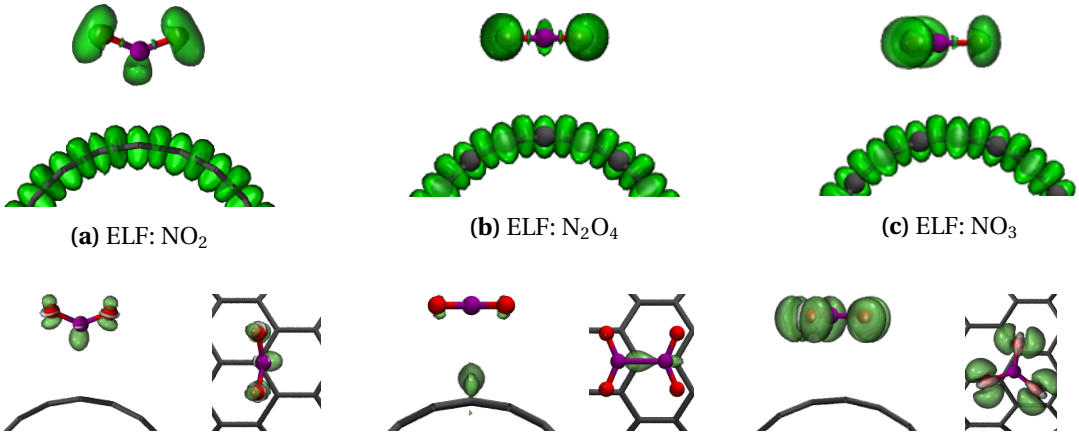

(a) ELF: NO_2 **(b)** ELF: N_2O_4 **(c)** ELF: NO_3

(d) $\Delta\rho$: NO_2 **(e)** NO_2 (top) **(f)** $\Delta\rho$: N_2O_4 **(g)** N_2O_4 (top) **(h)** $\Delta\rho$: NO_3 **(i)** NO_3 (top)

Figure 5.1: ELF ((a-c), isovalue 0.8) and differential charge ($\Delta\rho$) side- and top views (d-i) for the different considered nitrogen oxides on the (10,0)-CNT. For $\Delta\rho$, the green (white) shows a positive (negative) differential charge, i.e. donating electrons to (from) this position.

NO_3 pair configuration on the (8,0)-CNT and also on the (10,0)-CNT. By using the same unit cell as in Ref. 162 for the (8,0)-CNT we also find it stable and at smaller distances. However by increasing the cell size it becomes unstable. The same is true on the (10,0)-CNT. Therefore, the enhancement of binding with co-adsorption was only an artifact of the 64 atom-model for the unit cell. This is clearly inadequate to represent these adsorbates at very low concentration.

It is clear that more advanced quantum chemical methods are necessary to treat the problem of NO_x and any other physisorbed species on nanotubes. Unfortunately, more sophisticated calculations — MP2 [173] and quantum Monte Carlo [174] — have so far been possible only on very small fragments.

5.2.2 Indications from KS and Vibrational Spectra

In Fig. 5.2 the Kohn–Sham spectra calculated with the PBE-D2 functional at the Γ point of our supercell. In all cases considered, new levels appear in the gap of the pristine CNT. The orbitals (shown in the insets) are linear combinations of the NO_x molecular orbitals with CNT orbitals. These results hint at the possibility that some signatures of the different molecules could be found with electronic excitation spectra.

More direct information can be found in the vibrational spectra, for which experiments are available [42] reporting on infrared spectra of CNTs recorded after exposure to NO_2 gas. The data for the frequencies in Table 5.6 shows a remarkable difference with the isolated molecule, which cannot be understood on the basis of the knowledge of a weak NO_2-CNT interaction inducing no special deformation. In Ref. 42 the data were thus explained as due to the formation of a *nitrito* configuration in which the NO_2 molecule sits inside the CNT bundle with the two oxygen atoms bound to different CNTs.

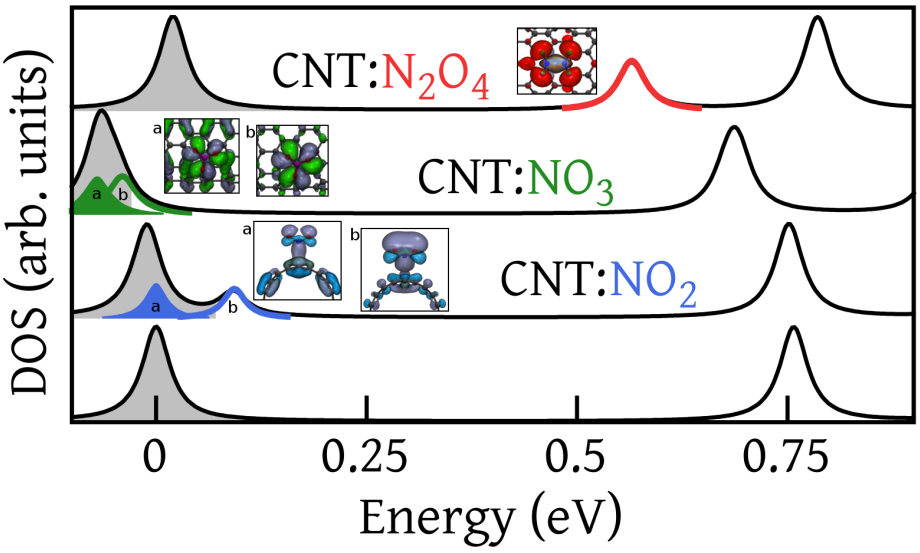

Figure 5.2: (10,0)-CNT: NO_x Kohn-Sham (KS) density of states (DOS) for the different molecules considered. Occupied (filled curves) and unoccupied (open curves) impurity states are shown as inset.

	theory					
NO2 (gas)	*741*	*1320*	*1608*			
NO2 (CNT)	669	1216	1567			
NO3 (gas)	471 (2)	767	1076	1195 (2)		
NO3 (CNT)	614 (2)	**783**	**1042**	**1243** (2)		
$NO3^-$ (gas)	689 (2)	803	1023	1310 (2)		
N_2O_4 (gas)	90	245	296	393	467	633
	734	822	1254	1394	1718	1746
N_2O_4 (CNT)	141	200	262	401	452	615
	723	816	1245	1375	1712	1735
	experiment					
NO_x (CNT, exp.[42])	**808**	**1026**	**1302**			
NO_2 (gas, exp.[175])	*750*	*1325*	*1612*			
NO_2 (gas[176])	*750*	*1319*	*1617*			
N_2O_4 (gas[177])	752	1274	1754			
N_2O_4 (gas[178])	750	1261	1748			
N_2O_4 (gas[169])	270	430	740–760	1270–1280	1760–1770	
N_2O_4 (graphite[169])	290	450	780	1290	1770	

Table 5.6: Calculated fundamental frequencies (in cm^{-1}) of the different molecules in gas–phase and on the (10,0)-CNT (PBE-D2). (2) indicates double degeneracy. Experimental values from different sources are given for reference.

We computed the vibrational frequencies of the three different molecules considered in the linear response scheme,[179] both in gas phase as well as on the (10,0)-CNT surface (see Appendix C). Comparison in Table 5.6 with experimental data is self-explanatory. In particular, for the gas-phase NO_2 the agreement is excellent. Changes due to the adsorption are not negligible but not such as to explain the observations. A simpler explanation can however be suggested, namely that the species detected with IR after adsorption of NO_2 is indeed NO_3. The presence of a localized fractional charge on the physisorbed NO_3 explains the difference, as shown by comparison with NO_3^-. Weak effects are found for the dimer, in agreement with experimental data on graphite.

5.2.3 Dependence on Diameter

For NO_2 and NO_3 the dependence of the binding energy dependence on zigzag CNT diameter is shown in Fig. 5.3. The results from two computational models are shown: (i) for the 360 C atom periodically repeated model with Γ-point only and (ii) using a 80 C model with k-points. Details on the methods are given in Appendix C.

We remark that, contrary to the case of oxygen chemisorption, the binding energy increases with increasing diameter for both molecules for semiconducting nanotubes. The effect is sizeable and the relative change from one case to the other is essentially the same for NO_2 and NO_3. This behavior is consistent with the increase of polarization of the CNT electron states with decreasing gap (increasing diameter). For metallic nanotubes, the binding energy is indeed higher, in agreement also with experimental data[40] and no appreciable variation with diameter is found.

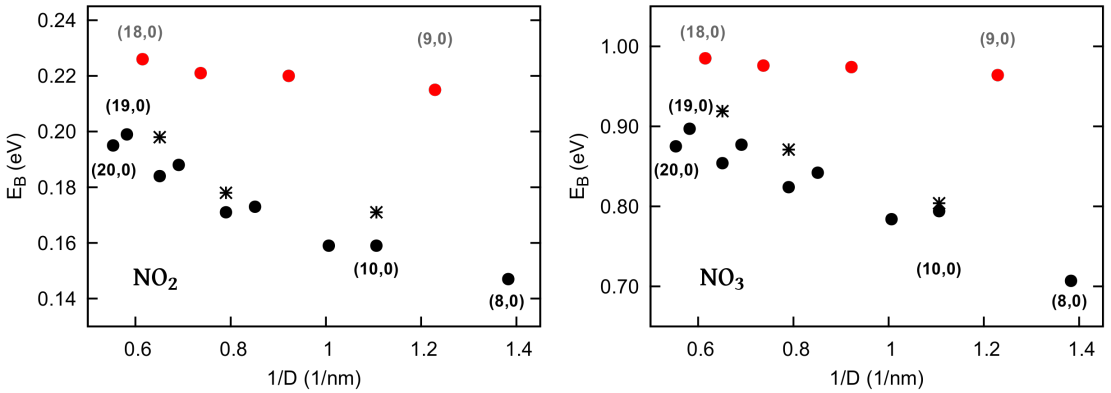

Figure 5.3: PBE-D2: (n,0)-CNT with NO_2 (left) and NO_3 (right). The dependence of the binding energy on the diameter for zigzag-nanotubes. Stars (circles) are used for computational model i (ii).

6 Intrinsic Defects: Single and Double Vacancies on the (10,0)-CNT

Vacancies are not expected to form at high concentration during synthesis of carbon nanotubes which takes place at temperatures of the order of 3000 °C. Still, as for any other defect, their presence is supposed to strongly influence the physical behavior of a nanotube, in particular when combined with interstitials or adatoms. The role of vacancies is also often invoked to explain unexpected strong effects, e.g. in the binding of molecules like NO_2 [180] or to characterize oxidation processes. [181] Therefore modelling of realistic systems cannot ignore their presence.

Systematic studies have required artificial generation of vacancies from irradiation with high-energy electrons or ions. [50] Their characterization is not immediate however. Our understanding relies on a thorough theoretical investigation. In particular, STM/STS experiments and DFT-GGA calculations of the local-density of electron states of single and double vacancy configurations, also coupled with interstitials and Stone-Wales defects.

Our primary aim is twofold: (i) comparing the predictions of commonly used carbon force-fields to those of DFT calculations, and (ii) within DFT investigate the dependence of the results on the xc functional. In particular, for the latter, we are interested in identifying the changes induced by introducing partial effects of the exact exchange on passing from PBE to PBE0. The physical quantities we consider are formation energies, structural characteristics, reconstruction and migration barriers. As working example, we consider the (10,0) nanotube. This choice allows us also comparison with previous calculations. Our results refer to Ref. 182.

6.1 Our Results and Comparison with Previous DFT Calculations

No systematic work on vacancies on nanotubes exists. However, several DFT-based calculations have been published aimed at establishing the thermodynamically favoured configurations of vacancies formed by the loss of few atoms and their formation energies, [183–188] how they modify the characteristics of the pristine nanotube [29,167,189] and also how their presence might manifest itself, e.g. in Raman spectra. [47] In the following we will mention some of these calculations for comparison with our results. In particular, the selected calculations use peri-

Reference	Functional	Algorithm	Size (N)
[183]	PW[84]	PAW[190]	120
[185][a]	PBE[85]	MT-PP[94]-DZ	120
[185][b]	PBE[85]	MT-PP[94]-DZ	240
[186][a]	PW[84]	PAW[190]	120
[186][b]	PW[84]	TB	120
[191]	PW[84]	UPP[131]	120

Table 6.1: Methods used in various referenced works.

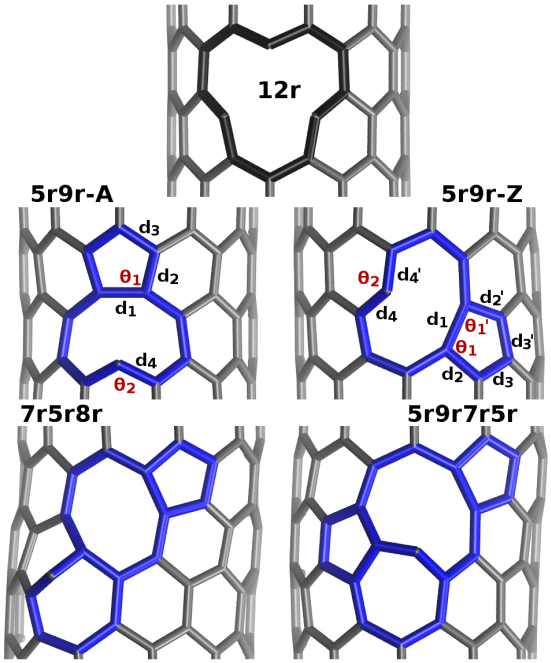

Figure 6.1: Single vacancy structures

odic boundary conditions and GGA functionals. The details in Table 6.1 help understanding possible differences in the results reported below.

We have considered a few single- and double vacancy configurations, which are shown in Figure 6.1 and 6.2 respectively. In order to explore a larger set of geometries than those sporadically considered in the literature, the starting step of our investigation consisted in classical MD simulations (using AIREBO) of a large-size model for the nanotube (10,000 atoms) in a range of temperatures (300 – 2500 K). We considered the configurations with higher population and optimised their structure *ab initio*. Eventually, however, only a few could be classified as local minima of either the DFT-PBE or the DFT-BLYP potential energy surface (see Figures 6.1 and 6.2). Geometries denoted as 12r and 14r are plotted as reference, and represent the holes left by stripping one or two atoms, with three or four dangling bonds (DBs). These are unstable in our calculations, as will be discussed below, but are metastable states in most of the other approaches we considered.

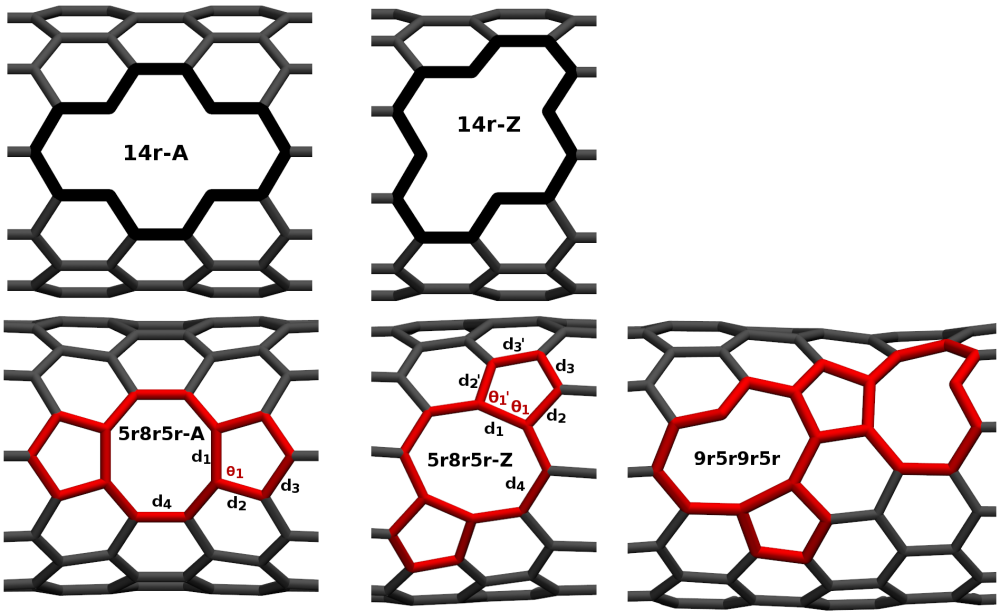

Figure 6.2: Double vacancy structures

The vacancy formation energy ϵ_f is defined as

$$\epsilon_f = (E_{\text{vac}} - n\mu - E_0)/n,$$

where E_{vac} and E_0 are the total energies of the defective and pristine nanotubes respectively and μ is chemical potential of carbon, which should be referred to its most stable structure. In general, however, this value is approximated as the energy per atom in the pristine nanotube: $\mu = E_0/N$. In the Tables below, we will report the values $E_f = n\epsilon_f$.

In analogy to the case of oxygen chemisorption, we find — as shown in Figure 6.3 — that in some cases smaller-size CNT-models can be used for the calculation of vacancy formation energies, but also that in others (see double vacancy 5r8r5r-Z) convergence of E_f is attained very slowly (600 atoms). This behavior depends on whether the perturbation induced by atom loss is more or less localized, as shown in the plot of the structural changes (strain distribution) (Figure 6.4). Apart from the case of the double vacancy 5r8r5r-Z for which we refer to the PBC-600-atom model, the results refer to calculations with the 360-atom unit cell.

As shown in Table 6.2(A), PBE and BLYP functionals are in close agreement regarding the values the formation energies and in most cases, BLYP tends to reduce them. Adding part of the exact exchange as in the PBE0 functional increases the formation energies significantly but preserved the ranking. The same conclusion can be derived from the energy gain in Table 6.3. On the other hand, we have also verified that including Grimme's corrections[89] for van-der-Waals interactions has no appreciable effect. In Table 6.4 comparison is made with previous GGA calculations is clarified. Ref. 183 apparently found the 12r geometry to correspond to a local energy minimum, in analogy with other LDA computations.[184] The progress of one of our geometry optimizations — leading to the 5r9r-Z — is illustrated in Figure 6.5. The plateau

(A) XC-funct.	12r	5r9r-A	5r9r-Z	5r5r	5r9r7r5r	7r5r8r
PBE	⋆	5.54	6.51	⋆	7.89	9.49
BLYP	⋆	5.47	6.26	⋆	7.50	9.13
PBE0	⋆	6.01	7.27	⋆	—	—
	14r–A	14r–Z	5r8r5r-A	5r8r5r-Z	9r5r9r5r	
PBE	⋆	⋆	3.92	4.98	11.96	
BLYP	⋆	⋆	3.97	4.77	11.61	
PBE0	⋆	⋆	4.28	5.96	13.60	
(B) Force-field	12r	5r9r-A	5r9r-Z	5r5r	5r9r7r5r	7r5r8r
ReaxFF	8.04	5.44	7.17	6.09	8.40	8.91
AIREBO	6.71	4.87	5.94	4.81	7.57	7.43
REBO	8.04	5.70	6.72	4.45	8.32	8.78
LCBOPI	7.11	4.62	5.80	5.70	7.14	7.33
LCBOPII	7.17	5.16	6.18	4.81	7.21	8.27
	14r–A	14r–Z	5r8r5r-A	5r8r5r-Z	9r5r9r5r	
ReaxFF	9.96	10.61	3.31	6.08	12.22	
AIREBO	8.90	9.08	4.26	6.31	10.49	
REBO	10.55	10.80	4.78	6.46	12.28	
LCBOPI	9.24	9.49	3.22	5.42	10.19	
LCBOPII	9.45	9.47	3.92	5.38	11.25	

Table 6.2: Vacancy formation energies (⋆ = unstable) E_f in eV.

(A) XC-functional	12r	5r9r-A	5r9r-Z	5r5r	14r–A	14r–Z	5r8r5r-A	5r8r5r-Z
PBE	⋆	2.32	1.36	⋆	⋆	⋆	5.59	4.59
BLYP	⋆	2.08	1.29	⋆	⋆	⋆	5.09	4.32
PBE0	⋆	2.62	1.40	⋆	⋆	⋆	6.09	4.41
(B) Force-field	12r	5r9r-A	5r9r-Z	5r5r	14r–A	14r–Z	5r8r5r-A	5r8r5r-Z
ReaxFF	3.34	5.94	4.21	5.30	4.46	4.16	11.11	8.96
AIREBO	0.91	2.75	1.69	3.17	1.28	1.11	5.92	3.87
REBO	0.65	2.98	1.96	4.07	0.99	0.79	6.76	5.13
LCBOPI	0.91	3.39	2.21	2.31	1.20	0.90	7.22	4.97
LCBOPII	0.83	2.84	1.82	3.19	0.94	0.85	6.47	4.93

Table 6.3: Energy gain corresponding to metastable and stable structures, relative to the pristine nanotube. 12r and 14r are optimised structures for the classical potential schemes (⋆ = unstable).

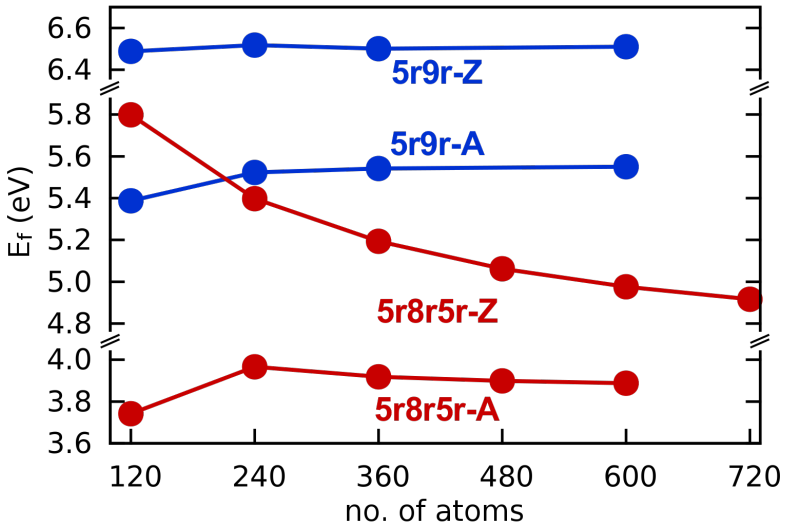

Figure 6.3: Formation energies for different sizes of the periodically repeated unit cell.

XC-functional	5r9r-A	5r9r-Z	12r	5r8r5r-A	5r8r5r-Z
PBE (this work)	5.54	6.51	$\star$	3.92	4.98
BLYP (this work)	5.47	6.26	$\star$	3.97	4.77
PBE0 (this work)	6.01	6.83	$\star$	4.29	5.96
PW[183]	5.5	6.7	7.4	–	–
PBE[185a]	5.67	7.11	–	3.90	6.65
PBE[185b]	5.65	–	–	4.06	–
PW[186a]	5.6	–	–	3.5	–
PW[186b]	6.4	–	–	4.2	–
PBE[191]		–	–	3.61	6.07

Table 6.4: (10,0)-CNT: Comparison of several DFT-based calculations of vacancy formation energies E_f in eV ($\star$ = unstable).

corresponds to the 12r geometry after mere relaxation from the pristine structure with one vacancy, which amounts to a gain of ∼0.5 eV. Apart from this case, there is a global consistency among all these calculations.

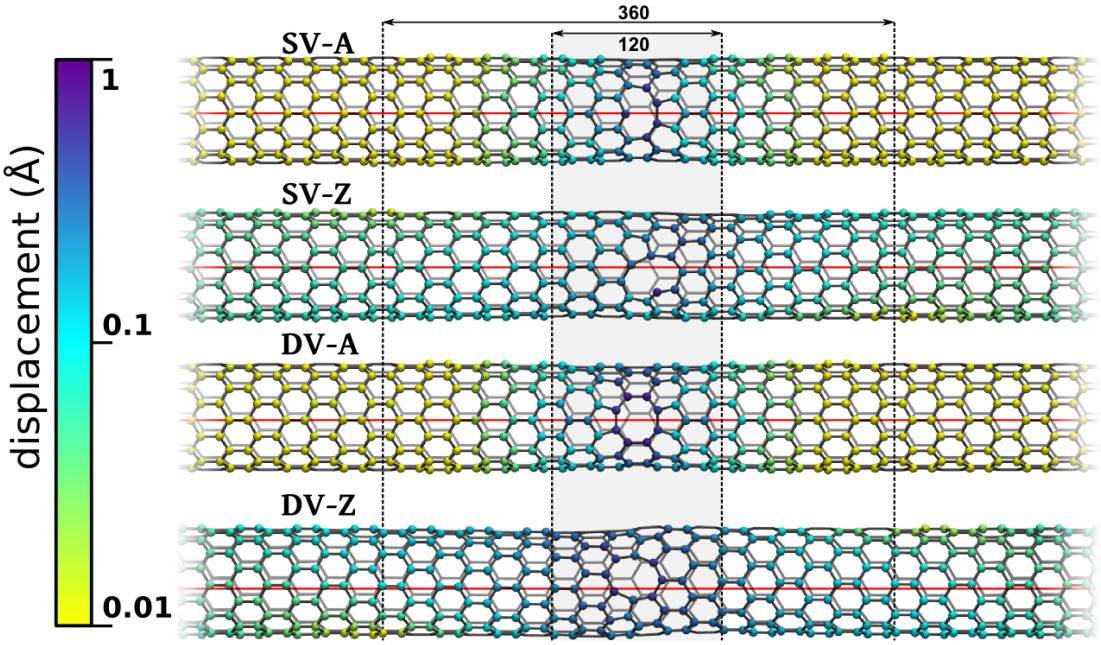

Figure 6.4: Displacements (in Å) of the carbon positions induced by the most stable single and double vacancies. The employed cell size contains to 600 C atoms. Smaller cells are indicated for illustration. The red line serves as a guide-to-the-eye for the lattice mismatch in smaller smells.

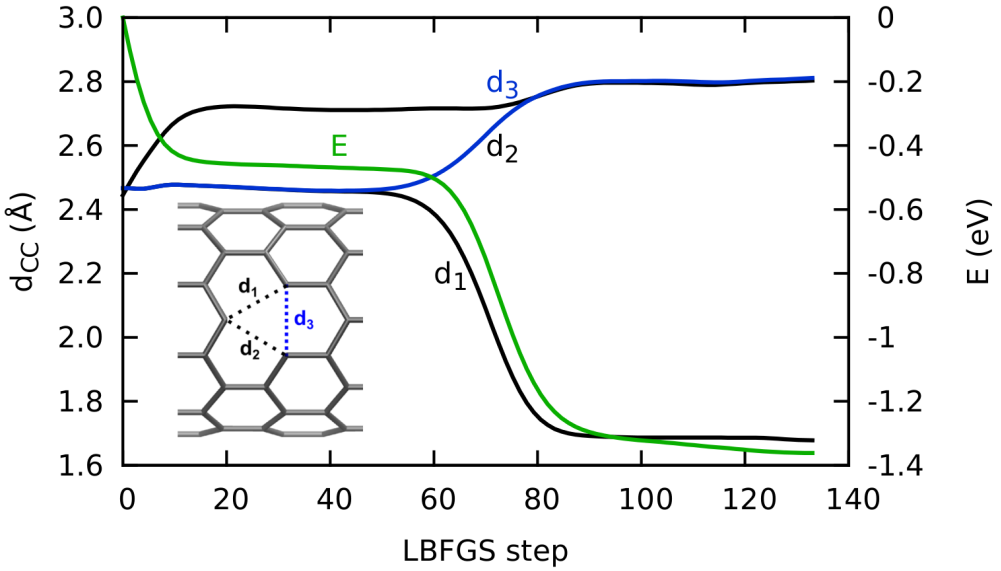

Figure 6.5: Geometry optimization starting from the pristine nanotube after loss of one atom.

5r9r-A	d_1	d_2	d_3	θ_1	d_4	θ_4
PBE	1.54	1.44	1.41	105	1.39	116
ReaxFF	1.45	1.46	1.47	107	1.37	149
AIREBO	1.47	1.46	1.42	107	1.41	117
5r9r-Z	d_1	d_2 ; d_2'	d_3; d_3'	θ_1 ; θ_1'	d_4; d_4'	θ_4
PBE	1.68	1.45; 1.43	1.41; 1.40	104; 100	1.37; 1.36	124
ReaxFF	1.50	1.45; 1.45	1.46; 1.46	109; 100	1.36; 1.36	141
AIREBO	1.66	1.46; 1.48	1.40; 1.39	105; 98	1.40; 1.40	117

Table 6.5: Single vacancy configurations. Bond distances (d) are in Å, angles in degrees.

5r8r5r-A	d_1	d_2	d_3	θ_1	d_4
PBE	1.50	1.42	1.42	106	1.46
ReaxFF	1.44	1.46	1.47	108	1.42
AIREBO	1.44	1.45	1.42	107	1.40
5r8r5r-Z	d_1	d_2; d_2'	d_3 ; d_3'	θ_1; θ_1'	d_4
PBE	1.58	1.44; 1.43	1.41; 1.40	106; 102	1.48
ReaxFF	1.48	1.46; 1.45	1.47; 1.45	108; 102	1.45
AIREBO	1.55	1.46; 1.47	1.41; 1.40	106; 102	1.43

Table 6.6: Double vacancy configurations. Geometric characteristics as in Table 6.5.

6.2 Results using Classical Force-fields

Comparison of force-fields and DFT predictions for defective structures of graphitic surfaces is essentially missing in the literature, apart from some regarding the REBO potentials in Ref.s 192 and187. This same potential was used to study the effect of vacancies on the mechanical properties of CNTs. [193]

Here we make a first attempt toward a systematic comparison. First, we compare geometrical characteristics for the relevant structures found in the DFT schemes with the most commonly used potentials. In this respect, AIREBO gives results close to PBE, whereas significant discrepancies are found for the single vacancy in ReaxFF.

Formation energies are given in Table 6.2. Here one can see remarkable differences, especially for most potentials of the REBO-family, that — as already pointed out in Ref.187 — predict an unexpected configuration (5r5r in Figure 6.6) as the lowest one of all those considered. It is a local minimum of the potential energy surface in the other force fields and unstable in our DFT calculations.

However, an ever more serious concern regards the kinetics. As clarified above, in our *ab initio* calculations the 12r and 14r structures spontaneously reconstruct. On the contrary, in all the classical potential schemes we have considered these reconstructions requires a complicated path (in two-steps for the double vacancy) and a high energy barrier, as shown in Table 6.7. This is the primary bottleneck one encounters when attempting to use these force-fields.

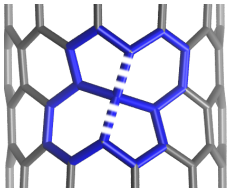

Figure 6.6: Lowest-energy structure in REBO, AIREBO and LCBOPII schemes.

Force-field	R(5r9r-A)	R(5r9r-Z)	R(5r8r5r-A)	R(5r8r5r-Z)
ReaxFF	2.96	2.76	2.58 ; 1.71	2.86 ; 2.37
AIREBO	1.08	1.32	1.37 ; 0.61	1.01 ; 0.79
REBO	0.97	1.23	1.24 ; 0.41	0.88 ; 0.37
LCBOPI	1.34	1.02	1.11 ; 0.11	0.88 ; 0.71

Table 6.7: Force-field: Energy barriers (in eV) for defect reconstruction on the (10,0)-CNT. The double vacancy reconstruction consists of two successive steps, each corresponding to the formation of one bond. In our DFT calculations, these reconstructions are barrierless.

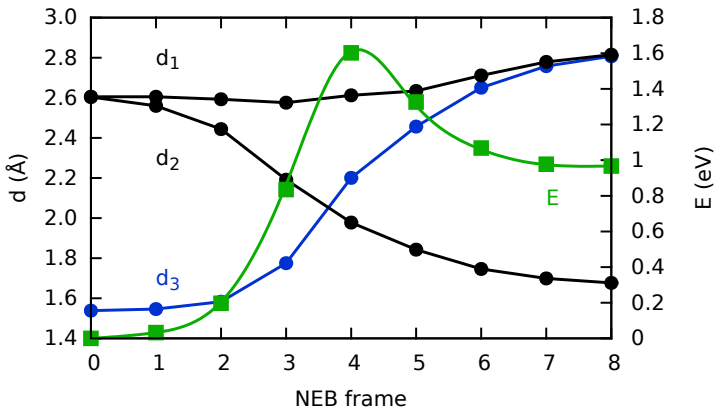

Figure 6.7: Distance variation along the transformation from the 5r9r-Z to the 5r9r-A structure (see Figure 6.1).

PBE	0.65
PBE0	0.68
PW [186]	0.45
ReaxFF	1.21 ; 0.64
AIREBO	1.85
REBO	2.60
LCBOPI	2.29

Table 6.8: Energy barrier (in eV) for single vacancy migration from the 5r9r-Z to the 5r9r-A structure.

As shown in Figure 6.8, in the ReaxFF approach, the migration of the single vacancy is also more complicated than in DFT-PBE and all other potentials considered here: For the latter, the transition involves one single step whereas it is a two-step process in ReaxFF potential implying as intermediate state the 5r5r configuration (Figure 6.6).

6.3 Elastic Properties: Young's modulus

To make a further comparison between classical potentials and DFT-PBE, the effect of vacancies on the Young's modulus is estimated in several schemes, using the same CNT models, namely a supercell comprising nine unit cells. This model represents the case of isolated (non-interacting) vacancies. Only the ground states are considered for both SV and DV. The length L optimised in the pristine nanotube is kept. The Young's modulus under uniaxial

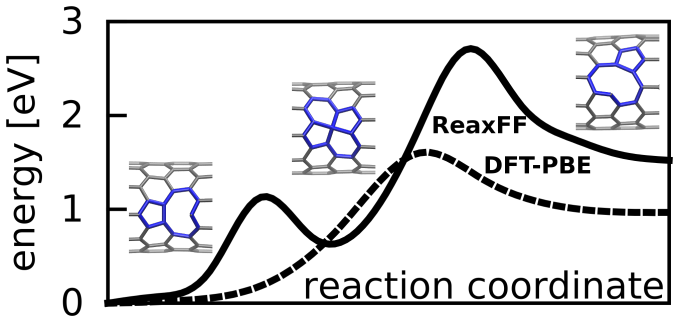

Figure 6.8: Single vacancy migration for DFT-PBE and ReaxFF.

	PBE	LCBOPI	LCBOPII	AIREBO	REBO	ReaxFF
L (Å)	4.267	4.246	4.228	4.183	4.194	4.318
a^1_{CC} (Å)	1.421	1.421	1.425	1.401	1.401	1.435
a^2_{CC} (Å)	1.428	1.425	1.427	1.405	1.406	1.454
Y_0 (GPa)	983	931	1004	988	1014	920
Y_{SV} (GPa)	947	917	990	964	990	892
ΔY_{SV} (%)	3.6	1.6	1.3	2.5	2.3	3.1
Y_{DV}-A (GPa)	966	905	963	958	988	897
ΔY_{DV}-A (%)	1.7	2.8	4.1	3.1	2.6	2.6
Y_{DV}-Z (GPa)	935	886	963	943	977	900
ΔY_{DV}-Z (%)	4.9	4.8	4.0	4.6	3.6	2.2

Table 6.9: Young's modulus Y of the defective (10,0)-CNT and reduction relative to the pristine CNT (ΔY) obtained in DFT-PBE and several reactive force-fields. Also given are the values of the supercell length (L) and of the bond lengths (d_{CC}) in the pristine nanotube.

strain is calculated from the harmonic approximation

$$E(\epsilon) = E_0 + \frac{1}{2} Y\ L\ A \epsilon^2,$$

where $A = 2\pi r t$ is the effective CNT surface area (r=4.07 Å and t=3.35 Å). Because the absolute value depends on the precise definition of the CNT surface area, the relative changes due to the presence of vacancies are also given. As a single quantity representing a global characteristic of the system, Y is less sensitive to the local rearrangement of the carbon bonds. Therefore, the agreement between different schemes for the prediction of the modifications induced by 1-2 atoms loss is in general better than what we discussed above.

6.4 Conclusions

The study presented in this chapter clearly shows that the most widely used classical potentials for carbon aggregates, from graphite to fullerenes to nanotubes to graphene, have difficulties to represent defective nanotube structures with simple vacancies. This is especially true because, contrary also to intuition, unreconstructed structures — with dangling bonds — are metastable states separated by high-energy barriers from the low-energy geometries.

7 Top-down CNT formation from Graphene Nanoflakes

This chapter reports on on-going work aimed at gaining more insight into the mechanisms leading to folding of graphene into nanotubes. The calculations presented here refer to a model of 142 carbon atoms, initially arranged in a (nano)flake and eventually folded into a tubular structure. The main results we can achieve with this model are: (i) comparison of different metadynamics strategies, namely employing either path [122]- or SPRINT [123]- CVs (see Chapter 3); and (ii) within path metadynamics, comparison of the predictions obtained from calculations based on DFT-PBE (with and without Grimme's corrections [89]) and the LCBOPII [111] force-field that includes van-der-Waals interactions (see Chapter 3).

7.1 Previous related calculations

No simulation of the folding of a graphene flake or a GNR into a nanotube caused by thermal activation only has ever been attempted. However, it is worth mentioning here two computational approaches to GNR–nanotube transformations which were related to experiments mentioned in Chapter 2. In Ref.s 66,69 classical MD using the Brenner potential [194] and a simple reaction coordinate (distance between the edges of the CNT) were applied to simulate the unzipping of a (8,8)-CNT at 600K to a GNR. In the absence of the template molecule, this process found to have a barrier of about 5 eV. In Ref. 68. Folding through twisting was studied for several cases with DFT-TB based MD at room temperature. A barrier of the order of 1.5 eV/Å was calculated for a 2.4nm-wide GNR (similar to our 238-atom flake model) transforming to a (9,3) nanotube.

7.2 Our results

Molecular dynamics simulations were performed at 1000 K. This choice is consistent with typical CVD temperatures and also with previous studies using SPRINT-CVs metadynamics [63] that succeeded to obtain the folding of a nanoflake into a fullerene-like cage. Computational details are given in Appendix C.

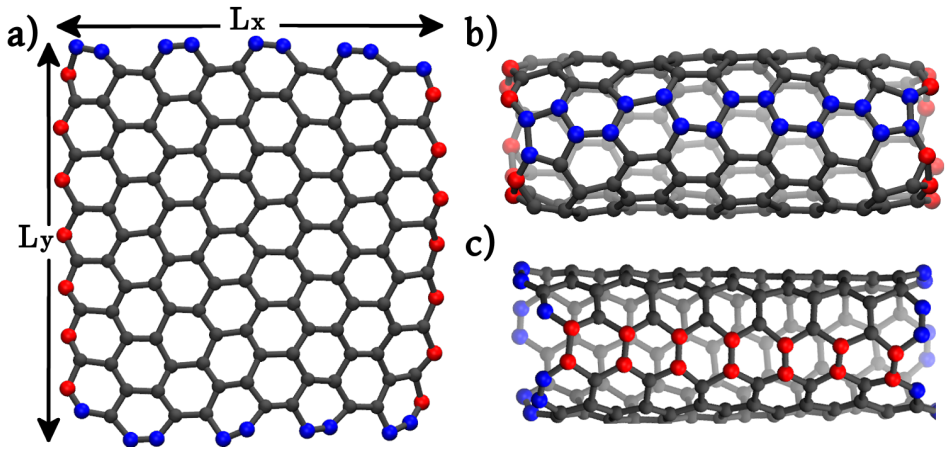

Figure 7.1: Structures of (a) the 142-atom nanoflake, (b) zigzag- and (c) armchair- folded configurations. L_x=17.9 Å, and L_y=18.9 Å for the 142 C nanoflake.

Method	E_{flake}	$E_{Z\star}$	E_Z	E_A
PBE	0	-48	-85[-117]	-91[-80]
PBE-D2	0	-59	-98[-125]	-102[-89]
LCBOPII	0	-35	-93[-95]	-53[-101]

Table 7.1: Energies (in meV/atom) of the (optimised) structures in Fig. 7.1. In parenthesis we report the values obtained starting from the 238 C nanoflake.

The nanoflake model is depicted in Fig. 7.1(a). Two orthogonal folding edges can be identified: the armchair edge leading to a zigzag-CNT (Z) (Fig. 7.1(b)) and the zigzag edge leading to an armchair-CNT (A) (Fig. 7.1(c)). The tubular structures obtained from the 142 C flake have (8,0) and (4,4) chiralities, whereas those generated from the 238 C flake correspond to (10,0) and (5,5) chiralities.

The energy gain associated with folding is given in Table 7.1 for both cases. Energies are reported per atom so as to better compare also with our calculations using a larger model with 238 atoms. In the case of the Z-CNT, an intermediate structure (Z*) is found in which only 2-fold coordinated atoms exists at the termination. Further bond formation (closure to pentagons) leads to the metastable zigzag conformation.

In all calculations, folding corresponds to an important energy gain. As expected, Grimme's correction for dispersion energy further lowers the energy of the folded structures (by ∼1.5-2 eV). This does not change the ranking of A and Z. Comparison with LCBOPII appears to be size-dependent but in both cases the relative stability of the two tubular structures is inverted with respect to DFT-PBE and DFT-PBE-D2.

Using path–metadynamics, we determined how the folding takes place and estimated the free energy barrier ΔF^*, in both directions (see Table 7.2. A few snapshots along the pathway are shown in Fig. 7.2 and Fig. 7.3, where (a) and (a') indicate "incipient" edge-driven folding.

Method	ΔF_Z^*	ΔF_A^*
PBE-D2	5	17
LCBOPII	36	41

Table 7.2: Free energy barriers (in eV) for the folding of the 142 C flake into the Z and A tubular structures, as estimated from path-metadynamics

Neither defects nor edge reconstructions were observed. The barrier corresponds to bending of the flake; after the first bond(s) is (are) formed, the transformation is barrierless. Folding along the armchair-edge requires a significantly lower barrier: indeed this edge is known to be more reactive than the zigzag-edge. We note that LCBOPII largely overestimates both these barriers. A possible explanation for this discrepancy could come from the unusually strained configurations that the system has to visit (transition state region) that were very different from the fitting/training sets originally used for the construction of the potential.

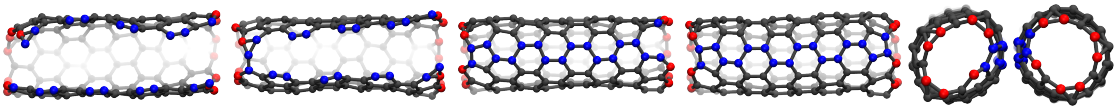

(a) Z: 29.6 ps **(b)** Z: 34.7 ps **(c)** Z: 36.1 ps **(d)** Z: 38.0 ps **(e)** left **(f)** right

Figure 7.2: *Ab initio* path-metadynamics: snapshots along the path leading the nanoflake to the zigzag (Z) CNT and sideviews of the final structure (e,f). Time denotes the MTD-time.

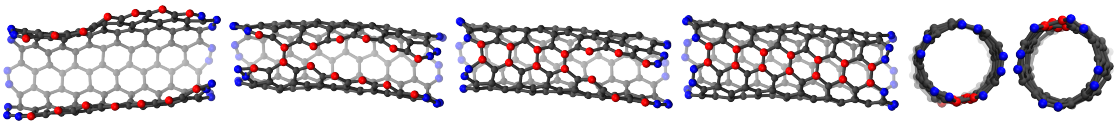

(a) A: 40.0 ps **(b)** A: 72.7 ps **(c)** A: 72.9 ps **(d)** A: 73.2 ps **(e)** left **(f)** right

Figure 7.3: *Ab initio* path-metadynamics: snapshots along the path leading the nanoflake to the armchair (A) CNT and sideviews of the final structure (e,f). Time denotes the MTD-time.

Starting from the same nanoflake model (Fig. 7.1(a)) we also performed one metadynamics simulation with the SPRINT CVs[123] at 1000 K. These coordinates are particularly useful in this case, since they do not require a predetermined structure for the product and may predict different final configurations and alternative pathways. Indeed we observed a transformation leading to the Z-nanotube through a very different path. Relevant steps are illustrated in Fig. 7.4. The first dramatic transformation corresponds to the closure of a 9-fold ring on one side (Fig. 7.4(a)), after which the edges progressively approach (Fig. 7.4(b)) and defects form and self-heal (c)-(d). The structure in (Fig. 7.4(d)) is still defective, having some non-hexagonal rings and two undercoordinated atoms. Once quenched, it is about 2eV higher than the "ideal" structure (Fig. 7.1(b)). This simulation will be continued also with simulated annealing. Others at higher temperature and starting from different initial conditions are also planned. Moreover, a separate series of metadynamics simulations using path-CVs will have to be applied to the "transition state" region to obtain a reasonably accurate estimate of the free energy barrier.[63]

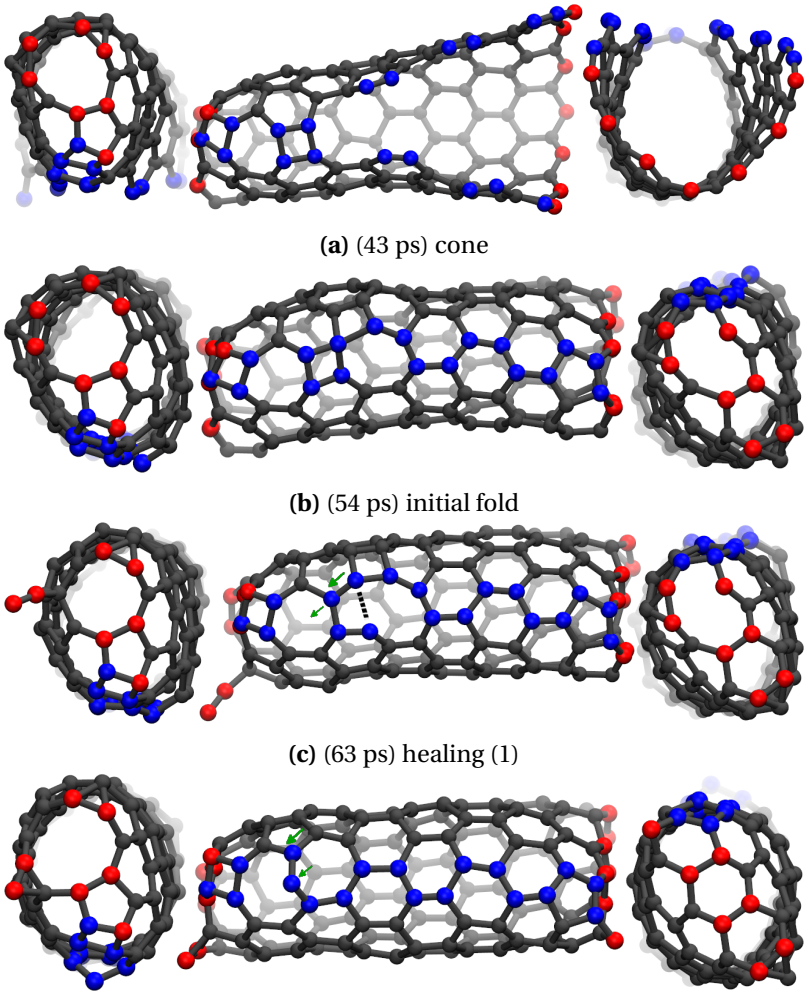

(a) (43 ps) cone

(b) (54 ps) initial fold

(c) (63 ps) healing (1)

(d) (65 ps) healing (2)

Figure 7.4: Structures (top- and side-views) along the SPRINT pathway toward the Z-nanotube.

The results presented above have provided hints on possible pathways for the folding of a small nanoflake and estimates for the associated barrier. One interesting message can already be derived from these preliminary calculations: the free-energy barriers to obtain tubular structures of different chirality can be very different, and much more sensitive than the relative energy differences.

A MPI Implementation of SPRINT

To reduce scaling and thereby the time needed for the SPRINT calculation we parallelized the code. An MPI communicator is used to reduce the group to the MPI size, in case more processors than atoms are used. Between the serial and MPI SPRINT implementation, the collective variables remain equal within printing accuracy (9 digits after the comma) during the a molecular dynamics run as shown in Fig. A.1. Adding the SPRINT forces of course changes the forces and therefore the evolution of the collective variables is different as can be seen in the right figure (black curves).

```
#ifdef SPRINT_MPI
  int mpirank, mpisize, mysize;
  MPI_Comm mycom;                                    // decrease mpi-size in
    case nat<mpisize
  MPI_Group mygroup, oldgroup;
  MPI_Comm_rank(MPI_COMM_WORLD,&mpirank);
  MPI_Comm_size(MPI_COMM_WORLD,&mpisize);
  MPI_Comm_group(MPI_COMM_WORLD, &oldgroup);         // create a new MPI
    group
  mysize = (mpisize>nat?nat:mpisize);                // number of procs used
    for computation
  int *ranks = int_1d_array_alloc(mysize);
  for(i=0;i<mysize;i++) ranks[i]=i;                  // include 0...mysize-1
  MPI_Group_incl(oldgroup, mysize, ranks, &mygroup); // create a group based
    on these ranks
  MPI_Comm_create(MPI_COMM_WORLD, mygroup, &mycom);  // create a communicator
     for this group
  int bufsize = 3*nat;
  real *in = float_1d_array_alloc(bufsize);
  real *buf = float_1d_array_alloc(bufsize);
#endif
        [[[ ........ DO THE REST OF THE SPRINT CALCULATION ...... ]]]
  real **D = sprint_data.cm;                         // diagonalized contact
    matrix
  real *lambda = sprint_data.lambda;                 // eigenvalues
  rvec *deriv = colvar.myder[i_c];                   // derivatives
#ifdef SPRINT_MPI
  for (i=mpirank;i<nat-1;i+=mysize) {                // loop-2 over cm (MPI)
#else
  for (i=0;i<nat-1;i++) {                            // loop-2 over cm
#endif
    for (j=i+1;j<nat;j++) {                          // loop-3 grad
```

```
27          tmp1 = 2.*D[i][nat-1]*D[j][nat-1];              // d lambda_N / d a_ij
28          tmp2 = 0.;                                      // d v_ii^N / d a_ij
29          for(k=0;k<nat-1;k++) {                          // loop-4
30            tmp2 += D[ind_sorted][k] * (D[i][k]*D[j][nat-1] + D[j][k]*D[i][nat
                -1])
31                                  / (lambda[nat-1]-lambda[k]);
32          }                                               // END loop-4
33          tmp3 = tmp1*D[ind_sorted][nat-1]+lambda[nat-1]*tmp2; // deriv of
              product lambda*v_i
34          for(ix=0;ix<3;ix++) {
35            deriv[i][ix]+=sqrtn*tmp3*sprint_data.grad[i][j][ix];
36            deriv[j][ix]-=sqrtn*tmp3*sprint_data.grad[i][j][ix];
37          }
38        }                                                 // END loop-3
39      }                                                   // END loop-2 over cm
40  #ifdef SPRINT_MPI
41    // gather data from procs
42    for(i=0;i<nat;i++) { for(j=0;j<3;j++) in[3*i+j]=deriv[i][j]; } // matrix ->
        vector
43    // all CP_GROUP master-nodes need the correct result: send sum to all procs
44    MPI_Allreduce(in, buf, bufsize , MPI_DOUBLE_PRECISION, MPI_SUM, mycom);
45    for(i=0;i<nat;i++) { for(j=0;j<3;j++) deriv[i][j]=buf[3*i+j]; } // vector ->
        matrix
46    // free arrays and MPI handles declared at the start of this function
47    MPI_Comm_free(&mycom); MPI_Group_free(&mygroup);
48    free_1dr_array_alloc(in);
49    free_1dr_array_alloc(buf);
50    free_1di_array_alloc(ranks);
51  #endif
```

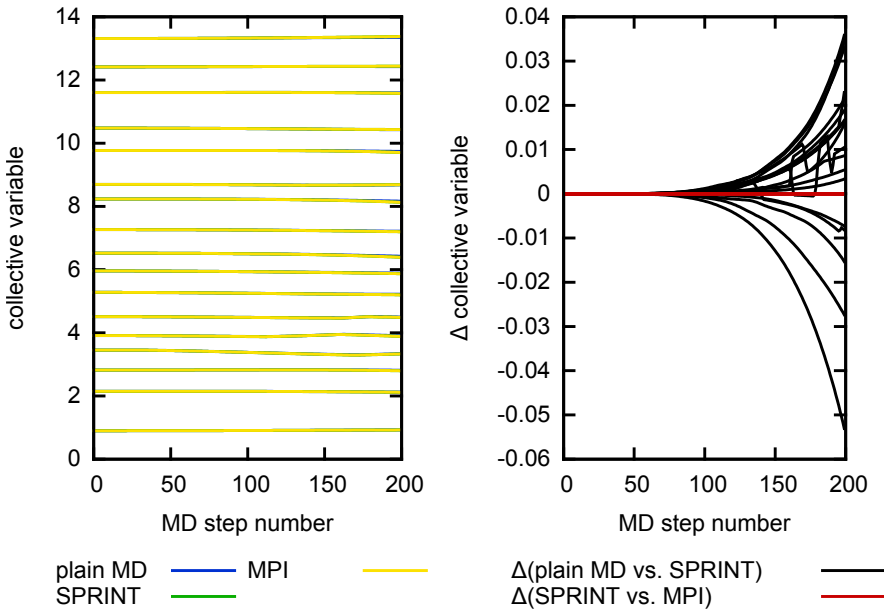

Figure A.1: The collective variables as function of the number of MD steps. On the left the values of 18 selected collective variables are shown. On the right, the difference between the different simulations are given: plain MD (without SPRINT), adding the SPRINT bias forces and using the MPI implementation of SPRINT.

B Oxygen Chemisorption

B.1 Atomic Ground State Reference

Binding energies in the main text are relative to the triplet ground state of atomic oxygen and sulfur. The energy difference between the triplet and spherical singlet is reported in Table. B.1.

xc–functional	O [pseudo]	O [AE]	S [pseudo]	S [AE]
BLYP	2.20	1.82	1.02	0.90
PBE	2.23	1.89	1.03	1.10
PBE0	5.11	4.91	2.88	2.84

Table B.1: Singlet–triplet energy splitting for oxygen and sulfur with the different functionals considered. All–electron (AE) calculations used the NWChem[195] code with the aug-cc–pVTZ basis set.

B.2 Structures and Binding Energies

Conf.		CC	CO	CC	CO
(2a)					
	PBE	2.20	1.39, 1.40	2.20	1.40, 1.39
	BLYP	2.24	1.40, 1.41	2.24	1.41, 1.40
(2b)					
	PBE	2.18	1.38, 1.40	2.18	1.40, 1.38
	BLYP	2.22	1.39, 1.41	2.22	1.41, 1.39
(2c)					
	PBE	2.16	1.36, 1.41	2.16	1.36, 1.41
	BLYP	2.20	1.37, 1.42	2.20	1.37, 1.42
(2d)					
	PBE	1.47	1.41, 1.51	2.27	1.37, 1.39
	BLYP	1.47	1.42, 1.55	2.29	1.38, 1.40

Table B.2: (10,0) CNT:2O. Comparison of some structural features and binding energies calculated within the PBE and BLYP functional schemes. In parenthesis the difference relative to the pristine CNT. Distances are in Å, angles in degrees. See Fig. 4.12.

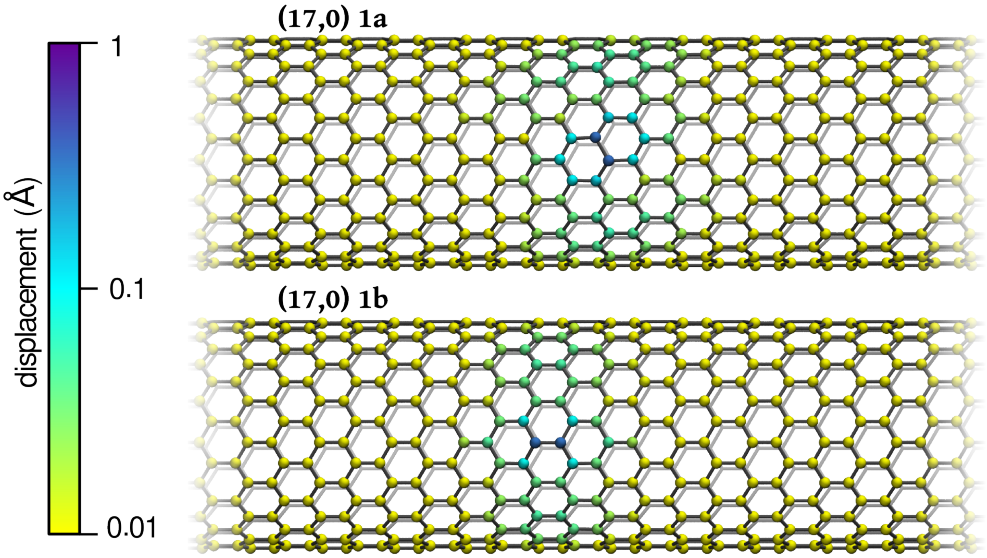

Figure B.1: (17,0) CNT:O. Displacements (in Å) of the C positions induced by O chemisorption.

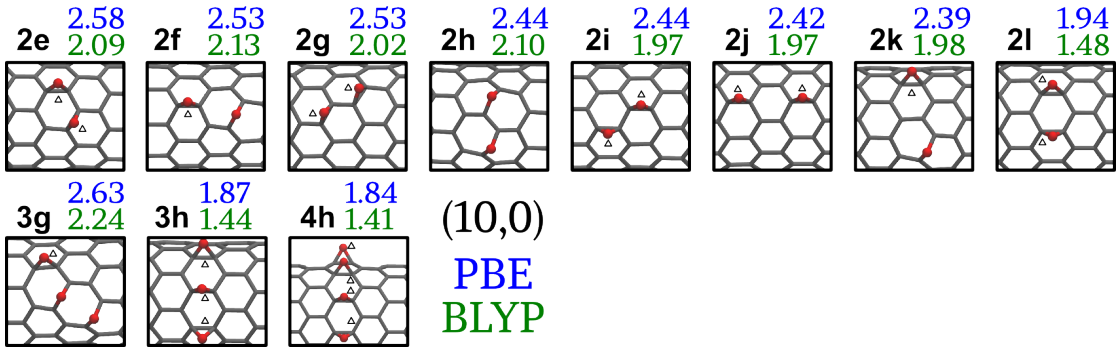

Figure B.2: (10,0) CNT:nO (n=1-4). Structures of chemisorbed oxygen for all cases with aggregation energy $E_c < 0$. Binding energies (in eV) refer to triplet oxygen. A small triangle indicates an EP.

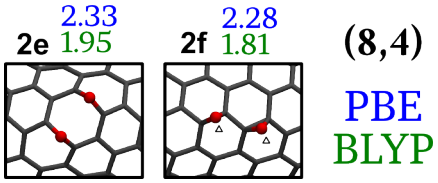

Figure B.3: (8,4) CNT:nO (n=1-2). Structures of chemisorbed oxygen for all cases with aggregation energy $E_c < 0$. Binding energies (in eV) refer to triplet oxygen. A small triangle indicates an EP.

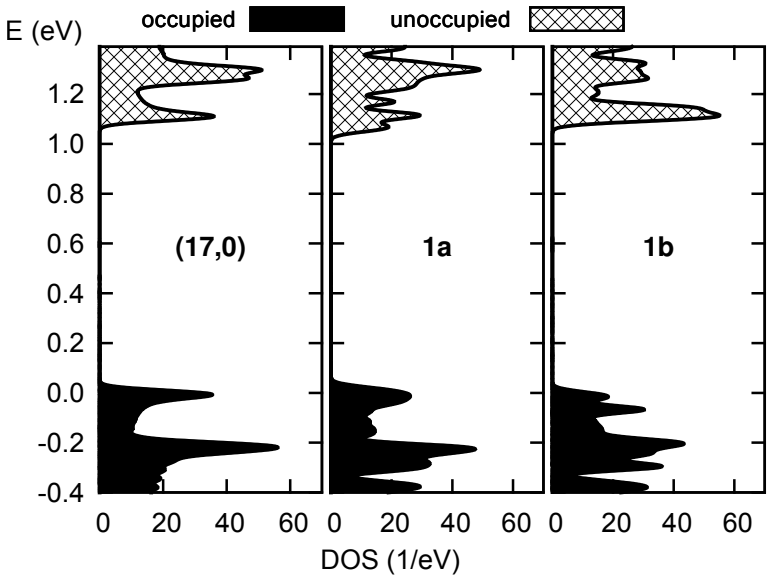

Figure B.4: (17,0)–CNT:O KS density of states.

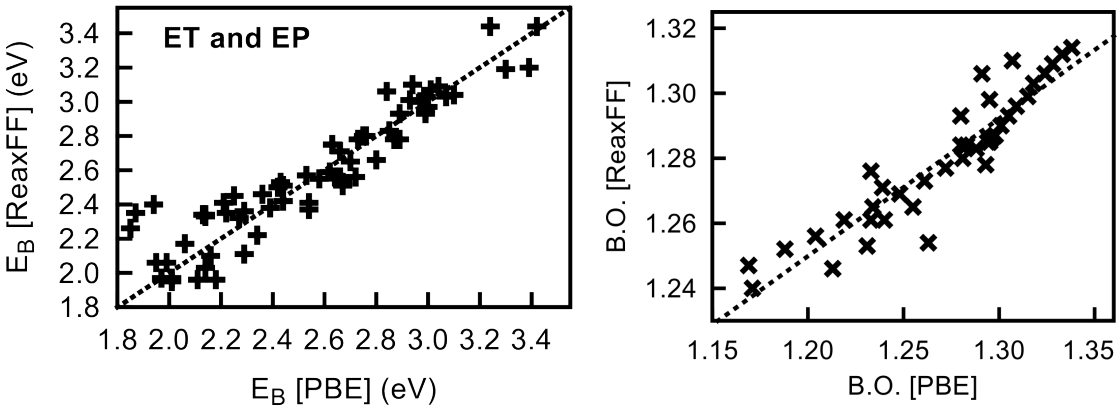

(a) binding energy correlation

(b) bond order correlation

Figure B.5: CNT:nO binding energy and bond order correlation between PBE and ReaxFF.

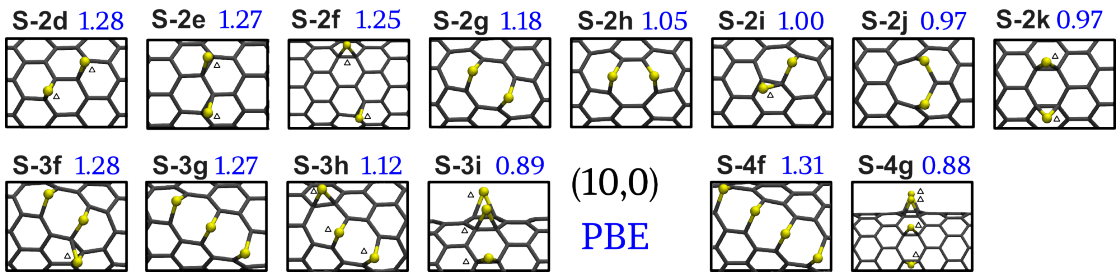

Figure B.6: (10,0) CNT:nO (n=1-4). Structures of chemisorbed sulphur for all cases with aggregation energy $E_c < 0$. Binding energies (in eV) refer to triplet sulphur. A small triangle indicates an EP.

Conf.		CC	CO	CC	CO	CC	CO
(3a)							
	PBE	2.18	1.39, 1.40	2.27	1.40, 1.40	2.18	1.40, 1.39
	BLYP	2.22	1.40, 1.41	2.32	1.41, 1.41	2.22	1.41, 1.40
(3b)							
	PBE	2.20	1.38, 1.40	2.27	1.40, 1.39	2.19	1.40, 1.39
	BLYP	2.24	1.39, 1.41	2.31	1.41, 1.41	2.23	1.41, 1.40
(3c)							
	PBE	1.46	1.41, 1.51	2.35	1.37, 1.40	2.23	1.40, 1.39
	BLYP	1.46	1.42, 1.54	2.37	1.38, 1.42	2.26	1.41, 1.40
(3d)							
	PBE	2.21	1.39, 1.40	1.54	1.49, 1.40	2.31	1.38, 1.40
	BLYP	2.24	1.40, 1.41	1.53	1.52, 1.42	2.34	1.40, 1.41
(3e)							
	PBE	2.23	1.39, 1.39	2.24	1.37, 1.37	2.23	1.39, 1.39
	BLYP	2.26	1.41, 1.41	2.25	1.38, 1.38	2.26	1.41, 1.41
(3f)							
	PBE	1.45	1.40, 1.53	2.28	1.37, 1.39	1.52	1.46, 1.45
	BLYP	1.45	1.41, 1.57	2.31	1.38, 1.41	1.53	1.49, 1.47

Table B.3: (10,0) CNT:3O. Comparison of some structural features and binding energies calculated within the PBE and BLYP functional schemes. In parenthesis the difference relative to the pristine CNT. Distances are in Å, angles in degrees. See Fig. 4.12.

Conf.		CC	CO	CC	CO	CC	CO	CC	CO
(4a)									
	PBE	2.17	1.39, 1.40	2.25	1.40, 1.40	2.25	1.40, 1.40	2.17	1.40, 1.39
	BLYP	2.21	1.40, 1.41	2.29	1.41, 1.41	2.29	1.41, 1.41	2.21	1.41, 1.40
(4b)									
	PBE	2.21	1.39, 1.39	2.40	1.41, 1.38	1.49	1.51, 1.40	2.18	1.40, 1.39
	BLYP	2.24	1.40, 1.41	2.44	1.42, 1.39	1.49	1.55, 1.41	2.22	1.41, 1.39
(4c)									
	PBE	2.24	1.39, 1.39	2.26	1.37, 1.36	2.30	1.40, 1.40	2.18	1.39, 1.39
	BLYP	2.27	1.40, 1.40	2.28	1.38, 1.37	2.33	1.41, 1.42	2.21	1.41, 1.40
(4d)									
	PBE	2.21	1.37, 1.39	1.54	1.48, 1.41	2.37	1.41, 1.40	2.18	1.40, 1.38
	BLYP	2.25	1.38, 1.40	1.54	1.51, 1.42	2.40	1.43, 1.41	2.22	1.41, 1.39
(4e)									
	PBE	1.50	1.45, 1.46	1.57	1.43, 1.45	2.23	1.39, 1.39	2.21	1.40, 1.39
	BLYP	1.50	1.47, 1.49	1.57	1.44, 1.47	2.27	1.40, 1.40	2.24	1.41, 1.40
(4f)									
	PBE	2.17	1.39, 1.40	2.28	1.39, 1.40	2.24	1.39, 1.39	1.54	1.46, 1.46
	BLYP	2.21	1.40, 1.41	2.32	1.40, 1.41	2.28	1.41, 1.40	1.54	1.48, 1.49
(4g)									
	PBE	1.46	1.41, 1.51	2.36	1.36, 1.40	2.27	1.40, 1.39	1.51	1.47, 1.46
	BLYP	1.45	1.42, 1.55	2.38	1.37, 1.42	2.30	1.41, 1.40	1.52	1.50, 1.48

Table B.4: (10,0) CNT:4O. Comparison of some structural features and binding energies calculated within the PBE and BLYP functional schemes. In parenthesis the difference relative to the pristine CNT. Distances are in Å, angles in degrees. See Fig. 4.12.

Conf.	CC	CO	CC	CO	CC	CO	CC	CO
(1a)	1.58	1.44, 1.44						
(1b)	1.50	1.47, 1.47						
(2a)	2.19	1.39, 1.39	2.19	1.39, 1.39				
(2b)	1.56	1.43, 1.46	1.56	1.46, 1.43				
(2c)	1.50	1.45, 1.47	1.54	1.43, 1.46				
(3a)	2.18	1.39, 1.39	2.29	1.39, 1.39	2.19	1.39, 1.39		
(3b)	2.19	1.39, 1.39	2.30	1.39, 1.40	2.21	1.39, 1.38		
(3c)	2.23	1.38, 1.39	2.35	1.40, 1.36	1.47	1.52, 1.41		
(3e)	2.24	1.39, 1.39	2.21	1.38, 1.38	2.24	1.39, 1.39		
(4a)	2.17	1.39, 1.39	2.28	1.39, 1.39	2.28	1.39, 1.39	2.17	1.39, 1.39
(4b)	2.22	1.38, 1.39	2.41	1.40, 1.38	1.50	1.51, 1.40	2.18	1.39, 1.39
(4e)	1.51	1.45, 1.46	1.57	1.43, 1.45	2.24	1.39, 1.39	2.21	1.39, 1.39

Table B.5: (17,0) CNT:nO. Distances for the selected structures of the main text as Table 1.

Conf.		CC	CO	CC	CO
(2a)					
	PBE	2.20	1.39, 1.40	2.20	1.40, 1.39
	ReaxFF	2.24	1.36, 1.37	2.24	1.37, 1.36
(2b)					
	PBE	2.18	1.38, 1.40	2.18	1.40, 1.38
	ReaxFF	2.26	1.39, 1.37	2.26	1.37, 1.39
(2c)					
	PBE	2.16	1.36, 1.41	2.16	1.36, 1.41
	ReaxFF	2.32	1.38, 1.37	2.32	1.38, 1.37
(2d)					
	PBE	1.47	1.41, 1.51	2.27	1.37, 1.39
	ReaxFF	1.51	1.37, 1.42	2.27	1.35, 1.42

Table B.6: (10,0) CNT:2O. Comparison of some structural features and binding energies calculated within the PBE and BLYP functional schemes. In parenthesis the difference relative to the pristine CNT. Distances are in Å, angles in degrees. Structures are in Fig. 4.24.

Conf.		CC	CO	CC	CO	CC	CO
(3a)							
	PBE	2.18	1.39, 1.40	2.27	1.40, 1.40	2.18	1.40, 1.39
	ReaxFF	2.24	1.36, 1.37	2.35	1.37, 1.37	2.24	1.37, 1.36
(3b)							
	PBE	2.20	1.38, 1.40	2.27	1.40, 1.39	2.19	1.40, 1.39
	ReaxFF	2.25	1.39, 1.37	2.34	1.36, 1.38	2.23	1.37, 1.37
(3c)							
	PBE	1.46	1.41, 1.51	2.35	1.37, 1.40	2.23	1.40, 1.39
	ReaxFF	1.41	1.37, 1.41	2.40	1.33, 1.47	2.24	1.37, 1.38
(3d)							
	PBE	2.21	1.39, 1.40	1.54	1.49, 1.40	2.31	1.38, 1.40
	ReaxFF	2.24	1.36, 1.38	1.53	1.52, 1.34	2.35	1.35, 1.44
(3e)							
	PBE	2.23	1.39, 1.39	2.24	1.37, 1.37	2.23	1.39, 1.39
	ReaxFF	2.23	1.39, 1.39	2.24	1.37, 1.37	2.23	1.39, 1.39
(3f)							
	PBE	1.45	1.40, 1.53	2.28	1.37, 1.39	1.52	1.46, 1.45
	ReaxFF	1.47	1.34, 1.49	2.32	1.35, 1.40	1.52	1.37, 1.42

Table B.7: (10,0) CNT:3O. Comparison of some structural features and binding energies calculated within the PBE and BLYP functional schemes. In parenthesis the difference relative to the pristine CNT. Distances are in Å, angles in degrees. Structures are in Fig. 4.24.

Conf.		CC	CO	CC	CO	CC	CO	CC	CO
(4a)									
	PBE	2.17	1.39, 1.40	2.25	1.40, 1.40	2.25	1.40, 1.40	2.17	1.40, 1.39
	ReaxFF	2.23	1.36, 1.37	2.34	1.37, 1.37	2.34	1.37, 1.37	2.23	1.37, 1.36
(4b)									
	PBE	2.21	1.39, 1.39	2.40	1.41, 1.38	1.49	1.51, 1.40	2.18	1.40, 1.39
	ReaxFF	2.25	1.37, 1.37	2.54	1.52, 1.32	1.42	1.48, 1.34	2.33	1.38, 1.36
(4c)									
	PBE	2.24	1.39, 1.39	2.26	1.37, 1.36	2.30	1.40, 1.40	2.18	1.39, 1.39
	ReaxFF	2.30	1.38, 1.39	2.26	1.37, 1.37	2.35	1.39, 1.37	2.22	1.37, 1.37
(4d)									
	PBE	2.21	1.37, 1.39	1.54	1.48, 1.41	2.37	1.41, 1.40	2.18	1.40, 1.38
	ReaxFF	2.30	1.40, 1.36	1.92	1.38, 1.39	2.70	1.28, 1.59	2.30	1.38, 1.36
(4e)									
	PBE	1.50	1.45, 1.46	1.57	1.43, 1.45	2.23	1.39, 1.39	2.21	1.40, 1.39
	ReaxFF	1.64	1.40, 1.38	1.76	1.36, 1.38	2.26	1.36, 1.37	2.23	1.37, 1.36
(4f)									
	PBE	2.17	1.39, 1.40	2.28	1.39, 1.40	2.24	1.39, 1.39	1.54	1.46, 1.46
	ReaxFF	2.24	1.36, 1.37	2.35	1.36, 1.36	2.29	1.37, 1.36	1.84	1.36, 1.44
(4g)									
	PBE	1.46	1.41, 1.51	2.36	1.36, 1.40	2.27	1.40, 1.39	1.51	1.47, 1.46
	ReaxFF	1.41	1.37, 1.41	2.45	1.34, 1.46	2.34	1.37, 1.37	1.50	1.52, 1.40

Table B.8: (10,0) CNT:4O. Comparison of some structural features and binding energies calculated within the PBE and BLYP functional schemes. In parenthesis the difference relative to the pristine CNT. Distances are in Å, angles in degrees. Structures are in Fig. 4.24.

Conf.	CC	CO	CC	CO	CC	CO	CC	CO
(1a)	1.76	1.39, 1.39						
(1b)	1.47	1.52, 1.39						
(2a)	2.23	1.36, 1.37	2.23	1.37, 1.36				
(2b)	1.80	1.38, 1.38	1.80	1.38, 1.38				
(2c)	1.50	1.47, 1.37	1.71	1.37, 1.40				
(3a)	2.24	1.36, 1.37	2.37	1.37, 1.37	2.24	1.37, 1.36		
(3b)	2.23	1.37, 1.37	2.37	1.38, 1.36	2.26	1.36, 1.39		
(3c)	2.24	1.38, 1.36	2.38	1.45, 1.34	1.42	1.42, 1.37		
(3e)	2.31	1.38, 1.39	2.24	1.38, 1.38	2.31	1.39, 1.38		
(4a)	2.24	1.36, 1.37	2.38	1.37, 1.37	2.38	1.37, 1.37	2.24	1.37, 1.36
(4b)	2.26	1.38, 1.36	2.55	1.51, 1.32	1.43	1.49, 1.35	2.33	1.37, 1.36
(4e)	1.51	1.50, 1.37	1.74	1.36, 1.39	2.27	1.36, 1.37	2.23	1.37, 1.36

Table B.9: (17,0) CNT:nO - ReaxFF. Distances for the selected structures of the main text as Table 1.

Conf.	CC	CO	CC	CO	CC	CO	CC	CO
(S-1a)	1.56	1.87, 1.87						
(S-1b)	1.50	1.87, 1.87						
(S-2a)	1.50	1.86, 1.87	1.50	1.87, 1.86				
(S-2b)	1.50	1.84, 1.88	1.50	1.88, 1.84				
(S-2c)	1.50	1.85, 1.88	1.53	1.84, 1.88				
(S-3a)	1.50	1.84, 1.87	1.50	1.84, 1.84	1.50	1.87, 1.84		
(S-3b)	1.49	1.86, 1.87	1.50	1.85, 1.85	1.49	1.87, 1.86		
(S-3c)	1.50	1.85, 1.88	1.53	1.83, 1.83	1.50	1.88, 1.85		
(S-3d)	1.50	1.85, 1.88	1.53	1.84, 1.88	1.50	1.87, 1.85		
(S-3e)	1.50	1.85, 1.87	1.50	1.84, 1.84	1.50	1.87, 1.85		
(S-4a)	1.50	1.84, 1.87	1.50	1.83, 1.84	1.50	1.84, 1.83	1.50	1.87, 1.84
(S-4b)	1.49	1.84, 1.87	1.50	1.84, 1.84	1.50	1.85, 1.83	1.49	1.87, 1.86
(S-4c)	1.49	1.85, 1.88	1.49	1.85, 1.86	1.49	1.86, 1.85	1.49	1.88, 1.85
(S-4d)	1.49	1.82, 1.87	1.51	1.84, 1.84	1.51	1.84, 1.84	1.49	1.87, 1.82
(S-4e)	1.49	1.83, 1.87	1.50	1.84, 1.83	1.50	1.84, 1.83	1.50	1.87, 1.85

Table B.10: (10,0) CNT:nS. Distances for selected structures of the main text as in Table 1.

B.3 Building up the Maps

SWNT	bond	d^i_{cc}	Θ_B	BO	d^f_{cc} [conf.]	pred.
(8,0)	Z	1.46	58	1.25	2.16 [ET]	ET
	A	1.43	0	1.31	1.57 [EP]	EP
(10,0)	Z	1.45	46	1.25	2.15 [ET]	ET
	A	1.43	0	1.31	1.57 [EP]	EP
(14,0)	Z	1.44	33	1.26	2.12 [ET]	ET
	A	1.44	0	1.30	1.57 [EP]	EP
(16,0)	Z	1.45	29	1.26	2.12 [ET]	EP
	A	1.44	0	1.29	1.57 [EP]	EP
(17,0)	Z	1.45	27	1.26	1.76 [EP/ET]	EP
	A	1.44	0	1.29	1.47 [EP]	EP
(19,0)	Z	1.45	24	1.26	1.76 [EP/ET]	EP
	A	1.44	0	1.29	1.57 [EP]	EP

Table B.11: (ReaxFF) Case n=1 of different nanotubes: Z=zigzag, A=axial, d^i_{cc}=BL prior to chemisorption (pristine tube), d^f_{cc}=BL in the final configuration (ET or EP), pred=prediction from limit-values

FROM	bond	d^i_{cc}	Θ_B	BO	TO	d^f_{cc} [conf.]	pred.
1a	Z	1.44	51	1.30	2a	2.24 [ET]	ET; EP
1a	Z	1.48	56	1.19	2b	2.26 [ET]	ET; ET
1a	Z	1.41	53	1.37	2c	2.32 [ET]	ET; EP
1a	A	1.41	28	1.37	2d	1.51 [EP]	EP; EP
1b	Z	1.50	55	1.12	2d	2.27 [ET]	ET; ET
1b	Z	1.43	47	1.33	2e	1.76 [ET/EP]	ET; EP
1b	A	1.42	1	1.34	2h	1.55 [EP]	EP; EP
1b	A	1.43	4	1.32	2i	1.47 [EP]	EP; EP
1b	Z	1.45	43	1.26	2j	2.12 [ET]	ET; EP
2a	Z	1.43	50	1.32	3a	2.24 [ET]	ET; EP
2a	Z	1.49	54	1.17	3b	2.25 [ET]	ET; ET
2a	A	1.39	16	1.42	3c	1.41 [EP]	EP; EP
2a	Z	1.39	55	1.42	3d	1.53 [EP]	ET; EP
2b	Z	1.44	52	1.29	3b	2.23 [ET]	ET; EP
2c	Z	1.43	52	1.32	3d	2.24 [ET]	ET; EP
2d	Z	1.45	53	1.24	3c	2.24 [ET]	ET; ET
2d	A	1.44	9	1.29	3f	1.52 [EP]	EP; EP
2e	A	1.43	9	1.30	3f	1.47 [EP]	EP; EP
2e	Z	1.45	49	1.25	3g	2.23 [ET]	ET; EP
2h	Z	1.49	58	1.16	3f	2.32 [ET]	ET; ET
3a	Z	1.43	50	1.32	4a	2.23 [ET]	ET; EP
3c	Z	1.43	52	1.31	4b	2.33 [ET]	ET; EP
3g	Z	1.48	57	1.19	4c	2.30 [ET]	ET; ET
3g	Z	1.45	50	1.26	4e	2.23 [ET]	ET; EP

Table B.12: ReaxFF - Data for the map.

FROM	bond	d^i_{cc}	Θ_B	BO	TO	d^f_{cc} [conf.]	pred.
1a	Z	1.46	32	1.25	2a	2.23 [ET]	ET; EP
1a	Z	1.45	32	1.27	2b	1.80 [ET/EP]	ET; EP
1a	A	1.43	4	1.30	2c	1.50 [EP]	EP; EP
1b	Z	1.43	30	1.25	2c	1.71 [ET/EP]	EP; ET
2a	Z	1.42	34	1.33	3a	2.24 [ET]	ET; EP
2a	Z	1.48	35	1.17	3b	2.26 [ET]	ET; ET
2a	A	1.39	15	1.42	3c	1.42 [EP]	EP; EP
2b	Z	1.45	33	1.26	3b	2.23 [ET]	ET; EP
2b	A	1.43	8	1.31	3e	2.24 [ET]	EP; EP
2c	Z	1.43	40	1.25	3e	2.31 [ET]	ET; EP
3a	Z	1.42	34	1.34	4a	2.24 [ET]	ET; EP
3a	A	1.39	16	1.43	4b	1.43 [EP]	EP; EP

Table B.13: (17,0):nO - (ReaxFF) Data for the map as in the tables above.

	FROM	bond	d^i_{cc}	Θ_B	BO	TO	d^f_{cc} [conf.]
(8,0)							
	n=0	A	1.42	0	1.31	S-1a	1.50 [EP]
		Z	1.43	57	1.21	S-1b	2.19 [EP]
(10,0)							
	n=0	A	1.42	0	1.29	S-1a	1.50 [EP]
		Z	1.43	46	1.23	S-1b	1.56 [EP]
	S-1a	Z	1.49	56	1.01	S-2i	2.48 [ET]
	S-1a	Z	1.41	47	1.37	S-2c	1.54 [EP]
	S-1a	A	1.41	1	1.32	S-2b	1.50 [EP]
	S-1b	A	1.47	6	1.37	S-2i	1.48 [EP]
	S-2a	A	1.40	1	1.41	S-3a	1.50 [EP]
	S-2a	A	1.41	5	1.35	S-3b	1.49 [EP]
	S-2b	A	1.40	4	1.37	S-3a	1.50 [EP]
	S-3a	A	1.40	3	1.28	S-4a	1.50 [EP]

Table B.14: (10,0):nS - Data for the map as in the tables above.

C Details of the Calculations

Ab Initio Calculations The main part of our DFT calculations rely on the CPMD code[97] using Martins-Troullier pseudopotentials[94] and a plane-wave basis set. PBE0 (B3LYP) calculations use the PBE (BLYP) pseudopotential so that the functional variation in the core-valence interaction is neglected. The results on oxygen, isoelectronic species and vacancies were obtained with a plane-wave cutoff of 100 Ry, whereas the results on hydrogen chemisorption and the folding were obtained with a cutoff of 55 Ry. For the total density a four times higher cutoff was used. Bond orders in Sec. 4.2 and projections for charge transfer in Ch. 5 were computed using the Slater TZ2Pfc (triple zeta frozen core 2-polarization) basis functions.[196] Mulliken populations in Sec. 4.1 were computed by projection on the pseudo atomic orbitals. Unless stated otherwise, all calculations were done using the Γ-point only of the corresponding Brillouin zone and considering only the lowest spin-multiplicity. The DOS figures shown in Chapter 4 were constructed using a 9 k-point Monkhorst-Pack grid[197] and unoccupied levels were shifted to match the PBE0 gap. Geometries were optimized using the quasi-Newton limited-memory Broyden-Fletcher-Goldfarb-Shanno method[198] until all nuclear gradients were less than 10^{-4} Ha/Bohr. For the computation of frequencies associated with the NO_x molecules on the CNT surface we consider only the partial Hessian associated with the nitrogen and oxygen atoms, neglecting possible off-diagonal elements. This choice is motivated by the fact that the interaction with the adducts is not of chemical nature, so that the effect of this approximation may be expected to be minimal. The periodic images in the isolated system calculations (for hydrogen chemisorption and folding) were decoupled using Hockney's Poisson solver[199] ensuring a vacuum between the molecules and cell edges of at least 10 Å.

All-electron calculations were performed with NWChem.[195] For hydrogen chemisorption we used the meta-hybrid M06 functional[200] with the aug-cc-pVDZ basis set for all atoms. The calculations of the singlet-triplet energy differences in Sec. B.1 were computed using the aug-cc-pVTZ basis set. Geometries were optimized using the "tight" settings in NWChem, corresponding to a maximum gradient of $1.5 \cdot 10^{-5}$ Ha/bohr.

For NO_x, PBE-D2 calculations of zigzag-CNTs for Fig. 5.3 were made with Quantum Espresso.[201] These calculations used ultrasoft van-der-Bilt pseudopotentials[131] with a plane-wave expansion up to 25 Ry (200 Ry for the density), Methfessel-Paxton[202] smearing of the occupation

numbers with a width of 0.01 Ry (i.e. similar to the methods in Ref.162). We used a double unit cell ($L_x \approx 8.5$ Å) with an 8×1×1 Monkhorst-Pack k-point grid. Geometries were optimized using the same scheme and criteria as for CPMD calculations described earlier.

Unless mentioned otherwise, the unit cells of our considered CNTs contain 36 rings for the (n,0) CNTs, and 336, 364 and 728 atoms for the (8,4), (6,5) and (12,10) CNTs respectively. Except for the calculations of Young's moduli, the unit cell is kept fixed at the value of the pristine CNT to facilitate total energy comparisons. Reference energies of the atoms and molecules are computed in the same cell.

Classical Calculations Calculations with REBO, AIREBO and LCBOP were done using the LAMMPS[203] code. The Reax code, kindly provided by prof. Adri van Duin, was used for calculations with ReaxFF. LCBOPII calculations were done with the Stamp code, kindly provided by dr. Nicolas Pineau of the Alternative Energies and Atomic Energy Commission (CEA) in France. Geometries for classical potentials were optimized to the same level as our *ab initio* results (maximum gradient of 10^{-4} Ha/Bohr) using the conjugate-gradient method in LAMMPS and Reax, and steepest-descent in the Stamp code.

Rare Events Static barriers were evaluated using the nudged elastic band method with a climbing image. The NEB implementation for CPMD was provided by gNEB.[204]

Temperature in our molecular dynamics (MD) simulations is controlled using a Nosé-Hoover chain thermostat.[104] The equations of motion are integrated using the velocity Verlet algorithm with a timestep of 3 atomic units for *ab initio* MD and 0.2 fs for classical MD. In the biased Car-Parrinello-MD simulations, the energy is quenched to the Born-Oppenheimer surface every 2000 time steps.

Finite temperature barriers computed with metadynamics used the PLUMED[205] code. A set of 14 frames was used to define the folding path in the path-CVs (so that $1 \geq s \leq 14$). Starting from a perfectly flat sample, reference frames were generated from the parametric transformation $(x, y, 0) \rightarrow (x, y \sin \tau_i, y \cos \tau_i)$, where $\tau_i = 2\theta_i \frac{x - x_{CM}}{L_x}$ with $0 \geq \theta_i \geq \pi$ chosen such that sequential frames are equidistant under the l^2-metric of the path-CVs. The perpendicular direction (z) is restricted by an additional spring force to prevent further unwanted exploration in the direction perpendicular to the constructed path. All atoms are used in the definition of the SPRINT coordinates, while the bias during the metadynamics was applied to every tenth CV including the highest and lowest eigenvalues.

Bibliography

[1] Iijima, S.; Ichihashi, T. Single-shell carbon nanotubes of 1-nm diameter. *Nature* **1993**, *363*, 603–605.

[2] Saito, R.; Dresselhaus, G.; Dresselhaus, M. S. *Physical Properties of Carbon Nanotube*; Imperial College Press, 1998.

[3] Dresselhaus, M. S.; Dresselhaus, G.; Avouris, P. H. *Carbon nanotubes: synthesis, structure, properties, and applications*; Springer: Berlin; New York, 2001.

[4] Hamada, N.; Sawada, S.-i.; Oshiyama, A. New one-dimensional conductors: Graphitic microtubules. *Phys. Rev. Lett.* **1992**, *68*, 1579–1581.

[5] Saito, R.; Fujita, M.; Dresselhaus, G.; Dresselhaus, M. S. Electronic structure of graphene tubules based on C60. *Phys. Rev. B* **1992**, *46*, 1804–1811.

[6] Saito, R.; Fujita, M.; Dresselhaus, G.; Dresselhaus, M. S. Electronic structure of chiral graphene tubules. *Applied Physics Letters* **1992**, *60*, 2204–2206.

[7] Odom, T. W.; Huang, J.-L.; Kim, P.; Lieber, C. M. Atomic structure and electronic properties of single-walled carbon nanotubes. *Nature* **1998**, *391*, 62–64.

[8] Wildöer, J. W. G.; Venema, L. C.; Rinzler, A. G.; Smalley, R. E.; Dekker, C. Electronic structure of atomically resolved carbon nanotubes. *Nature* **1998**, *391*, 59–62.

[9] Ouyang, M.; Huang, J.-L.; Cheung, C. L.; Lieber, C. M. Energy Gaps in "Metallic" Single-Walled Carbon Nanotubes. *Science* **2001**, *292*, 702–705.

[10] Gülseren, O.; Yildirim, T.; Ciraci, S. Tunable Adsorption on Carbon Nanotubes. *Phys. Rev. Lett.* **2001**, *87*, 116802.

[11] Chen, Z.; Thiel, W.; Hirsch, A. Reactivity of the Convex and Concave Surfaces of Single-Walled Carbon Nanotubes (SWCNTs) towards Addition Reactions: Dependence on the Carbon-Atom Pyramidalization. *ChemPhysChem* **2003**, *4*, 93–97.

[12] Niyogi, S.; Hamon, M. A.; Hu, H.; Zhao, B.; Bhowmik, P.; Sen, R.; Itkis, M. E.; Haddon, R. C. Chemistry of Single-Walled Carbon Nanotubes. *Acc. Chem. Res.* **2002**, *35*, 1105–1113.

[13] Hirsch, A. Functionalization of Single-Walled Carbon Nanotubes. *Angewandte Chemie International Edition* **2002**, *41*, 1853–1859.

[14] Jorio, A.; Dresselhaus, G.,; Dresselhaus, M. G. *Carbon Nanotubes: Advanced Topics in the Synthesis, Structure, Properties and Applications*; Springer, 2008; Vol. 10.

[15] Tulevski, G. S.; Franklin, A. D.; Afzali, A. High Purity Isolation and Quantification of Semiconducting Carbon Nanotubes via Column Chromatography. *ACS Nano* **2013**, *7*, 2971–2976.

[16] Zhang, R.; Zhang, Y.; Zhang, Q.; Xie, H.; Qian, W.; Wei, F. Growth of Half-Meter Long

Carbon Nanotubes Based on Schulz–Flory Distribution. *ACS Nano* **2013**, *7*, 6156–6161.

[17] Sugime, H.; Esconjauregui, S.; Yang, J.; D'Arsié, L.; Oliver, R. A.; Bhardwaj, S.; Cepek, C.; Robertson, J. Low temperature growth of ultra-high mass density carbon nanotube forests on conductive supports. *Appl. Phys. Lett.* **2013**, *103*, 073116.

[18] Yang, F. et al. Chirality-specific growth of single-walled carbon nanotubes on solid alloy catalysts. *Nature* **2014**, *510*, 522–524.

[19] (a) Banerjee, S.; Hemraj-Benny, T.; Wong, S. S. Covalent Surface Chemistry of Single-Walled Carbon Nanotubes. *Adv. Mater.* **2005**, *17*, 17–29; (b) Balasubramanian, K.; Burghard, M. Chemically Functionalized Carbon Nanotubes. *Small* **2005**, *1*, 180–192; (c) Peng, X.; Wong, S. S. Functional Covalent Chemistry of Carbon Nanotube Surfaces. *Adv. Mat.* **2009**, *21*, 625–642; (d) Gebhardt, B.; Syrgiannis, Z.; Backes, C.; Graupner, R.; Hauke, F.; Hirsch, A. Carbon Nanotube Sidewall Functionalization with Carbonyl Compounds—Modified Birch Conditions vs the Organometallic Reduction Approach. *J. Am. Chem. Soc.* **2011**, *133*, 7985–7995; (e) Hodge, S. A.; Bayazit, M. K.; Coleman, K. S.; Shaffer, M. S. P. Unweaving the rainbow: a review of the relationship between single-walled carbon nanotube molecular structures and their chemical reactivity. *Chem. Soc. Rev.* **2012**, *41*, 4409.

[20] Khare, B. N.; Meyyappan, M.; Cassell, A. M.; Nguyen, C. V.; Han, J. Functionalization of Carbon Nanotubes Using Atomic Hydrogen from a Glow Discharge. *Nano Lett.* **2002**, *2*, 73–77.

[21] Ruffieux, P.; Gröning, O.; Bielmann, M.; Gröning, P. Hydrogen chemisorption on sp 2 -bonded carbon: Influence of the local curvature and local electronic effects. *Appl Phys A* **2004**, *78*, 975–980.

[22] Zhang, G.; Qi, P.; Wang, X.; Lu, Y.; Mann, D.; Li, X.; Dai, H. Hydrogenation and Hydrocarbonation and Etching of Single-Walled Carbon Nanotubes. *J. Am. Chem. Soc.* **2006**, *128*, 6026–6027.

[23] Buchs, G.; Ruffieux, P.; Gröning, P.; Gröning, O. Scanning tunneling microscopy investigations of hydrogen plasma-induced electron scattering centers on single-walled carbon nanotubes. *Appl. Phys. Lett.* **2007**, *90*, 013104–013104–3.

[24] Nikitin, A.; Li, X.; Zhang, Z.; Ogasawara, H.; Dai, H.; Nilsson, A. Hydrogen Storage in Carbon Nanotubes through the Formation of Stable C-H Bonds. *Nano Lett.* **2008**, *8*, 162–167.

[25] Yoshihara, K.; Ishida, K.; Wongwiriyapan, W.; Inoue, S.; Okabayashi, Y.; Honda, S.-i.; Nishimoto, Y.; Kuwahara, Y.; Oura, K.; Katayama, M. Hydrogen Interaction with Single-Walled Carbon Nanotubes. *Appl. Phys. Express* **2008**, *1*, 094001.

[26] Kuznetsova, A.; Popova, I.; Yates,; Bronikowski, M. J.; Huffman, C. B.; Liu, J.; Smalley, R. E.; Hwu, H. H.; Chen, J. G. Oxygen-Containing Functional Groups on Single-Wall Carbon Nanotubes: NEXAFS and Vibrational Spectroscopic Studies. *J. Am. Chem. Soc.* **2001**, *123*, 10699–10704.

[27] Barberio, M.; Barone, P.; Bonanno, A.; Xu, F. Oxygen interaction with single-walled carbon nanotubes. *Superlattices and Microstructures* **2009**, *46*, 365–368.

[28] Kroes, J. M. H.; Pietrucci, F.; Curioni, A.; Jaafar, R.; Gröning, O.; Andreoni, W. Atomic Oxygen Chemisorption on Carbon Nanotubes Revisited with Theory and Experiment. *J. Phys. Chem. C* **2013**, *117*, 1948–1954.

[29] Liu, B.; Jiang, H.; Krasheninnikov, A. V.; Nasibulin, A. G.; Ren, W.; Liu, C.; Kauppinen, E. I.; Cheng, H.-M. Chirality-Dependent Reactivity of Individual Single-Walled Carbon Nanotubes. *Small* **2013**, *9*, 1379–1386.

[30] (a) Ajayan, P. M.; Ebbesen, T. W.; Ichihashi, T.; Iijima, S.; Tanigaki, K.; Hiura, H. Opening carbon nanotubes with oxygen and implications for filling. *Nature* **1993**, *362*, 522–525; (b) Collins, P. G.; Bradley, K.; Ishigami, M.; Zettl, A. Extreme Oxygen Sensitivity of Electronic Properties of Carbon Nanotubes. *Science* **2000**, *287*, 1801–1804.

[31] Larciprete, R.; Gardonio, S.; Petaccia, L.; Lizzit, S. Atomic oxygen functionalization of double walled C nanotubes. *Carbon* **2009**, *47*, 2579–2589.

[32] Curran, S. A.; Cech, J.; Zhang, D.; Dewald, J. L.; Avadhanula, A.; Kandadai, M.; Roth, S. Thiolation of carbon nanotubes and sidewall functionalization. *Journal of Materials Research* **2006**, *21*, 1012–1018.

[33] Kong, J.; Franklin, N. R.; Zhou, C.; Chapline, M. G.; Peng, S.; Cho, K.; Dai, H. Nanotube Molecular Wires as Chemical Sensors. *Science* **2000**, *287*, 622–625.

[34] Iqbal, N.; Afzal, A.; Cioffi, N.; Sabbatini, L.; Torsi, L. NOx sensing one- and two-dimensional carbon nanostructures and nanohybrids: Progress and perspectives. *Sens. Act. B* **2013**, *181*, 9–21.

[35] Heinze, S.; Tersoff, J.; Martel, R.; Derycke, V.; Appenzeller, J.; Avouris, P. Carbon Nanotubes as Schottky Barrier Transistors. *Phys. Rev. Lett.* **2002**, *89*, 106801.

[36] Vitale, V.; Curioni, A.; Andreoni, W. Metal-Carbon Nanotube Contacts: The Link between Schottky Barrier and Chemical Bonding. *J. Am. Chem. Soc.* **2008**, *130*, 5848–5849.

[37] Suehiro, J.; Imakiire, H.; Hidaka, S.-i.; Ding, W.; Zhou, G.; Imasaka, K.; Hara, M. Schottky-type response of carbon nanotube NO2 gas sensor fabricated onto aluminum electrodes by dielectrophoresis. *Sensors and Actuators B: Chemical* **2006**, *114*, 943–949.

[38] Chikkadi, K.; Muoth, M.; Maiwald, V.; Roman, C.; Hierold, C. Ultra-low power operation of self-heated, suspended carbon nanotube gas sensors. *Appl. Phys. Lett.* **2013**, *103*, 223109.

[39] Larciprete, R.; Petaccia, L.; Lizzit, S.; Goldoni, A. The Role of Metal Contact in the Sensitivity of Single-Walled Carbon Nanotubes to NO2. *J. Phys. Chem. C* **2007**, *111*, 12169–12174.

[40] Ruiz-Soria, G.; Pérez Paz, A.; Sauer, M.; Mowbray, D. J.; Lacovig, P.; Dalmiglio, M.; Lizzit, S.; Yanagi, K.; Rubio, A.; Goldoni, A.; Ayala, P.; Pichler, T. Revealing the Adsorption Mechanisms of Nitroxides on Ultrapure, Metallicity-Sorted Carbon Nanotubes. *ACS Nano* **2014**, *8*, 1375–1383.

[41] Zhao, J.; Buldum, A.; Han, J.; Lu, J. P. Gas molecule adsorption in carbon nanotubes and nanotube bundles. *Nanotechnology* **2002**, *13*, 195.

[42] Ellison, M. D.; Crotty, M. J.; Koh, D.; Spray, R. L.; Tate, K. E. Adsorption of NH3 and NO2 on Single-Walled Carbon Nanotubes. *J. Phys. Chem. B* **2004**, *108*, 7938–7943.

[43] Tolvanen, A.; Buchs, G.; Ruffieux, P.; Gröning, P.; Gröning, O.; Krasheninnikov, A. V. Modifying the electronic structure of semiconducting single-walled carbon nanotubes by Ar^+ ion irradiation. *Phys. Rev. B* **2009**, *79*, 125430.

[44] Collins, P. G. Defects and Disorder in Carbon Nanotubes. *Oxford Handbook of Nanoscience and Technology: Frontiers and Advances* **2010**,

[45] Dresselhaus, M. S.; Dresselhaus, G.; Jorio, A.; Souza Filho, A. G.; Saito, R. Raman spectroscopy on isolated single wall carbon nanotubes. *Carbon* **2002**, *40*, 2043–2061.

[46] Dresselhaus, M. S.; Dresselhaus, G.; Saito, R.; Jorio, A. Raman spectroscopy of carbon nanotubes. *Physics Reports* **2005**, *409*, 47–99.

[47] Malola, S.; Häkkinen, H.; Koskinen, P. Raman spectra of single-walled carbon nanotubes with vacancies. *Phys. Rev. B* **2008**, *77*, 155412.

[48] Buchs, G.; Krasheninnikov, A. V.; Ruffieux, P.; Gröning, P.; Foster, A. S.; Nieminen, R. M.; Gröning, O. Creation of paired electron states in the gap of semiconducting carbon nanotubes by correlated hydrogen adsorption. *New J. Phys.* **2007**, *9*, 275.

[49] Suenaga, K.; Wakabayashi, H.; Koshino, M.; Sato, Y.; Urita, K.; Iijima, S. Imaging active topological defects in carbon nanotubes. *Nat Nano* **2007**, *2*, 358–360.

[50] Krasheninnikov, A. V.; Nordlund, K. Ion and electron irradiation-induced effects in nanostructured materials. *J. Appl. Phys.* **2010**, *107*, 071301.

[51] Suzuki, S.; Yamaya, K.; Homma, Y.; Kobayashi, Y. Activation energy of healing of low-energy irradiation-induced defects in single-wall carbon nanotubes. *Carbon* **2010**, *48*, 3211–3217.

[52] Jin, C.; Suenaga, K.; Iijima, S. Vacancy Migrations in Carbon Nanotubes. *Nano Lett.* **2008**, *8*, 1127–1130.

[53] Börrnert, F.; Gorantla, S.; Bachmatiuk, A.; Warner, J. H.; Ibrahim, I.; Thomas, J.; Gemming, T.; Eckert, J.; Cuniberti, G.; Büchner, B.; Rümmeli, M. H. In situ observations of self-repairing single-walled carbon nanotubes. *Phys. Rev. B* **2010**, *81*, 201401.

[54] Geim, A. K.; Novoselov, K. S. The rise of graphene. *Nat Mater* **2007**, *6*, 183–191.

[55] Girit, Ç. Ö.; Meyer, J. C.; Erni, R.; Rossell, M. D.; Kisielowski, C.; Yang, L.; Park, C.-H.; Crommie, M. F.; Cohen, M. L.; Louie, S. G.; Zettl, A. Graphene at the Edge: Stability and Dynamics. *Science* **2009**, *323*, 1705–1708.

[56] Fasolino, A.; Los, J. H.; Katsnelson, M. I. Intrinsic ripples in graphene. *Nat Mater* **2007**, *6*, 858–861.

[57] Koskinen, P.; Malola, S.; Häkkinen, H. Self-Passivating Edge Reconstructions of Graphene. *Phys. Rev. Lett.* **2008**, *101*, 115502.

[58] Koskinen, P.; Malola, S.; Häkkinen, H. Evidence for graphene edges beyond zigzag and armchair. *Phys. Rev. B* **2009**, *80*, 073401.

[59] Shenoy, V. B.; Reddy, C. D.; Ramasubramaniam, A.; Zhang, Y. W. Edge-Stress-Induced Warping of Graphene Sheets and Nanoribbons. *Phys. Rev. Lett.* **2008**, *101*, 245501.

[60] Kotakoski, J.; Santos-Cottin, D.; Krasheninnikov, A. V. Stability of Graphene Edges under Electron Beam: Equilibrium Energetics versus Dynamic Effects. *ACS Nano* **2012**, *6*, 671–676.

[61] Chen, X.; Li, L.; Sun, X.; Kia, H. G.; Peng, H. A novel synthesis of graphene nanoscrolls with tunable dimension at a large scale. *Nanotechnology* **2012**, *23*, 055603.

[62] Chuvilin, A.; Kaiser, U.; Bichoutskaia, E.; Besley, N. A.; Khlobystov, A. N. Direct transformation of graphene to fullerene. *Nat Chem* **2010**, *2*, 450–453.

[63] Pietrucci, F.; Andreoni, W. Fate of a Graphene Flake: A New Route toward Fullerenes Disclosed with Ab Initio Simulations. *J. Chem. Theory Comput.* **2014**, *10*, 913–917.

[64] Ivanovskaya, V. V.; Zobelli, A.; Wagner, P.; Heggie, M. I.; Briddon, P. R.; Rayson, M. J.;

Ewels, C. P. Low-Energy Termination of Graphene Edges via the Formation of Narrow Nanotubes. *Phys. Rev. Lett.* **2011**, *107*, 065502.

[65] Akhukov, M. A.; Yuan, S.; Fasolino, A.; Katsnelson, M. I. Electronic, magnetic and transport properties of graphene ribbons terminated by nanotubes. *New J. Phys.* **2012**, *14*, 123012.

[66] Quintana, M.; Grzelczak, M.; Spyrou, K.; Calvaresi, M.; Bals, S.; Kooi, B.; Van Tendeloo, G.; Rudolf, P.; Zerbetto, F.; Prato, M. A Simple Road for the Transformation of Few-Layer Graphene into MWNTs. *J. Am. Chem. Soc.* **2012**, *134*, 13310–13315.

[67] Lim, H. E.; Miyata, Y.; Kitaura, R.; Nishimura, Y.; Nishimoto, Y.; Irle, S.; Warner, J. H.; Kataura, H.; Shinohara, H. Growth of carbon nanotubes via twisted graphene nanoribbons. *Nat Commun* **2013**, *4*.

[68] Kit, O. O.; Tallinen, T.; Mahadevan, L.; Timonen, J.; Koskinen, P. Twisting graphene nanoribbons into carbon nanotubes. *Phys. Rev. B* **2012**, *85*.

[69] Calvaresi, M.; Quintana, M.; Rudolf, P.; Zerbetto, F.; Prato, M. Rolling up a Graphene Sheet. *ChemPhysChem* **2013**, *14*, 3447–3453.

[70] Yu, D.; Liu, F. Synthesis of Carbon Nanotubes by Rolling up Patterned Graphene Nanoribbons Using Selective Atomic Adsorption. *Nano Lett.* **2007**, *7*, 3046–3050.

[71] Reddy, C. D.; Zhang, Y.-W. Structure manipulation of graphene by hydrogenation. *Carbon* **2014**, *69*, 86–91.

[72] Hohenberg, P.; Kohn, W. Inhomogeneous Electron Gas. *Phys. Rev.* **1964**, *136*, B864–B871.

[73] Kohn, W.; Sham, L. J. Self-Consistent Equations Including Exchange and Correlation Effects. *Phys. Rev.* **1965**, *140*, A1133–A1138.

[74] Dirac, P. a. M. Note on Exchange Phenomena in the Thomas Atom. *Mathematical Proceedings of the Cambridge Philosophical Society* **1930**, *26*, 376–385.

[75] Gell-Mann, M.; Brueckner, K. A. Correlation Energy of an Electron Gas at High Density. *Phys. Rev.* **1957**, *106*, 364–368.

[76] Carr, W. J. Energy, Specific Heat, and Magnetic Properties of the Low-Density Electron Gas. *Phys. Rev.* **1961**, *122*, 1437–1446.

[77] Ceperley, D. M.; Alder, B. J. Ground State of the Electron Gas by a Stochastic Method. *Phys. Rev. Lett.* **1980**, *45*, 566–569.

[78] Vosko, S. H.; Wilk, L.; Nusair, M. Accurate spin-dependent electron liquid correlation energies for local spin density calculations: a critical analysis. *Can. J. Phys.* **1980**, *58*, 1200–1211.

[79] Perdew, J. P.; Zunger, A. Self-interaction correction to density-functional approximations for many-electron systems. *Phys. Rev. B* **1981**, *23*, 5048–5079.

[80] Gross, E. K. U.; Dreizler, R. M. *Density Functional Theory*; Springer, 1995.

[81] Jones, R. O.; Gunnarsson, O. The density functional formalism, its applications and prospects. *Rev. Mod. Phys.* **1989**, *61*, 689–746.

[82] Langreth, D. C.; Perdew, J. P. Theory of nonuniform electronic systems. I. Analysis of the gradient approximation and a generalization that works. *Phys. Rev. B* **1980**, *21*, 5469–5493.

[83] Perdew, J. P. Accurate Density Functional for the Energy: Real-Space Cutoff of the Gradient Expansion for the Exchange Hole. *Phys. Rev. Lett.* **1985**, *55*, 1665–1668.

[84] Perdew, J. P.; Wang, Y. Accurate and simple density functional for the electronic exchange energy: Generalized gradient approximation. *Phys. Rev. B* **1986**, *33*, 8800–8802.

[85] (a) Perdew, J. P.; Burke, K.; Ernzerhof, M. Generalized Gradient Approximation Made Simple. *Phys. Rev. Lett.* **1996**, *77*, 3865–3868; (b) Perdew, J. P.; Burke, K.; Ernzerhof, M. Generalized Gradient Approximation Made Simple [Phys. Rev. Lett. 77, 3865 (1996)]. *Phys. Rev. Lett.* **1997**, *78*, 1396–1396.

[86] Becke, A. D. Density-functional exchange-energy approximation with correct asymptotic behavior. *Phys. Rev. A* **1988**, *38*, 3098–3100.

[87] Lee, C.; Yang, W.; Parr, R. G. Development of the Colle-Salvetti correlation-energy formula into a functional of the electron density. *Phys. Rev. B* **1988**, *37*, 785–789.

[88] Colle, R.; Salvetti, O. Approximate calculation of the correlation energy for the closed shells. *Theoret. Chim. Acta* **1975**, *37*, 329–334.

[89] Grimme, S. Semiempirical GGA-type density functional constructed with a long-range dispersion correction. *J. Comp. Chem.* **2006**, *27*, 1787–1799.

[90] Grimme, S.; Antony, J.; Ehrlich, S.; Krieg, H. A consistent and accurate ab initio parametrization of density functional dispersion correction (DFT-D) for the 94 elements H-Pu. *J. Chem. Phys.* **2010**, *132*, 154104.

[91] Adamo, C.; Barone, V. Toward reliable density functional methods without adjustable parameters: The PBE0 model. *J. Phys. Chem.* **1999**, *110*, 6158–6170.

[92] Stephens, P. J.; Devlin, F. J.; Chabalowski, C. F.; Frisch, M. J. Ab Initio Calculation of Vibrational Absorption and Circular Dichroism Spectra Using Density Functional Force Fields. *J. Phys. Chem.* **1994**, *98*, 11623–11627.

[93] Hamann, D. R.; Schlüter, M.; Chiang, C. Norm-Conserving Pseudopotentials. *Phys. Rev. Lett.* **1979**, *43*, 1494–1497.

[94] Troullier, N.; Martins, J. L. Efficient pseudopotentials for plane-wave calculations. *Phys. Rev. B* **1991**, *43*, 1993–2006.

[95] Goedecker, S.; Teter, M.; Hutter, J. Separable dual-space Gaussian pseudopotentials. *Phys. Rev. B* **1996**, *54*, 1703–1710.

[96] Payne, M. C.; Teter, M. P.; Allan, D. C.; Arias, T. A.; Joannopoulos, J. D. Iterative minimization techniques for ab initio total-energy calculations: molecular dynamics and conjugate gradients. *Rev. Mod. Phys.* **1992**, *64*, 1045–1097.

[97] CPMD, http://www.cpmd.org, Copyright IBM Corp 1990-2014, Copyright MPI für Festkörperforschung Stuttgart 1997-2001.

[98] Car, R.; Parrinello, M. Unified Approach for Molecular Dynamics and Density-Functional Theory. *Phys. Rev. Lett.* **1985**, *55*, 2471–2474.

[99] Grossman, J. C.; Schwegler, E.; Draeger, E. W.; Gygi, F.; Galli, G. Towards an assessment of the accuracy of density functional theory for first principles simulations of water. *The Journal of Chemical Physics* **2004**, *120*, 300–311.

[100] Verlet, L. Computer "Experiments" on Classical Fluids. I. Thermodynamical Properties of Lennard-Jones Molecules. *Phys. Rev.* **1967**, *159*, 98–103.

[101] Kühne, T. D.; Krack, M.; Mohamed, F. R.; Parrinello, M. Efficient and Accurate Car-Parrinello-like Approach to Born-Oppenheimer Molecular Dynamics. *Phys. Rev. Lett.* **2007**, *98*, 066401.

[102] Alavi, A.; Kohanoff, J.; Parrinello, M.; Frenkel, D. Ab Initio Molecular Dynamics with Excited Electrons. *Phys. Rev. Lett.* **1994**, *73*, 2599–2602.

[103] Nosé, S. A unified formulation of the constant temperature molecular dynamics methods. *J. Chem. Phys.* **1984**, *81*, 511–519.

[104] Hoover, W. G. Canonical dynamics: Equilibrium phase-space distributions. *Phys. Rev. A* **1985**, *31*, 1695–1697.

[105] Parrinello, M.; Rahman, A. Polymorphic transitions in single crystals: A new molecular dynamics method. *Journal of Applied Physics* **1981**, *52*, 7182–7190.

[106] Bernasconi, M.; Chiarotti, G. L.; Focher, P.; Scandolo, S.; Tosatti, E.; Parrinello, M. First-principle-constant pressure molecular dynamics. *Journal of Physics and Chemistry of Solids* **1995**, *56*, 501–505.

[107] Brenner, D. W.; Shenderova, O. A.; Harrison, J. A.; Stuart, S. J.; Ni, B.; Sinnott, S. B. A second-generation reactive empirical bond order (REBO) potential energy expression for hydrocarbons. *J. Phys.: Condens. Matter* **2002**, *14*, 783.

[108] Tersoff, J. New empirical model for the structural properties of silicon. *Phys. Rev. Lett.* **1986**, *56*, 632–635.

[109] Stuart, S. J.; Tutein, A. B.; Harrison, J. A. A reactive potential for hydrocarbons with intermolecular interactions. *J. Phys. Chem.* **2000**, *112*, 6472–6486.

[110] Los, J. H.; Fasolino, A. Intrinsic long-range bond-order potential for carbon: Performance in Monte Carlo simulations of graphitization. *Phys. Rev. B* **2003**, *68*, 024107.

[111] Los, J. H.; Ghiringhelli, L. M.; Meijer, E. J.; Fasolino, A. Improved long-range reactive bond-order potential for carbon. I. Construction. *Phys. Rev. B* **2005**, *72*, 214102.

[112] van Duin, A. C. T.; Dasgupta, S.; Lorant, F.; Goddard, W. A. ReaxFF: A Reactive Force Field for Hydrocarbons. *J. Phys. Chem. A* **2001**, *105*, 9396–9409.

[113] van Duin, A. C. T.; Strachan, A.; Stewman, S.; Zhang, Q.; Xu, X.; Goddard, W. A. ReaxFFSiO Reactive Force Field for Silicon and Silicon Oxide Systems. *J. Phys. Chem. A* **2003**, *107*, 3803–3811.

[114] Keith, J. A.; Fantauzzi, D.; Jacob, T.; van Duin, A. C. T. Reactive forcefield for simulating gold surfaces and nanoparticles. *Phys. Rev. B* **2010**, *81*, 235404.

[115] Kulkarni, A. D.; Truhlar, D. G.; Goverapet Srinivasan, S.; van Duin, A. C. T.; Norman, P.; Schwartzentruber, T. E. Oxygen Interactions with Silica Surfaces: Coupled Cluster and Density Functional Investigation and the Development of a New ReaxFF Potential. *J. Phys. Chem. C* **2013**, *117*, 258–269.

[116] Kim, S.-Y.; Kumar, N.; Persson, P.; Sofo, J.; van Duin, A. C. T.; Kubicki, J. D. Development of a ReaxFF Reactive Force Field for Titanium Dioxide/Water Systems. *Langmuir* **2013**, *29*, 7838–7846.

[117] Nielson, K. D.; van Duin, A. C. T.; Oxgaard, J.; Deng, W.-Q.; Goddard, W. A. Development of the ReaxFF Reactive Force Field for Describing Transition Metal Catalyzed Reactions, with Application to the Initial Stages of the Catalytic Formation of Carbon Nanotubes. *J. Phys. Chem. A* **2005**, *109*, 493–499.

[118] Henkelman, G.; Uberuaga, B. P.; Jónsson, H. A climbing image nudged elastic band method for finding saddle points and minimum energy paths. *J. Chem. Phys.* **2000**, *113*, 9901–9904.

[119] Chipot, C.; Pohorille, A. *Free Energy Calculations - Theory and Applications in Chemistry and Biology*; 2007.

[120] Laio, A.; Parrinello, M. Escaping free-energy minima. *PNAS* **2002**, *99*, 12562–12566.

[121] Geissler, P. L.; Dellago, C.; Chandler, D. Kinetic Pathways of Ion Pair Dissociation in Water. *J. Phys. Chem. B* **1999**, *103*, 3706–3710.

[122] Branduardi, D.; Gervasio, F. L.; Parrinello, M. From A to B in free energy space. *J. Chem. Phys.* **2007**, *126*, 054103.

[123] Pietrucci, F.; Andreoni, W. Graph Theory Meets Ab Initio Molecular Dynamics: Atomic Structures and Transformations at the Nanoscale. *Phys. Rev. Lett.* **2011**, *107*, 085504.

[124] Barone, V.; Heyd, J.; Scuseria, G. E. Interaction of atomic hydrogen with single-walled carbon nanotubes: A density functional theory study. *J. Chem. Phys.* **2004**, *120*, 7169–7173.

[125] Han, S. S.; Lee, H. M. Adsorption properties of hydrogen on (10,0) single-walled carbon nanotube through density functional theory. *Carbon* **2004**, *42*, 2169–2177.

[126] Nikitin, A.; Zhang, Z.; Nilsson, A. Energetics of C-H Bonds Formed at Single-Walled Carbon Nanotubes. *Nano Lett.* **2009**, *9*, 1301–1306.

[127] Muniz, A. R.; Maroudas, D. Hydrogenation effects on the structure and morphology of graphene and single-walled carbon nanotubes. *J. Appl. Phys.* **2010**, *108*, 113532.

[128] Heyd, J.; Scuseria, G. E.; Ernzerhof, M. Hybrid functionals based on a screened Coulomb potential. *J. Phys. Chem.* **2003**, *118*, 8207–8215.

[129] Yildirim, T.; Gülseren, O.; Ciraci, S. Exohydrogenated single-wall carbon nanotubes. *Phys. Rev. B* **2001**, *64*, 075404.

[130] Perdew, J. P.; Chevary, J. A.; Vosko, S. H.; Jackson, K. A.; Pederson, M. R.; Singh, D. J.; Fiolhais, C. Atoms, molecules, solids, and surfaces: Applications of the generalized gradient approximation for exchange and correlation. *Phys. Rev. B* **1992**, *46*, 6671–6687.

[131] Vanderbilt, D. Soft self-consistent pseudopotentials in a generalized eigenvalue formalism. *Phys. Rev. B* **1990**, *41*, 7892–7895.

[132] Andreoni, W.; Curioni, A.; Kroes, J. M. H.; Pietrucci, F.; Gröning, O. Exohedral Hydrogen Chemisorption on a Carbon Nanotube: The Clustering Effect. *J. Phys. Chem. C* **2012**, *116*, 269–275.

[133] Haddon, R. C. C60: Sphere or Polyhedron? *J. Am. Chem. Soc.* **1997**, *119*, 1797–1798.

[134] Kastner, J.; Pichler, T.; Kuzmany, H.; Curran, S.; Blau, W.; Weldon, D. N.; Delamesiere, M.; Draper, S.; Zandbergen, H. Resonance Raman and infrared spectroscopy of carbon nanotubes. *Chem. Phys. Lett.* **1994**, *221*, 53–58.

[135] Muniz, A. R.; Singh, T.; Maroudas, D. Effects of hydrogen chemisorption on the structure and deformation of single-walled carbon nanotubes. *Appl. Phys. Lett.* **2009**, *94*, 103108.

[136] Boukhvalov, D. W.; Katsnelson, M. I.; Lichtenstein, A. I. Hydrogen on graphene: Electronic structure, total energy, structural distortions and magnetism from first-principles calculations. *Phys. Rev. B* **2008**, *77*, 035427.

[137] Lee, S. M.; An, K. H.; Lee, Y. H.; Seifert, G.; Frauenheim, T. A Hydrogen Storage Mechanism in Single-Walled Carbon Nanotubes. *J. Am. Chem. Soc.* **2001**, *123*, 5059–5063.

[138] Kroes, J. M. H.; Pietrucci, F.; Curioni, A.; Andreoni, W. Characterizing and Understanding Divalent Adsorbates on Carbon Nanotubes with Ab Initio and Classical Approaches:

Size, Chirality, and Coverage Effects. *J. Chem. Theory Comput.* **2014**, *10*, 4672–4683.

[139] Liu, H. J.; Chan, C. T.; Liu, Z. Y.; Shi, J. Density functional study of oxygen adsorption on 4-Å carbon nanotubes. *Phys. Rev. B* **2005**, *72*, 075437.

[140] Kresse, G.; Hafner, J. Norm-conserving and ultrasoft pseudopotentials for first-row and transition elements. *J. Phys.: Condens. Matter* **1994**, *6*, 8245.

[141] Barone, V.; Heyd, J.; Scuseria, G. E. Effect of oxygen chemisorption on the energy band gap of a chiral semiconducting single-walled carbon nanotube. *Chem. Phys. Lett.* **2004**, *389*, 289–292.

[142] Froudakis, G. E.; Schnell, M.; Mühlhäuser, M.; Peyerimhoff, S. D.; Andriotis, A. N.; Menon, M.; Sheetz, R. M. Pathways for oxygen adsorption on single-wall carbon nanotubes. *Phys. Rev. B* **2003**, *68*, 115435.

[143] Khorrampour, R.; Esrafili, M. D.; Hadipour, N. L. Density functional theory study of atomic oxygen, O2 and O3 adsorptions on the H-capped (5,0) single-walled carbon nanotube. *Physica E: Low-dimensional Systems and Nanostructures* **2009**, *41*, 1373–1378.

[144] Dag, S.; Gülseren, O.; Yildirim, T.; Ciraci, S. Oxygenation of carbon nanotubes: Atomic structure, energetics, and electronic structure. *Phys. Rev. B* **2003**, *67*, 165424.

[145] Zheng, G.; Wang, Z.; Irle, S.; Morokuma, K. Origin of the Linear Relationship between CH2/NH/O-SWNT Reaction Energies and Sidewall Curvature: Armchair Nanotubes. *J. Am. Chem. Soc.* **2006**, *128*, 15117–15126.

[146] Lu, J.; Nagase, S.; Zhang, X.; Maeda, Y.; Wakahara, T.; Nakahodo, T.; Tsuchiya, T.; Akasaka, T.; Yu, D.; Gao, Z.; Han, R.; Ye, H. Structural evolution of [2+1] cycloaddition derivatives of single-wall carbon nanotubes: From open structure to closed three-membered ring structure with increasing tube diameter. *J. Mol. Struct. (theochem)* **2005**, *725*, 255–257.

[147] Lee, Y.-S.; Marzari, N. Cycloaddition Functionalizations to Preserve or Control the Conductance of Carbon Nanotubes. *Phys. Rev. Lett.* **2006**, *97*.

[148] Li, J.; Jia, G.; Zhang, Y.; Chen, Y. Bond-Curvature Effect of Sidewall [2+1] Cycloadditions of Single-Walled Carbon Nanotubes: A New Criterion To the Adduct Structures. *Chem. Mater.* **2006**, *18*, 3579–3584.

[149] Li, J.; Jia, G.; Zhang, Y. Chemical Anisotropies of Carbon Nanotubes and Fullerenes Caused by the Curvature Directivity. *Chem.* **2007**, *13*, 6430–6436.

[150] Li, E. Y.; Poilvert, N.; Marzari, N. Switchable Conductance in Functionalized Carbon Nanotubes via Reversible Sidewall Bond Cleavage. *ACS Nano* **2011**, *5*, 4455–4465.

[151] Lu, X.; Sun, C.; Li, F.; Cheng, H.-M. Selected absorption behavior of sulfur on single-walled carbon nanotubes by DFT. *Chem. Phys. Lett.* **2008**, *454*, 305–309.

[152] Denis, P. A.; Faccio, R. Theoretical characterization of thioepoxidated single wall carbon nanotubes. *Chem. Phys. Lett.* **2008**, *460*, 486–491.

[153] McNicholas, T. P.; Ding, L.; Yuan, D.; Liu, J. Density Enhancement of Aligned Single-Walled Carbon Nanotube Thin Films on Quartz Substrates by Sulfur-Assisted Synthesis. *Nano Lett.* **2009**, *9*, 3646–3650.

[154] Bercioux, D.; Buchs, G.; Grabert, H.; Gröning, O. Defect-induced multicomponent electron scattering in single-walled carbon nanotubes. *Phys. Rev. B* **2011**, *83*, 165439.

[155] Bronikowski, M. J.; Willis, P. A.; Colbert, D. T.; Smith, K. A.; Smalley, R. E. Gas-phase

production of carbon single-walled nanotubes from carbon monoxide via the HiPco process: A parametric study. *Journal of Vacuum Science & Technology A* **2001**, *19*, 1800–1805.

[156] Yan, J.-A.; Chou, M. Y. Oxidation functional groups on graphene: Structural and electronic properties. *Phys. Rev. B* **2010**, *82*, 125403.

[157] Sun, T.; Fabris, S. Mechanisms for Oxidative Unzipping and Cutting of Graphene. *Nano Lett.* **2012**, *12*, 17–21.

[158] Hossain, M. Z.; Johns, J. E.; Bevan, K. H.; Karmel, H. J.; Liang, Y. T.; Yoshimoto, S.; Mukai, K.; Koitaya, T.; Yoshinobu, J.; Kawai, M.; Lear, A. M.; Kesmodel, L. L.; Tait, S. L.; Hersam, M. C. Chemically homogeneous and thermally reversible oxidation of epitaxial graphene. *Nat Chem* **2012**, *4*, 305–309.

[159] Bridgeman, A. J.; Cavigliasso, G.; Ireland, L. R.; Rothery, J. The Mayer bond order as a tool in inorganic chemistry. *J. Chem. Soc., Dalton Trans.* **2001**, 2095–2108.

[160] Chen, Z.; Nagase, S.; Hirsch, A.; Haddon, R. C.; Thiel, W.; Schleyer, P. v. R. Side-Wall Opening of Single-Walled Carbon Nanotubes (SWCNTs) by Chemical Modification: A Critical Theoretical Study. *Angew. Chem.* **2004**, *116*, 1578–1580.

[161] Li, E. Y.; Marzari, N. Improving the Electrical Conductivity of Carbon Nanotube Networks: A First-Principles Study. *ACS Nano* **2011**, *5*, 9726–9736.

[162] Dai, J.; Giannozzi, P.; Yuan, J. Adsorption of pairs of NOx molecules on single-walled carbon nanotubes and formation of NO + NO3 from NO2. *Surf. Sci.* **2009**, *603*, 3234–3238.

[163] Kanai, Y.; Khalap, V. R.; Grossman, J. C. Atomistic Oxidation Mechanism of a Carbon Nanotube in Nitric Acid. *Phys. Rev. Lett.* **2010**, *104*, 066401.

[164] Peng, S.; Cho, K. Chemical control of nanotube electronics. *Nanotechnology* **2000**, *11*, 57.

[165] Chang, H.; Lee, J. D.; Lee, S. M.; Lee, Y. H. Adsorption of NH3 and NO2 molecules on carbon nanotubes. *Appl. Phys. Lett.* **2001**, *79*, 3863–3865.

[166] Perdew, J. P.; Wang, Y. Accurate and simple analytic representation of the electron-gas correlation energy. *Phys. Rev. B* **1992**, *45*, 13244–13249.

[167] Santucci, S.; Picozzi, S.; Di Gregorio, F.; Lozzi, L.; Cantalini, C.; Valentini, L.; Kenny, J. M.; Delley, B. NO2 and CO gas adsorption on carbon nanotubes: Experiment and theory. *J. Phys. Chem.* **2003**, *119*, 10904–10910.

[168] Peng, S.; Cho, K.; Qi, P.; Dai, H. Ab initio study of CNT NO2 gas sensor. *Chem. Phys. Lett.* **2004**, *387*, 271–276.

[169] Sjövall, P.; So, S. K.; Kasemo, B.; Franchy, R.; Ho, W. NO2 adsorption on graphite at 90 K. *Chem. Phys. Lett.* **1990**, *172*, 125–130.

[170] Liu, W.-G.; Goddard, W. A. First-Principles Study of the Role of Interconversion Between NO2, N2O4, cis-ONO-NO2, and trans-ONO-NO2 in Chemical Processes. *J. Am. Chem. Soc.* **2012**, *134*, 12970–12978.

[171] Inoue, G.; Nakataa, Y.; Usuia, Y.; Akimoto, H.; Okuda, M. Emission of NO2* formed in the photodissociation of N2O4. *The Journal of Chemical Physics* **1979**, *70*, 3689–3693.

[172] Snyder, S. E.; Rotkin, S. V. Polarization component of cohesion energy in single-wall carbon nanotube-DNA complexes. *Jetp Lett.* **2006**, *84*, 348–351.

[173] Ricca, A.; Bauschlicher Jr., C. W. The adsorption of NO2 on (9,0) and (10,0) carbon nanotubes. *Chem. Phys.* **2006**, *323*, 511–518.

[174] Lawson, J. W.; Bauschlicher Jr., C. W.; Toulouse, J.; Filippi, C.; Umrigar, C. J. Quantum Monte Carlo study of the cooperative binding of NO2 to fragment models of carbon nanotubes. *Chem. Phys. Lett.* **2008**, *466*, 170–175.

[175] Hadjiivanov, K. I. Identification of Neutral and Charged N x O y Surface Species by IR Spectroscopy. *Cat. Rev.* **2000**, *42*, 71–144.

[176] Nelson, H. H.; Pasternack, L.; McDonald, J. R. Laser-induced excitation and emission spectra of nitrate radical (NO3). *J. Phys. Chem.* **1983**, *87*, 1286–1288.

[177] Schaffert, R. The Infrared Absorption Spectra of NO2 and N2O4. *The Journal of Chemical Physics* **1933**, *1*, 507–511.

[178] Snyder, R. G.; Hisatsune, I. C. Infrared Spectrum of N2O4. *The Journal of Chemical Physics* **1957**, *26*, 960–960.

[179] Baroni, S.; de Gironcoli, S.; Dal Corso, A.; Giannozzi, P. Phonons and related crystal properties from density-functional perturbation theory. *Rev. Mod. Phys.* **2001**, *73*, 515–562.

[180] Mercuri, F.; Sgamellotti, A.; Valentini, L.; Armentano, I.; Kenny, J. M. Vacancy-Induced Chemisorption of NO2 on Carbon Nanotubes: A Combined Theoretical and Experimental Study. *J. Phys. Chem. B* **2005**, *109*, 13175–13179.

[181] Liu, A. C. Y.; Arenal, R.; Montagnac, G. In situ transmission electron microscopy observation of keV-ion irradiation of single-walled carbon and boron nitride nanotubes. *Carbon* **2013**, *62*, 248–255.

[182] Kroes, J. M. H.; Pietrucci, F.; Andreoni, W. Single and Double Vacancies on SWNT sidewalls: Comparison of DFT and Classical Forcefield Predictions (manuscript in preparation).

[183] Ma, Y.; Lehtinen, P. O.; Foster, A. S.; Nieminen, R. M. Magnetic properties of vacancies in graphene and single-walled carbon nanotubes. *New J. Phys.* **2004**, *6*, 68.

[184] Berber, S.; Oshiyama, A. Reconstruction of mono-vacancies in carbon nanotubes: Atomic relaxation vs. spin polarization. *Physica B: Condensed Matter* **2006**, *376–377*, 272–275.

[185] Orellana, W.; Fuentealba, P. Structural, electronic and magnetic properties of vacancies in single-walled carbon nanotubes. *Surface Science* **2006**, *600*, 4305–4309.

[186] Krasheninnikov, A.; Lehtinen, P.; Foster, A.; Nieminen, R. Bending the rules: Contrasting vacancy energetics and migration in graphite and carbon nanotubes. *Chem. Phys. Lett.* **2006**, *418*, 132–136.

[187] Kotakoski, J.; Krasheninnikov, A. V.; Nordlund, K. Energetics, structure, and long-range interaction of vacancy-type defects in carbon nanotubes: Atomistic simulations. *Phys. Rev. B* **2006**, *74*, 245420.

[188] Padilha, J. E.; Amorim, R. G.; Rocha, A. R.; da Silva, A. J. R.; Fazzio, A. Energetics and stability of vacancies in carbon nanotubes. *Solid State Communications* **2011**, *151*, 482–486.

[189] Mielke, S. L.; Troya, D.; Zhang, S.; Li, J.-L.; Xiao, S.; Car, R.; Ruoff, R. S.; Schatz, G. C.; Belytschko, T. The role of vacancy defects and holes in the fracture of carbon nanotubes.

Chem. Phys. Lett. **2004**, *390*, 413–420.

[190] Kresse, G.; Joubert, D. From ultrasoft pseudopotentials to the projector augmented-wave method. *Phys. Rev. B* **1999**, *59*, 1758–1775.

[191] Saidi, W. A. Effects of Topological Defects and Diatom Vacancies on Characteristic Vibration Modes and Raman Intensities of Zigzag Single-Walled Carbon Nanotubes. *J. Phys. Chem. A* **2013**,

[192] Krasheninnikov, A. V.; Nordlund, K.; Keinonen, J. Production of defects in supported carbon nanotubes under ion irradiation. *Phys. Rev. B* **2002**, *65*, 165423.

[193] Sammalkorpi, M.; Krasheninnikov, A.; Kuronen, A.; Nordlund, K.; Kaski, K. Mechanical properties of carbon nanotubes with vacancies and related defects. *Phys. Rev. B* **2004**, *70*, 245416.

[194] Brenner, D. W. Empirical potential for hydrocarbons for use in simulating the chemical vapor deposition of diamond films. *Phys. Rev. B* **1990**, *42*, 9458–9471.

[195] Valiev, M.; Bylaska, E. J.; Govind, N.; Kowalski, K.; Straatsma, T. P.; Van Dam, H. J. J.; Wang, D.; Nieplocha, J.; Apra, E.; Windus, T. L.; de Jong, W. A. NWChem: A comprehensive and scalable open-source solution for large scale molecular simulations. *Computer Physics Communications* **2010**, *181*, 1477–1489.

[196] Van Lenthe, E.; Baerends, E. J. Optimized Slater-type basis sets for the elements 1–118. *J. Comput. Chem.* **2003**, *24*, 1142–1156.

[197] Monkhorst, H. J.; Pack, J. D. Special points for Brillouin-zone integrations. *Phys. Rev. B* **1976**, *13*, 5188–5192.

[198] Billeter, S. R.; Curioni, A.; Andreoni, W. Efficient linear scaling geometry optimization and transition-state search for direct wavefunction optimization schemes in density functional theory using a plane-wave basis. *Comp. Mat. Sc.* **2003**, *27*, 437–445.

[199] Hockney, R. W. The Potential Calculation and Some Applications. **1970**, *9*, 136–211.

[200] Zhao, Y.; Truhlar, D. G. Density Functionals with Broad Applicability in Chemistry. *Acc. Chem. Res.* **2008**, *41*, 157–167.

[201] Giannozzi, P. et al. QUANTUM ESPRESSO: a modular and open-source software project for quantum simulations of materials. *J. Phys.: Condens. Matter* **2009**, *21*, 395502.

[202] Methfessel, M.; Paxton, A. T. High-precision sampling for Brillouin-zone integration in metals. *Phys. Rev. B* **1989**, *40*, 3616–3621.

[203] Plimpton, S. Fast Parallel Algorithms for Short-Range Molecular Dynamics. *J. Comp. Theor. Nanosci.* **1995**, *117*, 1–19.

[204] Sraccia, C. Computer Simulation of Thermally Activated Processes. Ph.D. thesis, Scuola Internazionale Superiore di Studi Avanzati (SISSA), Trieste, 2005.

[205] Bonomi, M.; Branduardi, D.; Bussi, G.; Camilloni, C.; Provasi, D.; Raiteri, P.; Donadio, D.; Marinelli, F.; Pietrucci, F.; Broglia, R. A.; Parrinello, M. PLUMED: A portable plugin for free-energy calculations with molecular dynamics. *Computer Physics Communications* **2009**, *180*, 1961–1972.

Curriculum Vitae **Kroes, Jaap** **October 3, 2014**

CONTACT INFORMATION

Jaap Kroes
Avenue de Morges 44
1004 Lausanne, Switzerland

e-mail: jaap.kroes@epfl.ch
Tel: (+41) 787 11 40 44
Born: 2 Dec 1984, Arnhem, Netherlands

EDUCATION

Ecole Polytechnique Féderale de Lausanne, Switzerland **expected 2014**

Ph.D., EPFL – Computational Chemical Physics on the Nanoscale (C3PN)

- Thesis: "Carbon Nanotubes: Adsorption, Point Defects and Structural Deformation from Quantum and Classical Simulations"
- Supervision: Professor W. Andreoni

Radboud University, Nijmegen, Netherlands **June 2010**

M.Sc. (*cum laude*), Physics and Astronomy

- Thesis: "Graphene Nanoribbons and Edge Reconstructions"
- Supervision: Professor A. Fasolino

B.Sc., *Physics and Astronomy*, **June 2008**

RELEVANT WORK EXPERIENCE

Teaching Assistance:

- General Physics I (EPFL) **autumn 2013**
- Numerical Physics (EPFL) **autumn 2011 – spring 2013**
- Mathematical Methods in Physics (EPFL) **autumn 2011**
- Analytical Mechanics (EPFL) **spring 2011**
- Physics Labs for Biologists (EPFL) **autumn 2010**
- Biophysics (RU) **autumn 2009**
- Probability Theory (RU) **autumn 2006**

SCIENTIFIC PUBLICATIONS AND CONFERENCE CONTRIBUTIONS

List of Publications

- J.M.H. Kroes, F. Pietrucci, W. Andreoni, K. Chikkadi, C. Roman, C. Hierold, *NOx Interactions with SWNT Sidewalls: New Insights from Theory and Experiment* (manuscript in preparation)
- J.M.H. Kroes, F. Pietrucci, W. Andreoni, *Single and Double Vacancies on SWNT sidewalls: Comparison of DFT and Classical Forcefield Predictions* (manuscript in preparation)
- J.M.H. Kroes, F. Pietrucci, A. Curioni, and W. Andreoni, Characterizing and Understanding Divalent Adsorbates on Carbon Nanotubes with Ab-Initio and Classical Approaches: Size, Chirality and Coverage Effects, J. Chem. Theory Comput. (10.1021/ct500701n) **2014**
- J.M.H. Kroes, F. Pietrucci, A. Curioni, R. Jaafar, O. Gröning, and W. Andreoni, Atomic Oxygen Chemisorption on Carbon Nanotubes Revisited with Theory and Experiment, J. Phys. Chem. C 117, 1948 **2013**
- W. Andreoni, A. Curioni, J. M. H. Kroes, F. Pietrucci and O. Gröning, Exohedral Hydrogen Chemisorption on a Carbon Nanotube: The Clustering Effect, J. Phys. Chem. C 116, 269 **2012**
- J.M.H. Kroes, M.A. Akhukhov, J.H. Los, N. Pineau, A. Fasolino, Mechanism and free-energy barrier of the type-57 reconstruction of the zigzag edge of graphene, Phys. Rev. B 83, 165411 **2011**

List of Presentations

- "Materials Research Society Spring Meeting 2014", San Fransisco, United States; Apr 21–25 **2014 (talk)**
- "Nano-Tera.ch Annual Meeting 2013" in Bern, Switzerland; May 30–31 **2013 (poster)**
- "Energy from the Sun: Computational Chemists and Physicists Take up the Challenge" conference, Italy; Sept 10–14 **2012 (poster)**
- "Nano-Tera.ch Annual Meeting 2012" Meeting in Zurich, Switzerland; Apr 26–27 **2012 (poster)**
- "Chemical and Topological Functionalization of Graphitic Surfaces: Open Challenges for Computational Modeling", workshop; Lausanne, Switzerland; April 23–25 **2012 (poster)**
- "Towards Reality in Nanoscale Materials V", workshop in Levi, Finland; Feb 20–22 **2012 (poster)**
- "Trends in Nanotechnology 2011", conference; Tenerife (Spain), Nov 21–25 **2011 (poster)**
- "DFT and Beyond: Hands-on Tutorial Workshop 2011 on Ab Initio Molecular Simulations: Toward a First-Principles Understanding of Materials Properties and Functions", workshop; Berlin, Germany; July 12–21 **2011 (poster)**
- "Towards Reality in Nanoscale Materials '10", workshop; Levi, Finland **2010 (poster)**